CHARACTERIZATION OF OPTICAL FIBRE FILTERS

by

© DENNIS KWOK WAH LAM, B.Eng.

A Thesis
Submitted to the School of Graduate Studies
in Partial Fulfillment of the Requirements
for the Degree
Master of Engineering

McMaster University

June 1980

CHARACTERIZATION OF OPTICAL FIBRE FILTERS

TO

My Parents

for their

Immeasurable Love

MASTER OF ENGINEERING (1980)
Electrical Engineering

McMASTER UNIVERSITY
Hamilton, Ontario

TITLE: Characterization of Optical Fibre Filters

AUTHOR: Dennis Kwok Wah Lam, B.Eng. (McMaster University)

SUPERVISOR: Professor B.K. Garside

NUMBER OF PAGES: xiv, 122

ABSTRACT

The major purpose of the work described in this thesis is to characterize the basic properties and evaluate the potential of optical fibre filters. As it turns out, these filters have a spectral bandwidth in reflection which can be varied over a very wide range, from as narrow as 0.01 to several angstroms (Å). As a result, they are potentially very important for applications as multiplexers and demultiplexers in Wavelength-Division-Multiplexing (WDM) in Optical Communication Systems (OCS) (WDM is a means of increasing the data handling capability of a given fibre system through the use of multiple propagating wavelengths). Up to the present moment, gratings in the form of slabs have invariably been employed as the multiplexers and demultiplexers in WDM which greatly restricts the number of wavelengths which can be used since a large spectral bandwidth separation (>100 Å) is required between adjacent channels in such systems.

The optical fibre filters we report here can have a spectral bandwidth narrower than 1 Å and consequently, employing them as multiplexers and demultiplexers in WDM allows a lot more channels to be transmitted. Other than this particular application, optical fibre filters can equally well function as resonant reflectors in a laser cavity, distributed feedback devices, tunable filters or external wavelength selective reflectors for heterojunction injection laser by end butting them to the latter. Furthermore, they have the potential to

be used for equalizing material dispersion in OCS employing single mode fibres. Lastly, they can be tailored to give multifilters, comb filters or in general, filters that perform a variety of specified functions.

The approach to the characterization of optical fibre filters is divided into two parts. The first part deals with the development of a theoretical model that can be used to predict and describe the performance of the optical fibre filters. The second part describes the experiments for the actual fabrication of the filters and subsequent extraction of some of their physical parameters. By comparing the theory with the experimental results, we are able to deduce the range of filters available when using an Argon laser as the means of writing filters and subsequently evaluate their full potential in OCS. Also, a very important relationship between the optical writing power applied to a fibre and the resultant index perturbation in the fibre or equivalently, the resultant filter characteristics, is established so that the actual fabrication of filters designed to satisfy specific functions can be performed.

ACKNOWLEDGEMENTS

I wish to express my deep appreciation to my supervisor, Dr. B.K. Garside, for his guidance and support in this work.

I would like to thank Dr. K.O. Hill and Dr. B.S. Kawasaki of the Communications Research Centre for use of their laboratory facilities, Dr. T.K. Lim for his suggestions on the theoretical analysis described in Chapter 2, and my colleague Mr. T. Znotins for proof reading this thesis.

Finally, to Miss Janet Delsey go my sincere thanks for her excellent typing of the manuscript.

TABLE OF CONTENTS

TABLE OF CONTENTS (cont'd) Page

FIGURE CAPTIONS

FIGURE CAPTIONS (cont'd) Page

FIGURE CAPTIONS (cont'd)

FIGURE CAPTIONS (con'd)

FIGURE CAPTIONS (cont'd)

LIST OF TABLES

LIST OF TABLES (cont'd)

CHAPTER 1

INTRODUCTION

During the past several years, Optical Communication [1-5] has evolved from a speculative research activity plagued with many practical problems to the point where systems implementation is under way for low and moderate data rate systems. The question of Optical Communication replacing the present conventional copper cable system in high data rate telecommunication applications is only when it will occur, not whether it will occur. As a matter of fact, many high bit rate experimental systems have been implemented and proved to be successful [6-8].

The reason Optical Communication Systems (OCS) are becoming such an important field is basically due to its superior performance over the conventional copper cable system at competitive cost. Table 1.1 provides a comparison between the two systems and shows that system cost and lifetime for high data rate system are the only two drawbacks for OCS. However, recent studies [9-10] have indicated that there will be a sharp decrease in cost and improved lifetime in the very near future.

Of all the OCS advantages shown in Table 1.1, the length-bandwidth product (LBWP) deserves special attention. The LBWP shown there is for an OCS employing multimode fibres where material and modal dispersion [11-14] rather than absorption or radiation losses limit the LBWP. By employing single mode fibres, modal dispersion is

TABLE 1.1

Comparison between Optical Communication System and Copper Cable System

Characteristics	Optimal Communication System	Copper Cable System
Length-bandwidth (MHz-Km)	low data rate: 400 moderate data rate: 600 high data rate: ≥1000	20
Spacing between repeaters (Km)	10 - 20	1-2
System cost	low data rate: low moderate data rate: compatible high data rate: presently high, steep decrease in the future	Low now, slow increase in the future
System lifetime (years)	low data rate: 10-40 moderate data rate: 10-40 high data rate: 1-2	20-40
Cross talk	Negligible	low
Noise immunity	High	Medium
Electrical input-output isolation	Complete	No
Short circuit loading	No	Yes
Weight, size	Low	High

eliminated and much higher LBWP of a few GHz-Km, especially in the spectral region of 1.1 - 1.3 μ, is achievable [7,15]. For the ultimate LBWP in OCS, new approaches to radiation propagation in optical fibres are needed. Furthermore, if OCS are implemented, it is inevitable that the traffic on some links will eventually exceed the available capacity. In such cases, it is obviously desirable to be able to increase the capacity of the system without having to replace the fibre cable. One particular method of attacking this problem is to multiplex several signals of different wavelengths into the same fibre.

In OCS, there are basically three major types of multiplexing technique which are: Time Division Multiplexing (TDM), Space Division Multiplexing (SDM) and Frequency or Wavelength Division Multiplexing (FDM or WDM). At the present moment, TDM and WDM are the more popular choices. Although WDM in principle offers the best approach to expanding the data rate capacity as needed, the schemes for approaching the multiplexers and demultiplexers have employed plane or concave gratings which although they offer good coupling efficiencies, require a wide spectral bandwidth to work with. Experimental studies [16-20] have shown that typical wavelength separation between adjacent channels needs to be in the order of 100 Å or more. For a 10 channels system, it is therefore necessary to have a spectral bandwidth of 0.1 μ and very likely then, different sources. Furthermore, there will be differential attenuation for the different channels because the absorption spectra of typical optical fibres are not constant with respect to wavelength over such a large bandwidth region. Suitable dichroic and interference

filters for WDM systems are unavailable and moreover, they are difficult to implement. WDM systems are thus limited to cases where the number of channels to be multiplexed is small, or else require a new approach of implementation.

A novel device having the promise of providing much enhanced WDM capacity based on an initial discovery by Hill and Kawasaki [21] is reported here. This device is simply called an optical fibre filter and works on the principle of photosensitivity in GeO_2. It is found that when a 4% GeO_2 doped SiO_2 near single mode fibre is irradiated by highly intense contradirectional coherent beams from an Argon laser, a periodic modulation of the refractive index in the core region along the fibre is formed. This index modulated fibre then behaves as a length limited, Bragg distributed-feedback waveguide filter similar to the grating filters in the thin film waveguides [22-24]. The main importance of this optical fibre filter is its extremely narrow spectral bandwidth. As reported by Hill and Kawasaki, a frequency bandwidth of 200 MHz was measured. Aside from this special feature, it was found that the filter is long lived (no significant degradation was observed in its reflectance over a period of two weeks) and tunable by varying either the temperature or stress applied to it. Other important features include the capability of being overwritten without erasure of previously written grating so as to give multifilters or comb filters. Furthermore, it will be shown that there is an anomalous dispersion region in the phase characteristics of the filter which may prove to be valuable in equalizing material dispersion in OCS which uses single mode

fibres. Finally, it can be used as a resonant reflector in a laser cavity as was demonstrated by Hill and Kawasaki [21].

In order to develop an understanding of optical fibre filters, it is necessary to characterize the capability in terms of the range of index perturbation that can be induced as a function of writing power. Furthermore, their physical characteristics such as spectral bandwidth, size or rather, length, phase response and reflectance as a function of the induced index perturbation must be delineated so that filters can be designed to perform specific functions.

The work reported in this thesis is aimed at investigating the basic characteristics as outlined above of the GeO_2 doped SiO_2 single mode fibre filters. A theoretical model is first formulated and predictions are made of the spectral bandwidth ($\Delta\lambda_t$), phase characteristics ($\Delta\beta_p$) and effective cutoff length (L_{cutoff}) (which is defined as the length of the filter when the normalized reflectance is equal to 0.9) of the filter as a function of the index perturbation size. Experiments are then reported which are designed to obtain $\Delta\lambda_t$ and L_{cutoff} for filters of different writing power and comparison is made between the measurements and the theory to deduce the induced index perturbation. Furthermore, by comparing the writing power used in the experiment and the corresponding induced index perturbation deduced from the theory, a relationship is established between the writing power and the induced index perturbation over the available range of writing powers. Having established the basic filter characteristics, predictions concerning the potential usages of optical fibre filters are

discussed.

The layout of this thesis is as follows. In Chapter 2, the theoretical model for the optical fibre filters is presented and numerous predictions of the filters' physical characteristics mentioned above are illustrated as a function of the induced index perturbation. Chapter 3 describes the experiments that were used to deduce the spectral bandwidth ($\Delta\lambda_t$) and effective cutoff length (L_{cutoff}) of the filters. Results and a preliminary dicussion are presented but the detailed analysis of the results is deferred to Chapter 4. Included in Chapter 4 are the comparisons between the two sets of experimental data on $\Delta\lambda_t$ and L_{cutoff} and deduction of the filters' characteristics upon comparing the experimental data with the theory. Also, a discussion on the practical and potential applications of the optical fibre filters is presented. The final chapter summarizes both the theory and experiments reported in this thesis and presents suggestions for further research aimed at developing a better understanding of the optical fibre filters. It is hoped that this thesis will serve the purpose of introducing optical fibre filters as novel and important devices in Optical Communication System and stimulate further research in their development.

CHAPTER 2

A THEORETICAL MODEL

2.1 INTRODUCTION

In this chapter, a theoretical model is reported for the propagation of electromagnetic waves in an optical fibre with a periodically varying refractive index. A number of authors [22-32] have discussed models for the propagation of radiation in the related, but simpler, cases of thin film gratings, couplers and filters. In general, the so-called Coupled Mode Theory [33-36] has been employed to analyze these structures. In this approach, the radiation field is expanded in a suitable basis set of unperturbed modes, and the periodically varying refractive index is treated as a perturbation which produces coupling between the modes. This method is adequate provided the perturbation is small and only the first order Bragg condition is effective. Over the range of experimental conditions utilized in the experiments reported here, the conditions for using the Coupled Mode Theory are well satisfied. However, if filters of much higher perturbation can be written, then Coupled Mode Theory will be suspected, and a more rigorous analysis, such as is afforded by Floquet Theory [37-39], will have to be employed.

A fibre waveguide differs from a thin film waveguide in its geometry; requiring a three dimensional instead of two dimensional

analysis. Consequently, the analytical form of the eigenmodes is more complex, but otherwise the treatment of the two cases is basically the same. As indicated above, we will use Coupled Mode Theory in our analysis. The relationship between this approach and the more exact analysis obtained from Floquet Theory has been discussed in some detail by Jaggard and Evans [38-40].

In section 2 of this Chapter, the Coupled Mode Theory formalism is presented. Several theoretical predictions based on this analysis are presented in section 3, The chapter ends with some discussion concerning the assumptions and approximations made in the theoretical analysis.

2.2 COUPLED MODE THEORY FORMALISM

2.2.1 Introduction

In the analysis of an optical fibre filter which has its refractive index periodically modulated along its length, it is appropriate to express the perturbed field in terms of the ideal fields. The ideal fields are the fields for a fibre which has a uniform refractive index along its length. In what is to follow, the ideal fields are obtained first and then used as a basis set for the perturbed fields.

2.2.2 Ideal Fields

Figure 2.1 shows the cross section of an optical fibre together with the co-ordinate axes which will be used in the analysis. The fact that the difference between n_{CORE} and n_{CLAD} is very small ($n_{CORE} - n_{CLAD} << 1$) in the fibres used here allows the usage of Linearly Polarized

FIGURE 2.1

Cross section of an optical fibre. The refractive index in the core and cladding regions is n_1 and n_2 respectively, and the core diameter is 2a.

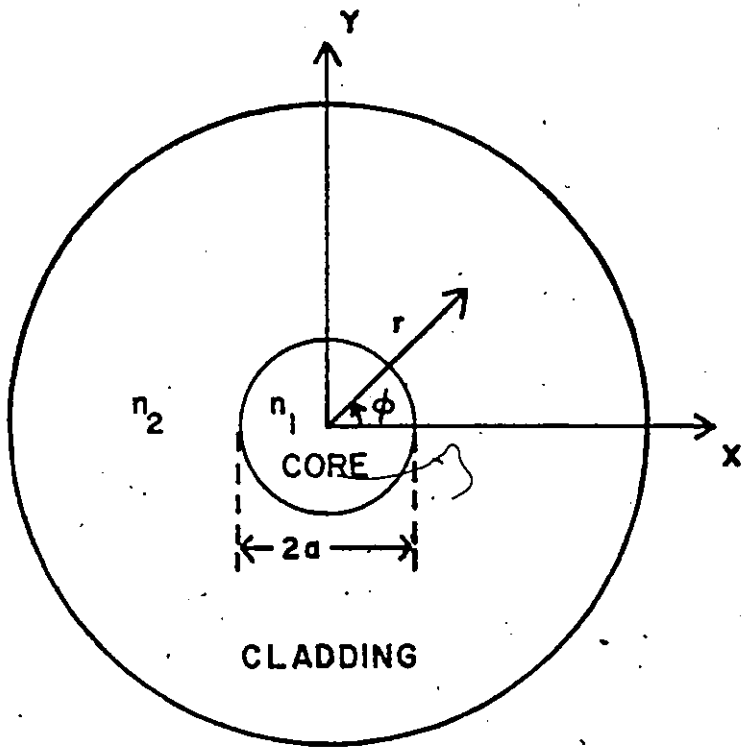
Y
r
n_2
n_1
ϕ
X
CORE
2a
CLADDING

Fields [41-43] instead of the exact Vector Fields in the analysis. Two further approximations are made and they are (1) no absorption loss, and (2) the propagating modes do not couple significantly to the TE or TM radiation modes. The justification to these two assumptions is that the fibre has a quoted total loss of 5 dB/Km and the lengths of the fibres used in all the experiments never exceed 1 metre. There is also a few other assumptions which will be indicated during the development of the analysis.

To start the analysis for an ideal fibre, the Wave Equation is invoked;

$$\nabla^2\psi + n_i^2 k^2 \psi = 0 \tag{2.1}$$

where

n_i : n_1, n_2 = n_{CORE}, n_{CLAD}, respectively,

ψ = scalar longitudinal fields, and

k = $2\pi/\lambda$ = free space propagation constant.

For the present purposes, it is appropriate to write Eq. (2.1) in cylindrical co-ordinates:

$$\frac{\partial^2\psi}{\partial r^2} + \frac{1}{r}\frac{\partial\psi}{\partial r} + \frac{1}{r^2}\frac{\partial^2\psi}{\partial\phi^2} + \frac{\partial^2\psi}{\partial z^2} + n_i^2 k^2 \psi = 0 \tag{2.2}$$

Since the z dependence of ψ is in the form of $e^{\pm i(\omega t-\beta z)}$, where ω and β are the angular frequency and the propagation constant respectively, Eq. (2.2) can be written as

$$\frac{\partial^2\psi}{\partial r^2} + \frac{1}{r}\frac{\partial\psi}{\partial r} + \frac{1}{r^2}\frac{\partial^2\psi}{\partial\phi^2} + (n_i^2 k^2 - \beta^2)\psi = 0 \tag{2.3}$$

It is now assumed that ψ can be written in the form:

$$\psi(r,\phi,z,t) = F(r)\cos(\nu\phi)\, e^{i(\omega t-\beta z)} \tag{2.4}$$

Substituting it into Eq. (2.3) gives

$$\cos(\nu\phi)\left(\frac{\partial^2 F}{\partial r^2} + \frac{1}{r}\frac{\partial F}{\partial r}\right) - \frac{\nu^2}{r^2}\cos(\nu\phi) + \kappa^2 F\cos(\nu\phi) = 0 \tag{2.5}$$

where

$$\kappa^2 = n_{CORE}^2 k^2 - \beta^2 > 0 \tag{2.6}$$

for the core region ($r < a$) and

$$\cos(\nu\phi)\left(\frac{\partial^2 F}{\partial r^2} + \frac{1}{r}\frac{\partial F}{\partial r}\right) - \frac{\nu^2}{r^2}\cos(\nu\phi) - \gamma^2 F\cos(\nu\phi) = 0 \tag{2.7}$$

where

$$\gamma^2 = \beta^2 - n_{CLAD}^2 k^2 > 0 \tag{2.8}$$

for the cladding region ($r > a$).

For the core region, Eq. (2.5) is the Bessel's differential equation and the two possible solutions for integral ν are Bessel function of the first kind $J_\nu(\kappa r)$ and of the second kind $N_\nu(\kappa r)$. Employing the boundary condition that the field at the centre of the core ($r = 0$) must be finite implies that $J_\nu(\kappa r)$ is the only allowable solution.

It has been shown by Marcuse [44] that the field amplitude of the longitudinal fields can be adjusted so that only one set of the two possible transverse fields exist. The required longitudinal fields then are:

$$\psi_z^{*}: E_z = \frac{iA\kappa}{2\beta_\nu}\left[J_{\nu+1}(\kappa r)\begin{Bmatrix}\sin(\nu+1)\phi\\ -\cos(\nu+1)\phi\end{Bmatrix} - J_{\nu-1}(\kappa r)\begin{Bmatrix}\sin(\nu-1)\phi\\ -\cos(\nu-1)\phi\end{Bmatrix}\right] \quad (2.9)$$

$$H_z = \frac{-iA\kappa}{2k}\left(\frac{\varepsilon_o}{\mu_o}\right)^{1/2}\left[J_{\nu+1}(\kappa r)\begin{Bmatrix}\cos(\nu+1)\phi\\ \sin(\nu+1)\phi\end{Bmatrix} - J_{\nu-1}(\kappa r)\begin{Bmatrix}\cos(\nu-1)\phi\\ \sin(\nu-1)\phi\end{Bmatrix}\right] \quad (2.10)$$

where

β_ν = propagation constant for mode ν,

A = arbitrary amplitude coefficient to be determined,

ε_o = free space susceptibility, and

μ_o = free space permeability.

To obtain the transverse field, the following Maxwell equations are invoked,

$$\bar{\nabla} \times \bar{H} = \varepsilon_o n^2 \frac{\partial \bar{E}}{\partial t} \quad (2.11)$$

$$\bar{\nabla} \times \bar{E} = -\mu_o \frac{\partial \bar{H}}{\partial t} \quad (2.12)$$

where the upper bar "$^-$" implies vector quantity and the results are

$$E_y = A\, J_\nu(\kappa r)\begin{Bmatrix}\cos(\nu\phi)\\ \sin(\nu\phi)\end{Bmatrix} \quad (2.13)$$

---

*The phase factor $e^{i(\omega t-\beta z)}$ will be deleted from now on for simplicity sake.

$$H_x = -nA \frac{\beta_\nu}{|\beta_\nu|} \left(\frac{\varepsilon_o}{\mu_o}\right)^{1/2} J_\nu(\kappa r) \begin{Bmatrix} \cos(\nu\phi) \\ \sin(\nu\phi) \end{Bmatrix} \tag{2.14}$$

$$E_x = 0 \tag{2.15}$$

$$H_y \simeq 0 \tag{2.16}$$

For the cladding region, going through the same procedure as above gives

$$\psi_z : E_z = \frac{-A\gamma}{2\beta_\nu} \frac{J_\nu(\kappa a)}{H_\nu^{(1)}(i\gamma a)} \left[H_{\nu+1}^{(1)}(i\gamma r) \begin{Bmatrix} \sin(\nu+1)\phi \\ -\cos(\nu+1)\phi \end{Bmatrix} + H_{\nu-1}^{(1)}(i\gamma r) \begin{Bmatrix} \sin(\nu-1)\phi \\ -\cos(\nu-1)\phi \end{Bmatrix}\right] \tag{2.17}$$

$$H_z = \frac{A\gamma}{2k}\left(\frac{\varepsilon_o}{\mu_o}\right)^{1/2} \frac{J_\nu(\kappa a)}{H_\nu^{(1)}(i\gamma a)} \left[H_{\nu+1}^{(1)}(i\gamma r) \begin{Bmatrix} \cos(\nu+1)\phi \\ \sin(\nu+1)\phi \end{Bmatrix} - H_{\nu-1}^{(1)}(i\gamma r) \begin{Bmatrix} \cos(\nu-1)\phi \\ \sin(\nu-1)\phi \end{Bmatrix}\right] \tag{2.18}$$

$$E_y = \frac{AJ_\nu(\kappa a)}{H_\nu^{(1)}(i\gamma a)} H_\nu^{(1)}(i\gamma r) \begin{Bmatrix} \cos(\nu\phi) \\ \sin(\nu\phi) \end{Bmatrix} \tag{2.19}$$

$$H_x = -nA \frac{\beta_\nu}{|\beta_\nu|} \left(\frac{\varepsilon_o}{\mu_o}\right)^{1/2} \frac{J_\nu(\kappa a)}{H_\nu^{(1)}(i\gamma a)} H_\nu^{(1)}(i\gamma r) \begin{Bmatrix} \cos(\nu\phi) \\ \sin(\nu\phi) \end{Bmatrix} \tag{2.20}$$

$$E_x = 0 \tag{2.21}$$

$$H_y \simeq 0 \tag{2.22}$$

where

$H_\nu^{(1)}$ = Hankel function of the first kind.

It is important to point out here that by introducing a slightly different form of E_z and H_z, it is possible to make E_x and H_y be the nonvanishing transverse fields instead of their orthogonal counterpart E_y and H_x. Appendix A gives the required form of H_z and E_z and the corresponding transverse field expressions.

In order to satisfy the boundary conditions, all the tangential fields must be continuous at the boundary between the core and the cladding. Transforming the transverse fields into the cylindrical form gives

$$E_r = E_x \cos\phi + E_y \sin\phi \tag{2.23}$$

$$E_\phi = -E_x \sin\phi + E_y \cos\phi \tag{2.24}$$

and similarly for H_r and H_ϕ. The fact that either E_x or E_y is zero implies that E_ϕ is proportional to either E_x or E_y. Since E_x and E_y are continuous by themselves, E_ϕ is therefore continuous as well. For H_ϕ, the fields inside and outside the core are multiplied by n_{CORE} and n_{CLAD} respectively. The fact that the difference between n_{CORE} and n_{CLAD} is much less then 1.0 make H_ϕ continuous, to a very good approximation, as well. What is left now is that E_z and H_z must be continuous and using either Eqs. (2.9, 2.17) or Eqs. (2.10, 2.18) gives

$$\frac{\kappa\, J_{\nu+1}(\kappa a)}{J_\nu(\kappa a)} = \frac{i\gamma H^{(1)}_{\nu+1}(i\gamma a)}{H^{(1)}_\nu(i\gamma a)} \tag{2.25}$$

$$\frac{\kappa\, J_{\nu-1}(\kappa a)}{J_\nu(\kappa a)} = \frac{i\gamma H^{(1)}_{\nu-1}(i\gamma a)}{H^{(1)}_\nu(i\gamma a)} \tag{2.26}$$

Equations (2.25) and (2.26) are equivalent by the relationship

$$Z_{\nu+1}(x) = \left(\frac{2\nu}{x}\right) Z_\nu(x) - Z_{\nu-1}(x) \tag{2.27}$$

where

$$Z_\nu(x) = H_\nu^{(1)}(x) \text{ or } J_\nu(x) \tag{2.28}$$

Using Eq. (2.25) or (2.26) then, the eigen propagation constant β_ν can be found. It is worthwhile to mention here that β_ν should actually have two subscripts ($\beta_{\nu\mu}$) instead of only ν which is derived from the azimuthal symmetry. The subscript μ corresponds to the multiple roots found from Eq. (2.25) or (2.26) for each ν.

Before proceeding to the analysis of the perturbed fields, we must determine the amplitude coefficient A, which was introduced in Eq. (2.9), for each particular mode ν. Using the relationship for the power, P_ν, carried by mode ν:

$$P_\nu = \frac{1}{2} \int_0^{2\pi} \int_0^{\infty} (E_x H_y^* - E_y H_x^*)\Big|_\nu \, r \, dr d\phi \tag{2.29}$$

where * denotes complex conjugate, the fields expressions for E_x, E_y, H_x and H_y are substituted into it and evaluating the integral gives

$$A = \left[\frac{4(\mu_o/\varepsilon_o)^{1/2} \gamma^2 P}{e_\nu \pi a^2 n(n_{CORE}^2 - n_{CLAD}^2) k^2 |J_{\nu-1}(\kappa a) J_{\nu+1}(\kappa a)|}\right]^{1/2} \tag{2.30}$$

where

$e_\nu = 2$ for $\nu = 0$

$= 1$ for $\nu \neq 0$

and

$$n = \frac{(n_{CORE} + n_{CLAD})}{2}$$

2.2.3 Perturbed Fields

In order to simplify the algebra involved in the following analysis, both the electric and magnetic fields are separated into longitudinal and transverse components.

$$E = E_t + E_z \tag{2.31a}$$

$$H = H_t + H_z \tag{2.31b}$$

Writing the operator ∇ in similar format

$$\nabla = \nabla_t + e_z \cdot \partial/\partial z \tag{2.31c}$$

where e_z is a unit vector in the z direction, the curls of E and H can be expressed as

$$(\nabla \times E)_t = \nabla_t \times E_z + e_z \times \partial E_t/\partial z \tag{2.32a}$$

$$(\nabla \times E)_z = \nabla_t \times E_t \tag{2.32b}$$

$$(\nabla \times H)_t = \nabla_t \times H_z + e_z \times \partial H_t/\partial z \tag{2.32c}$$

$$(\nabla \times H)_z = \nabla_t \times H_t \tag{2.32d}$$

Writing Maxwell equations

$$(\bar{\nabla} \times \bar{H}) = i\,\omega\,\varepsilon_o\,n^2\,\bar{E} \tag{2.33a}$$

$$(\bar{\nabla} \times \bar{E}) = -i\,\omega\,\mu_o\,\bar{H} \tag{2.33b}$$

in the separate transverse and longitudinal forms gives

$$\nabla_t \times H_t = i\,\omega\,\varepsilon_o\, n^2\, E_z \tag{2.34a}$$

$$(\nabla \times H)_t = i\,\omega\,\varepsilon_o\, n^2\, E_t \tag{2.34b}$$

$$\nabla_t \times E_t = -i\,\omega\,\mu_o\, H_z \tag{2.34c}$$

$$(\nabla \times E)_t = -i\,\omega\,\mu_o\, H_t \tag{2.34d}$$

Equations (2.34a) and (2.34c) show that E_z and H_z are simply the derivatives of H_t and E_t. Hence, only the transverse fields have to be solved for and this is the reason for separating the fields into the longitudinal and transverse components.

Substituting Eqs. (2.34a) to (2.34d) into Eqs. (2.32a) and (2.32c) gives the equation for analyzing a filter with any arbitrary refractive index profile (n(x,y,z)).

$$-\frac{1}{i\omega\mu_o}\nabla_t \times (\nabla_t \times E_t) + e_z \times \frac{\partial H_t}{\partial z} = i\,\omega\,\varepsilon_o\, n^2\, E_t \tag{2.35}$$

$$\frac{1}{i\omega\varepsilon_o}\nabla_t \times \left(\frac{1}{n^2}\nabla_t \times H_t\right) + e_z \times \frac{\partial E_t}{\partial z} = -i\,\omega\,\mu_o\, H_t \tag{2.36}$$

The only assumption that is made in obtaining these two equations is that the medium is nonmagnetic. By letting the refractive index profile be independent of z(n_o(x,y)), they become

$$-\frac{1}{i\omega\mu_o}\nabla_t \times (\nabla_t \times \mathcal{E}_{\nu t}) - i\beta_\nu (e_z \times \mathcal{H}_{\nu t}) = i\omega\,\varepsilon\, n_o^2\, \mathcal{E}_{\nu t} \tag{2.37}$$

$$\frac{1}{i\omega\varepsilon_o}\nabla_t \times \left(\frac{1}{n_o^2}\nabla_t \times \mathcal{H}_{\nu t}\right) - i\beta_\nu (e_z \times \mathcal{E}_{\nu t}) = -i\omega\,\mu_o\, \mathcal{H}_{\nu t} \tag{2.38}$$

where $\mathcal{E}_{\nu t}$ and $\mathcal{H}_{\nu t}$ are the ideal eigenmode fields that were discussed in Section 2.2.2 and $n_o(x,y)$ is the refractive index profile for a uniform fibre.

An exact ideal field expansion for the perturbed field will involve a summation of all the guided and radiation modes. But recalling that the filter is short and does not allow much loss, only the guided modes will be required. Letting E_t and H_t be the perturbed fields, their expansions are therefore

$$E_t = \sum_{\nu=1}^{N} a_\nu \mathcal{E}_{\nu t} \tag{2.39}$$

$$H_t = \sum_{\nu=1}^{N} b_\nu \mathcal{H}_{\nu t} \tag{2.40}$$

where N is the number of guided modes and a_ν, b_ν are the mode amplitude coefficients. These amplitude coefficients can be found by substituting Eq. (2.39) and (2.40) into Eqs. (2.35) and (2.36) and using Eqs. (2.37) and (2.38) to simplify the final expression. Assuming that the refractive index profile is continuous, summation and differentiation can therefore be interchanged and the results are

$$\sum_{\nu=1}^{N} \{ (\frac{db_\nu}{dz} + i\beta_\nu a_\nu)(e_z x \mathcal{H}_{\nu t}) - i\omega\epsilon_o(n^2-n_o^2)a_\nu \mathcal{E}_{\nu t}\} = 0 \tag{2.41}$$

$$\sum_{\nu=1}^{N} \{ (\frac{da_\nu}{dz} + i\beta_\nu b_\nu)(e_z x \mathcal{E}_{\nu t}) + \frac{1}{i\omega\epsilon_o} b_\nu \nabla_t x [(\frac{1}{n^2} - \frac{1}{n_o^2})(\nabla_t x \mathcal{H}_{\nu t})]\} = 0 \tag{2.42}$$

Making use of the orthogonal property for the ideal modes;

$$\frac{1}{2} \int_{-\infty}^{\infty} \int_{-\infty}^{\infty} e_z \cdot (\mathcal{E}_{\nu t} \times \mathcal{H}^*_{\mu t})\, dxdy = \delta_{\nu\mu} \cdot P \tag{2.43}$$

where $\delta_{\nu\mu}$ = Kronecker Delta and

P = power.

Equations (2.41) and (2.42) can be written as

$$\left(\frac{db_\mu}{dz} + i\beta_\mu a_\mu\right) = 2 \sum_{\nu=1}^{N} a_\nu \bar{K}_{\mu\nu} \tag{2.44}$$

$$\left(\frac{da_\mu}{dz} + i\beta_\mu b_\mu\right) = 2 \sum_{\nu=1}^{N} b_\nu \bar{k}_{\mu\nu} \tag{2.45}$$

where

$$\bar{K}_{\mu\nu} = \frac{\Psi}{i} \int_{-\infty}^{\infty} \int_{-\infty}^{\infty} \mathcal{E}_{\nu t} \cdot \mathcal{E}^*_{\mu t} (n^2 - n_o^2)\, dxdy \tag{2.46}$$

$$\bar{k}_{\mu\nu} = \frac{\Psi}{i} \int_{-\infty}^{\infty} \int_{-\infty}^{\infty} (n^2 - n_o^2) \left(\frac{n_o}{n}\right)^2 \mathcal{E}_{\mu z}^* \mathcal{E}_{\nu z}\, dxdy \tag{2.47}$$

and

$$\Psi = \frac{\omega \varepsilon_o}{4P} \tag{2.48}$$

$\bar{K}_{\mu\nu}$ and $\bar{k}_{\mu\nu}$ are essentially the transverse and longitudinal coupling coefficients respectively. Making use of the knowledge that $a_\mu = b_\mu$ for forward travelling waves and $a_\mu = -b_\mu$ for backward travelling waves, it can be shown that

$$\frac{da_\mu^+}{dz} = -i\beta_\mu a_\mu^+ + \sum_{\nu=1}^{N} (a_\nu^+ K_{\mu\nu}^{++} + a_\nu^- K_{\mu\nu}^{+-}) \tag{2.49}$$

$$\frac{da_\mu^-}{dz} = i\beta_\mu a_\mu^- + \sum_{\nu=1}^{N} (a_\nu^+ K_{\mu\nu}^{-+} + a_\nu^- K_{\mu\nu}^{--}) \tag{2.50}$$

where

$+ \rightarrow$ forward travelling wave

$- \rightarrow$ backward travelling wave

and

$$K_{\mu\nu}^{pq} = p\,\bar{K}_{\mu\nu} + q\,\bar{k}_{\mu\nu} \tag{2.51}$$

Postulating

$$a_\mu^+ = C_\mu^+ e^{-i\beta_\mu z} \tag{2.52a}$$

$$a_\mu^- = C_\mu^- e^{i\beta_\mu z} \tag{2.52b}$$

and substituting them into Eqs. (2.49) and (2.50) gives

$$\frac{dC_\mu^+}{dz} = \sum_{\nu=1}^{N} [C_\mu^+ e^{i(\beta_\mu-\beta_\nu)z} K_{\mu\nu}^{++} + C_\mu^- e^{i(\beta_\mu+\beta_\nu)z} K_{\mu\nu}^{+-}] \tag{2.53}$$

$$\frac{dC_\mu^-}{dz} = \sum_{\nu=1}^{N} [C_\mu^+ e^{-i(\beta_\mu+\beta_\nu)z} K_{\mu\nu}^{-+} + C_\mu^- e^{-i(\beta_\mu-\beta_\nu)z} K_{\mu\nu}^{--}] \tag{2.54}$$

It has been shown [44] that the longitudinal fields are often very much smaller than the transverse fields and therefore, we make the assumption

$$K_{\mu\nu}^{pq} \simeq p\,\overline{K}_{\mu\nu} \tag{2.55}$$

At this point, the refractive index profile must be specified before the analysis can proceed further. The index profile is taken to be sinusoidal, since this is what is expected for the fibre filters of reasonable writing powers. Accordingly, we take the index profile to be of the form:

$$\begin{aligned} n^2(z) = \varepsilon(z) &= (n_o^2 + \Delta\varepsilon \cos \theta z) \quad r < a \\ &= n_o^2 \qquad\qquad\qquad\quad r > a \end{aligned} \tag{2.56}$$

where

$\theta = \frac{2\pi}{\Lambda}$

Λ = period of the perturbation

$\Delta\varepsilon$ = perturbation parameter

as shown in Fig. 2.2.

Substituting Eqs. (2.55) and (2.56) into Eq. (2.53) yields

$$\frac{dC_\mu^+}{dz} = \sum_{\nu=1}^{N} [C_\mu^+ e^{i(\beta_\mu-\beta_\nu)z} + C_\mu^- e^{i(\beta_\mu-\beta_\nu)z}] \frac{\Psi}{i} \frac{\Delta\varepsilon}{2} (e^{i\theta z} + e^{-i\theta z}) I_{\mu\nu_t} \tag{2.57}$$

where

$$I_{\mu\nu_t} = \int_o^a \int_o^{2\pi} \mathcal{E}_{\mu t} \cdot \mathcal{E}_{\nu t}\, r dr\, d\phi \tag{2.58}$$

Assuming only a single mode* can propagate, $\nu=1$ and there are two modes corresponding to C_1^+ and C_1^-, Eq. (2.57) becomes

---

* The fibre is genuinely single mode for $\lambda > 0.8\mu$. In our experiments where $\lambda \simeq 0.5\mu$, it can actually support 3 modes. We will justify our assumption at a later stage.

FIGURE 2.2

An optical fibre filter having an index profile of $\varepsilon(z) = (n_o^2 + \Delta\varepsilon \cos 2\pi z/\Lambda)$ where n_o^2 is the average value of the refractive index, $\Delta\varepsilon$ is the induced index perturbation and Λ is the period of the index profile.

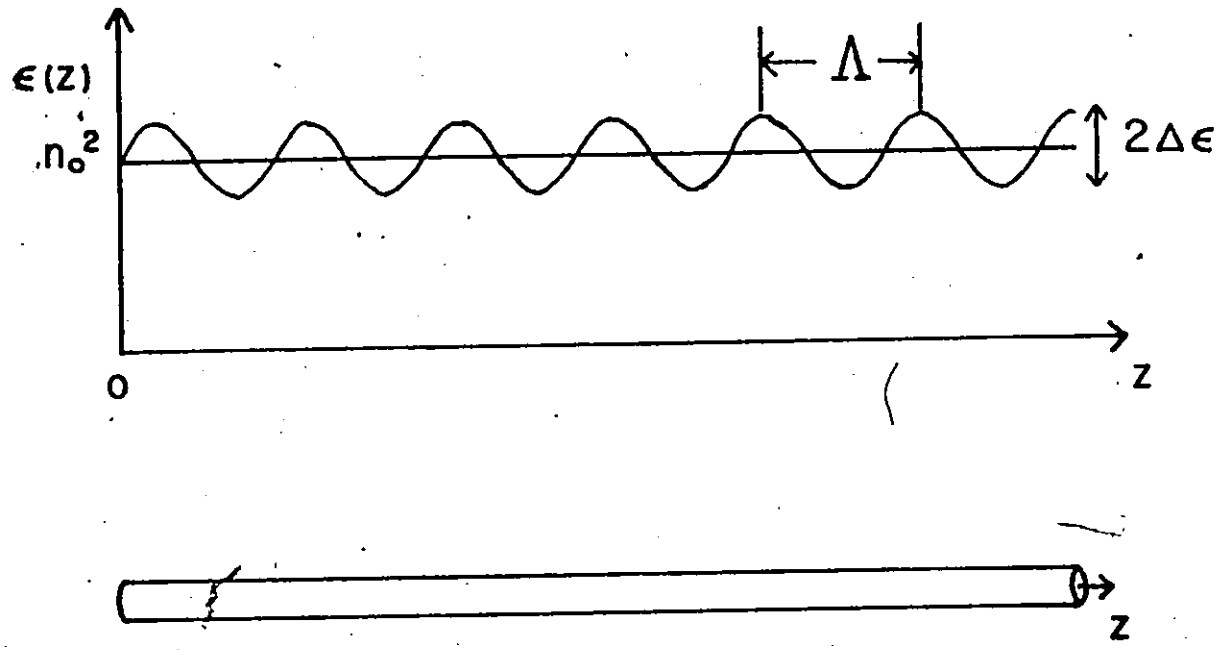

OPTICAL FIBRE FILTER

$$\frac{dC^+}{dz} = \frac{\Omega}{i}\,[2C^+ \cos(\theta z) + C^- (e^{i2\Delta\beta z} + e^{i2\theta z})] \qquad (2.59)$$

where

$$\Omega = \frac{\Delta\epsilon}{2}\,\Psi\, I_{11_t} \qquad (2.60a)$$

$$\Delta\beta = \beta - \frac{\theta}{2} = \beta - \frac{\pi}{\Lambda} \qquad (2.60b)$$

and the subscript 1 has been dropped.

Similar treatment to Eq. (2.54) gives

$$\frac{dC^-}{dz} = \frac{-\Omega}{i}\,[C^+ (e^{-i2\Delta\beta z} + e^{-i2\theta z}) + 2C^- \cos(\theta z)] \qquad (2.61)$$

Ignoring the fast varying terms of $e^{\pm i\theta z}$ and $e^{\pm i2\theta z}$ or equivalently, averaging over these variables, Eqs. (2.59) and (2.61) combine to give two first order coupled differential equations.

$$\frac{dC^+}{dz} = \frac{\Omega}{i}\; C^- \; e^{i2\Delta\beta z} \qquad (2.62a)$$

$$\frac{dC^-}{dz} = \frac{-\Omega}{i}\, C^+ \; e^{-i2\Delta\beta z} \qquad (2.62b)$$

Solving Eq. (2.62) with the boundary conditions of

(1) $C^+(0) = 1.0$

(2) $C^-(L) = 0.0$

where

L = length of the filter

gives

$$C^{+}(z) = \frac{-e^{i\Delta\beta z}}{[\Delta\beta\sinh(SL)-iS\cosh(SL)]}\ [\Delta\beta\sinh(S(z-L))+iS\cosh(S(z-L))] \quad (2.63)$$

$$C^{-}(z) = \frac{\Omega\ e^{-i\Delta\beta z}}{[\Delta\beta\sinh(SL) - iS\cosh(SL)]}\ \sinh(S(z-L)) \quad (2.64)$$

where

$$S = (\Omega^2 - \Delta\beta^2)^{1/2}$$

Using the results shown in this section, we can now proceed to analyze the kind of filters that can be made as a function of the induced index perturbation $\Delta\varepsilon$.

2.3 THEORETICAL PREDICTIONS

There are basically three important quantities that characterize optical fibre filters. They are (1) spectral variations of the filter reflection coefficient ($R(\lambda)$) which includes information on the maximum reflectance and the spectral bandwidth, (2) deviation of the perturbed propagation constant from the eigen or ideal propagation constant ($\Delta\beta_p$), and (3) the effective cutoff length of the filter (L_{cutoff}) which is defined as the length at which $R(L)$ is equal to 0.9.

$R(\lambda)$ will dictate the amplitude response of the filter and $\Delta\beta_p$ and L_{cutoff} will dictate the phase response. Therefore when the filter is used as a device to select different wavelength, only $R(\lambda)$ will have to be known whereas if it is used to perform phase compensation or adjustment, $\Delta\beta_p$ and L_{cutoff} will have to be known instead.

In order to obtain information on these quantities, we can use Eqs. (2.63) and (2.64) and express $R(\lambda)$ as

$$R(\lambda) = \left|\frac{C^-(0)}{C^+(0)}\right|^2 = \frac{\Omega^2 \sinh^2 (SL)}{\Delta\beta^2 \sinh^2(SL) + S^2\cosh^2(SL)} \quad \text{for } \Omega^2 > \Delta\beta^2 \qquad (2.65)$$

$$= \frac{\Omega^2 \sin^2 (QL)}{\Delta\beta^2 - \Omega^2\cos^2 (QL)} \quad \text{for } \Omega^2 < \Delta\beta^2 \qquad (2.66)$$

where

$S = (\Omega^2 - \Delta\beta^2)^{1/2}$ as before, and

$Q = (\Delta\beta^2 - \Omega^2)^{1/2} = iS$

The regions of $\Omega^2 > \Delta\beta^2$ and $\Delta\beta^2 > \Omega^2$ are respectively called the stopband and passband regions. In the stopband region, the coupling coefficient Ω is greater than the detuning of the propagation constant whereas in the passband region, the converse is true. As long as the filter cutoff length is not limited by the filter physical length (L_{phy}), $R(\lambda)$ can always be equal to 1.0 for all λ in the stopband region as L approaches very large value. Rewriting Eq. (2.65) as

$$R(\lambda) = \frac{\Omega^2}{\Delta\beta^2 + S^2\coth^2(SL)}$$

as $L \to \infty$, $\coth (SL) \to 1.0$ and therefore

$$R(\lambda) = \frac{\Omega^2}{\Delta\beta^2 + S^2} = 1.0 \quad \text{for } \Omega^2 > \Delta\beta^2 \qquad (2.67)$$

In the passband region, the sine and cosine terms cause $R(\lambda)$ to become rapidly oscillating at large L and $R(\lambda)$ has a maximum value at $QL = \pi/2$ which correspond to

$$R(\lambda) = \frac{\Omega^2}{\Delta\beta^2} \qquad \text{for} \quad \Omega^2 < \Delta\beta^2 \tag{2.68}$$

Figure 2.3 shows $R(\lambda)$ for L_{phy} much greater than L_{cutoff}.

In the case where L_{cutoff} is limited by L_{phy}, Eqs. (2.67) and (2.68) do not apply and the correct length of L_{phy} has to be used in Eqs. (2.65) and (2.66). Figures 2.4 and 2.5 show $R(\lambda)$ for $L_{phy} < L_{cutoff}$ for $\lambda \neq \lambda_c$ and $R(L)$ respectively for a typical value of induced perturbation ($\Delta\varepsilon$). Comparing Figs. 2.3 and 2.4, (which have the same value of $\Delta\varepsilon$)the spectral bandwidth for $L_{phy} > L_{cutoff}$ case is greater than that of $L_{phy} < L_{cutoff}$ case. In the case shown, the difference is a factor of 1.18. In Appendix B, it is shown that the factor is on the average equal to 1.15.

For different $\Delta\varepsilon$, $R(L)$ and $R(\lambda)$ will be different as expected and Figs. 2.6 - 2.8 show families of curves for a typical range of $\Delta\varepsilon$. From these figures, the behaviour of $\Delta\lambda_t$ and L_{cutoff} as a function of $\Delta\varepsilon$ can be deduced and they are plotted in Figs. 2.9 and 2.10 respectively. Referring to them, it can be seen that as $\Delta\varepsilon$ increases, $\Delta\lambda_t$ increases linearly whereas L_{cutoff} decreases in a nonlinear fashion. As $\Delta\varepsilon$ exceeds 8×10^{-5}, the change in L_{cutoff} between $\Delta\varepsilon$ of increment 0.5×10^{-5} is less than 1 mm. This minute change of L_{cutoff} at large $\Delta\varepsilon$ makes it almost impossible to measure L_{cutoff} accurately in the experiment for

FIGURE 2.3

Theoretical spectral reflectance curve ($R(\lambda)$) for the case of physical length much longer than the effective cutoff length of the filter. The value of the induced index perturbation ($\Delta\varepsilon$) is 1.2×10^{-4} and $\lambda-\lambda_c$ represents the deviation of wavelength (λ) from the Bragg wavelength (λ_c). The full width half maximum is 0.16 Å as shown.

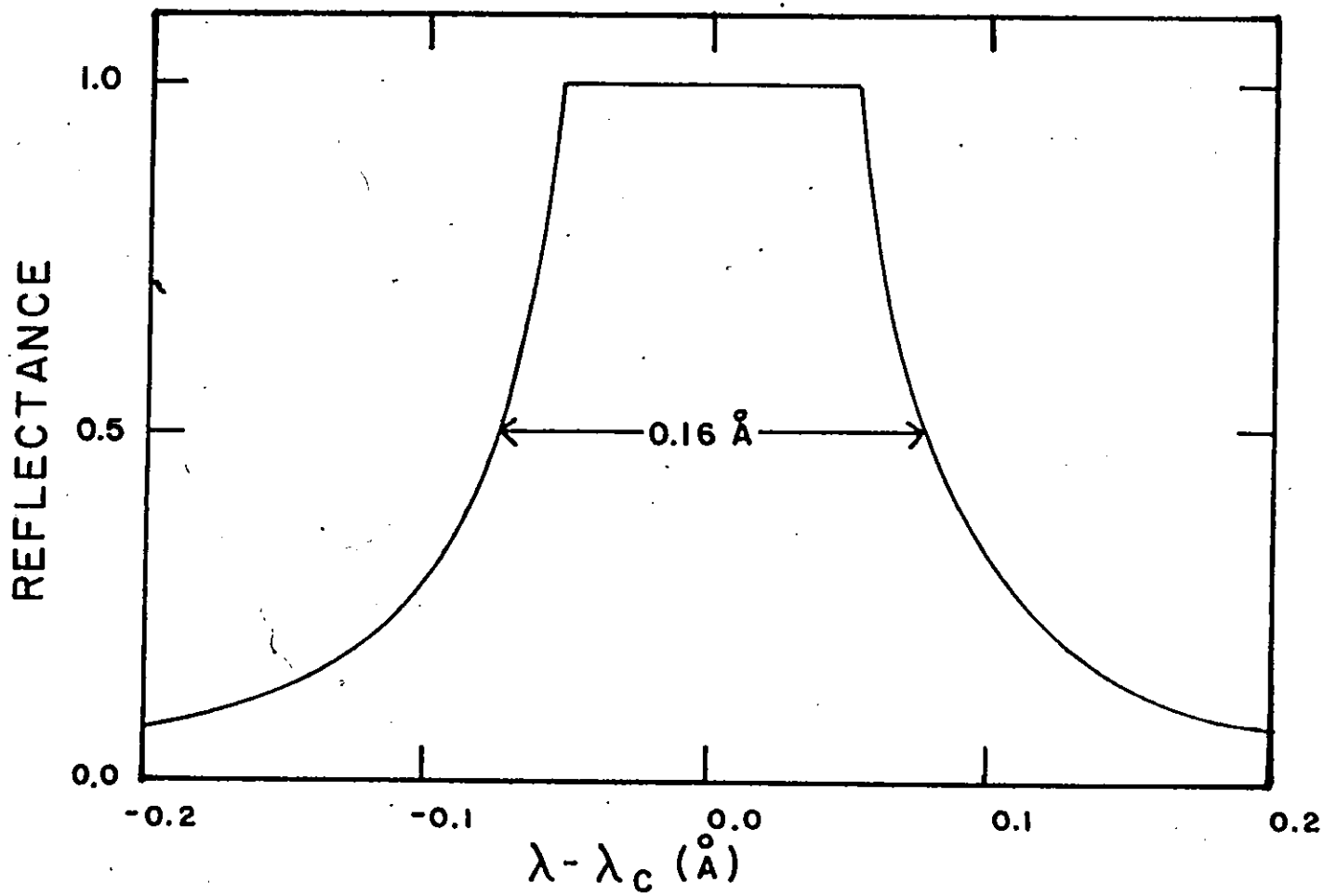
REFLECTANCE
1.0
0.5
0.0
0.16 Å
-0.2
-0.1
0.0
0.1
0.2
λ - λc (Å)

FIGURE 2.4

Normalized theoretical spectral reflectance curve ($R(\lambda)$) for the case of physical length shorter than the effective cutoff length of the filter. The value of the induced index perturbation ($\Delta\varepsilon$) is 1.2×10^{-4} and $\lambda - \lambda_c$ represents the deviation of wavelength (λ) from the Bragg wavelength (λ_c). The full width half maximum is 0.136 Å as shown.

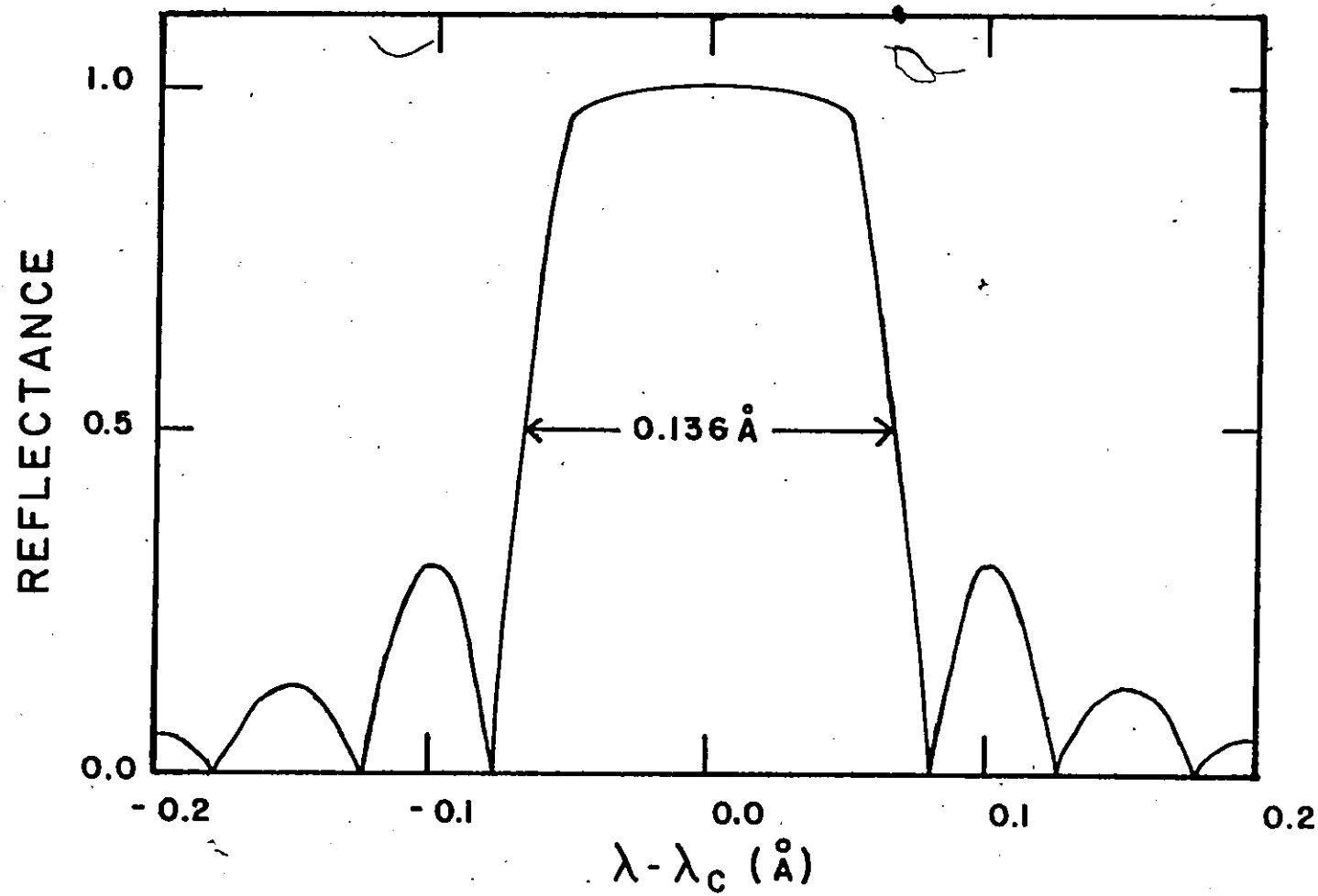
REFLECTANCE
1.0
0.5
0.0
0.136 Å
- 0.2
- 0.1
0.0
0.1
0.2
λ - λc (Å)

FIGURE 2.5

Theoretical reflectance as a function of the filter length at Bragg wavelength (λ_c) for a value of the induced index perturbation equal to 1.2×10^{-4}. The effective cutoff length (L_{cutoff}) is 0.94 cm as shown.

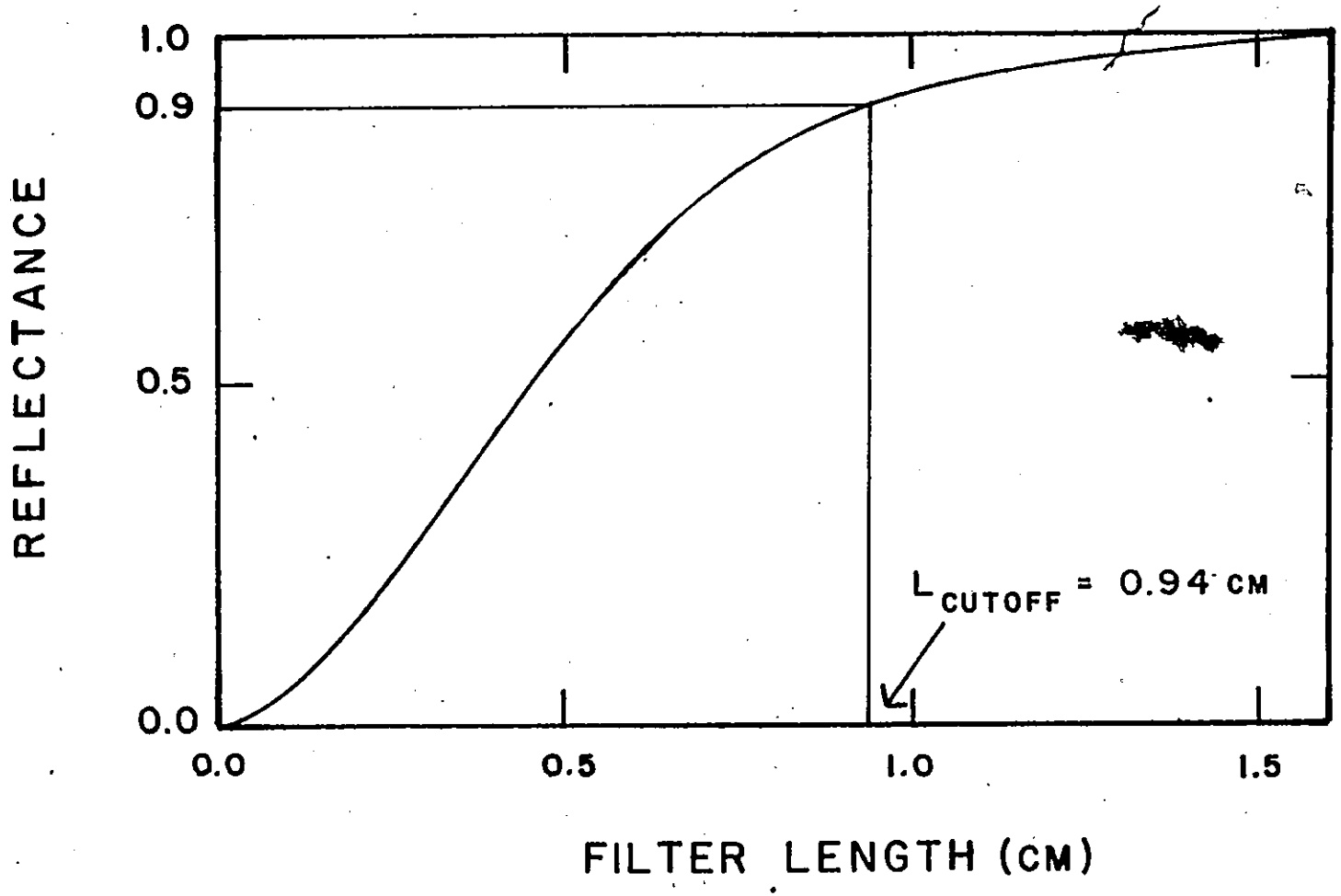
1.0
0.9
0.5
0.0
REFLECTANCE
0.0
0.5
1.0
1.5
FILTER LENGTH (CM)
L CUTOFF = 0.94 CM

FIGURE 2.6

Theoretical spectral reflectance curves ($R(\lambda)$) (for the case of physical length much larger than the effective cutoff length of the filter) as a function of the induced index perturbation ($\Delta\varepsilon$). Curves A, B and C correspond to $\Delta\varepsilon$ of 3.0×10^{-4}, 2.0×10^{-4} and 1.0×10^{-4} respectively, and have spectral bandwidths of 0.386 Å, 0.254 Å and 0.133 Å respectively. $\lambda - \lambda_c$ is the deviations of the wavelength (λ) from the Bragg wavelength (λ_c).

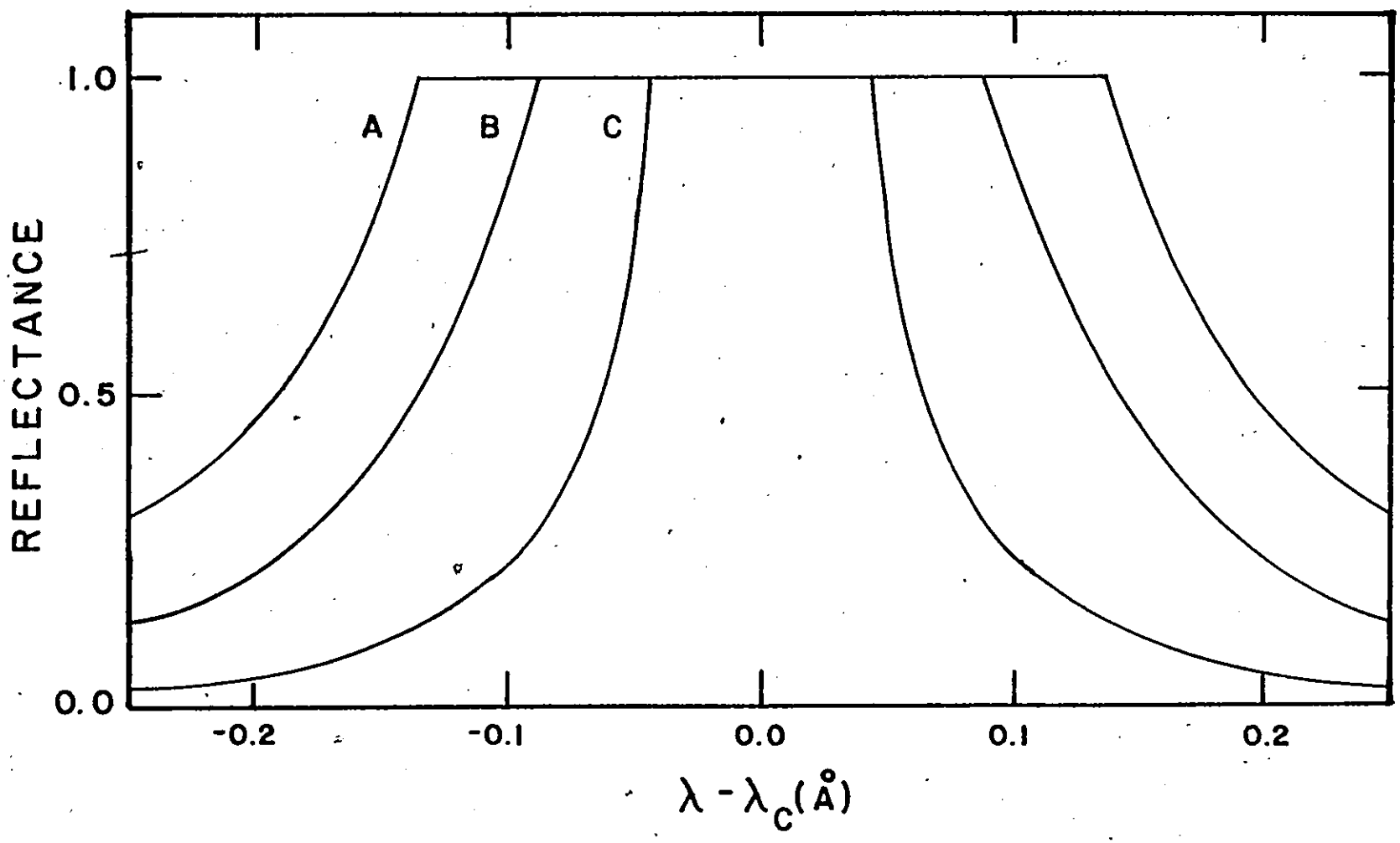
REFLECTANCE
1.0
0.5
0.0
A
B
C
-0.2
-0.1
0.0
0.1
0.2
λ - λc(Å)

FIGURE 2.7

Normalized theoretical spectral reflectance curves ($R(\lambda)$) as a function of the induced index perturbation ($\Delta\varepsilon$) for the case of physical length shorter than the effective cutoff length of the filter. Curves A, B and C correspond to $\Delta\varepsilon$ of 3.0×10^{-8}, 2.0×10^{-4} and 1.0×10^{-4} respectively, and have spectral bandwidths of 0.344 Å, 0.228 Å and 0.112 Å respectively. $\lambda - \lambda_c$ is the deviation of wavelength (λ) from the Bragg wavelength (λ_c).

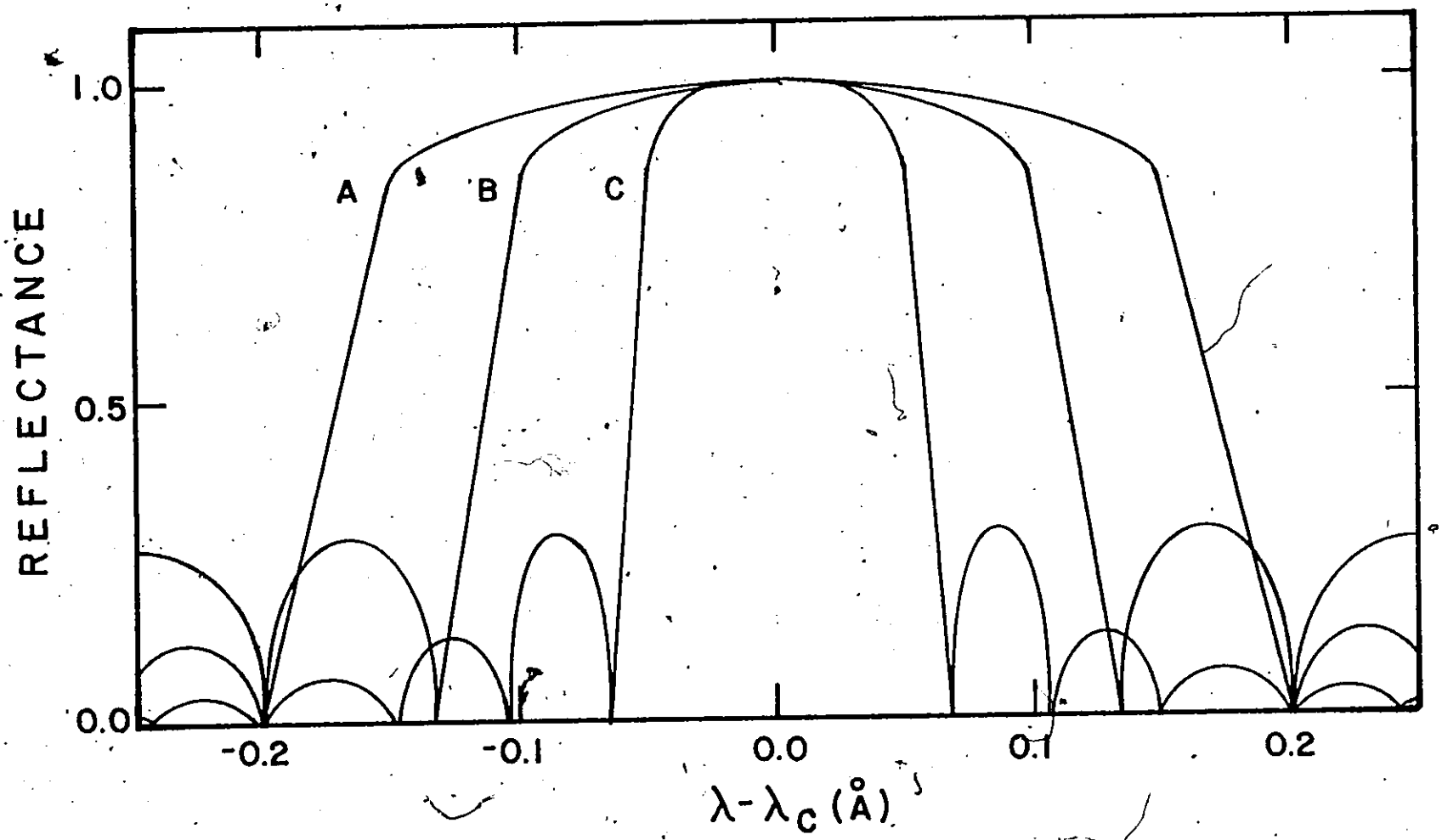
REFLECTANCE
1.0
0.5
0.0
A
B
C
-0.2
-0.1
0.0
0.1
0.2
λ-λc (Å)

FIGURE 2.8

Theoretical reflectance as a function of the filter length at Bragg wavelength (λ_c) for different values of induced index perturbation ($\Delta\varepsilon$). Curves A, B and C correspond to $\Delta\varepsilon$ of 3.0×10^{-4}, 2.0×10^{-4} and 1.0×10^{-4} respectively, and have effective cutoff length (L_{cutoff}) of 0.376 cm, 0.565 cm and 1.129 cm respectively.

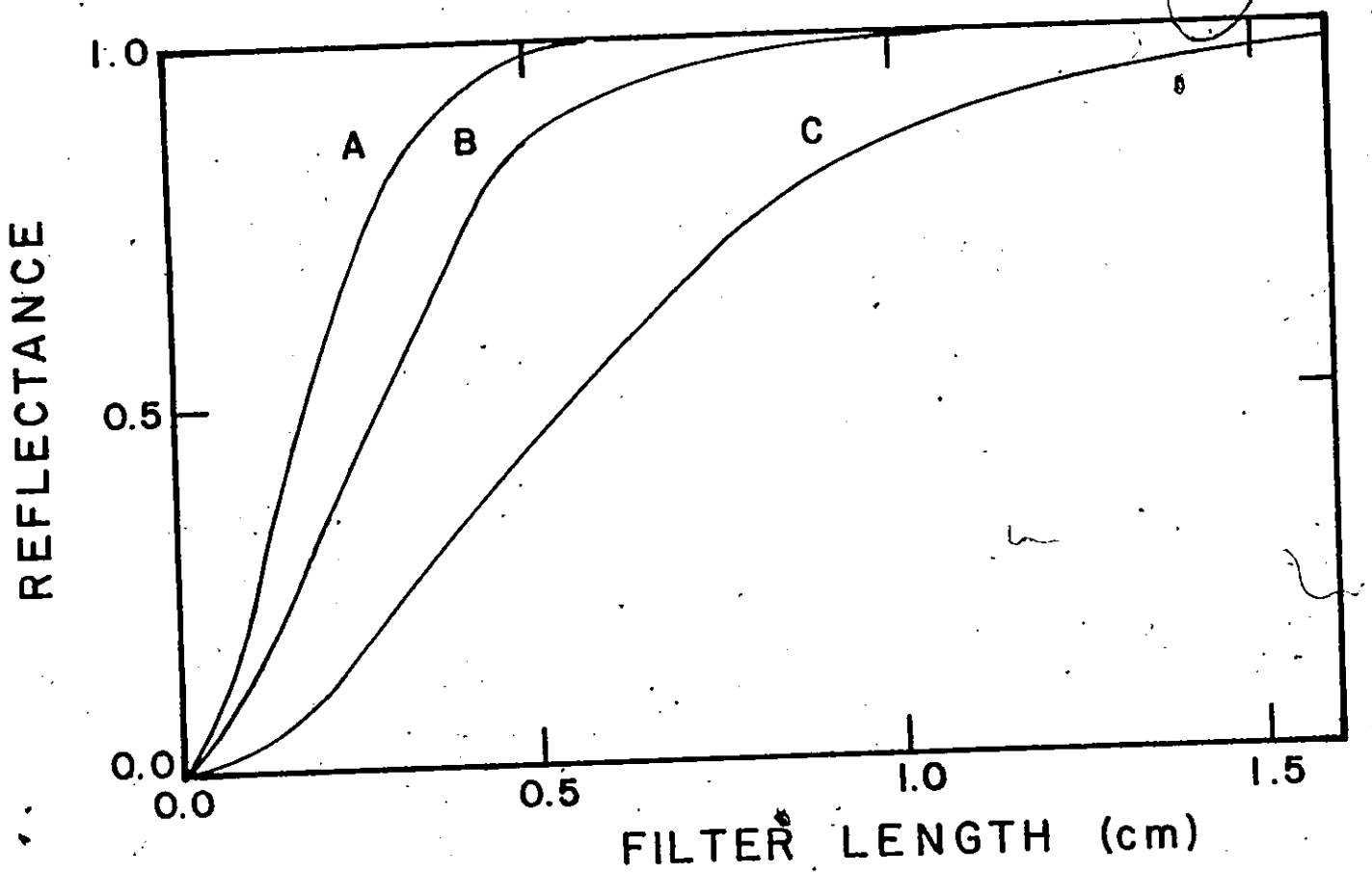
1.0
0.5
0.0
REFLECTANCE
A
B
C
0.0
0.5
1.0
1.5
FILTER LENGTH (cm)

FIGURE 2.9

Theoretical spectral bandwidth of the optical fibre filters as a function of the induced index perturbation. Line A represents the case of physical length less than effective cutoff length of the filters whereas line B represents the inverse case.

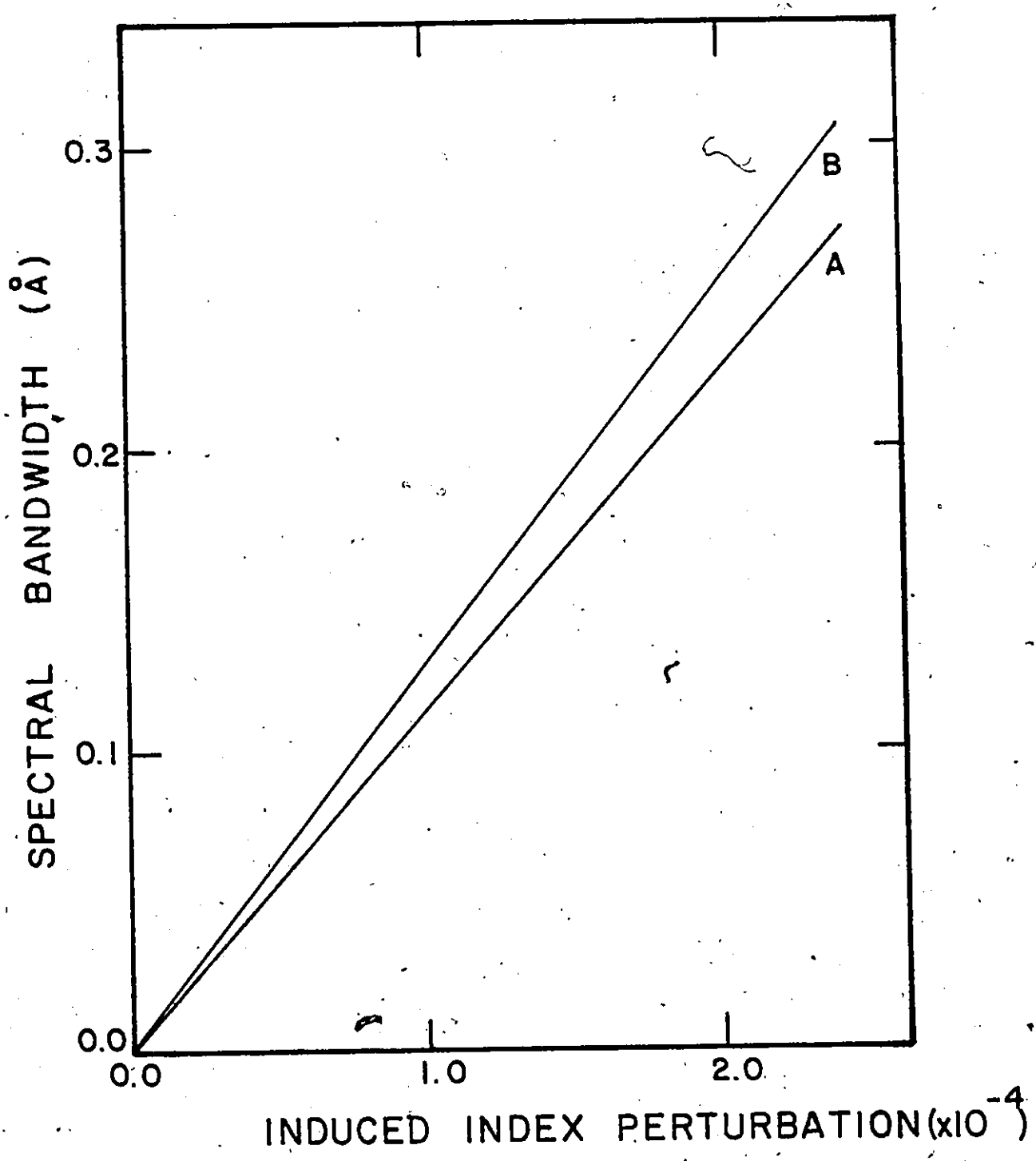
0.3
0.2
0.1
0.0
SPECTRAL BANDWIDTH (Å)
B
A
0.0
1.0
2.0
INDUCED INDEX PERTURBATION (x10^{-4})

FIGURE 2.10

Theoretical effective cutoff length of optical fibre filters as a function of the induced index perturbation.

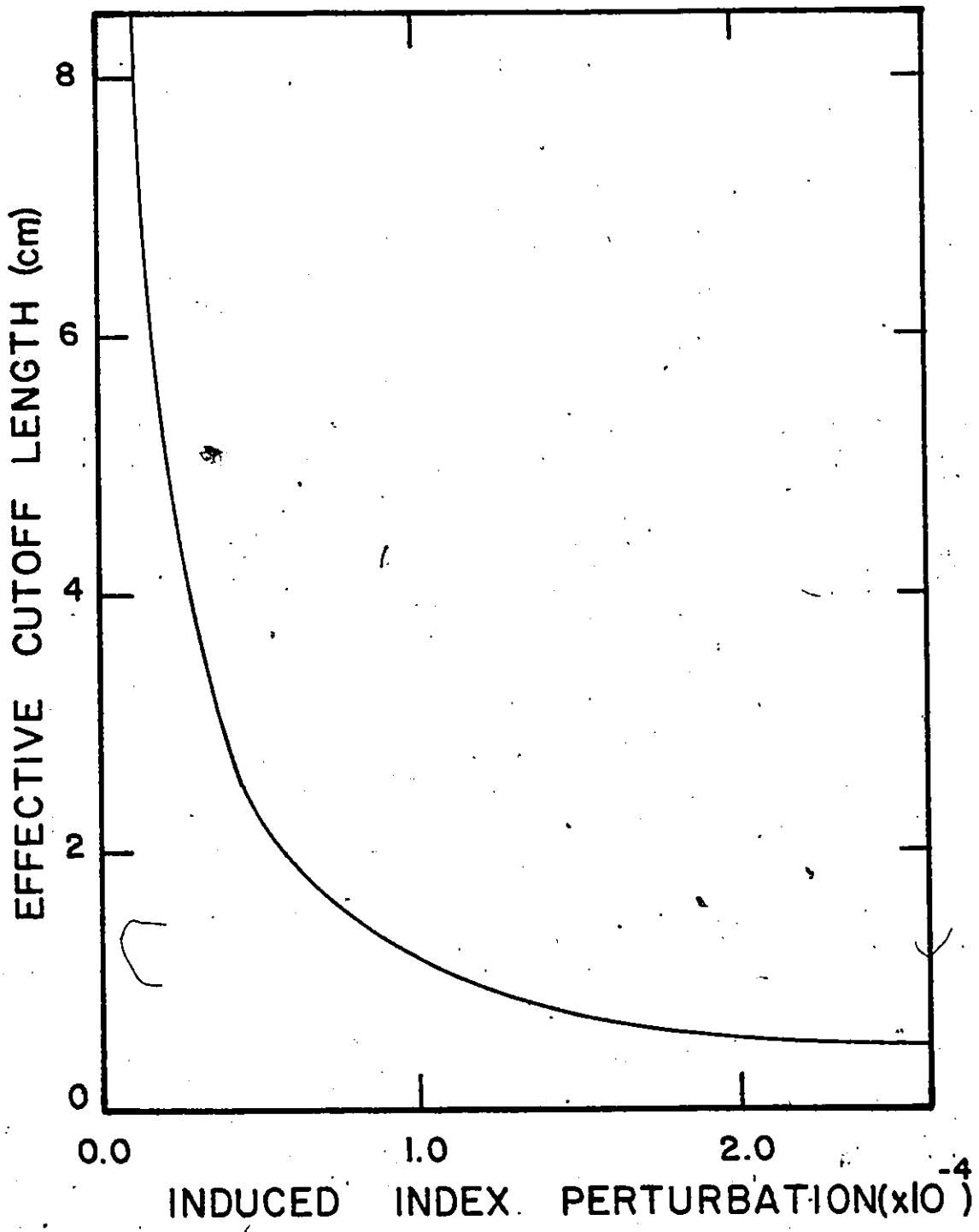
EFFECTIVE CUTOFF LENGTH (cm)
8
6
4
2
0
0.0
1.0
2.0
INDUCED INDEX PERTURBATION(x10^-4)

values of $\Delta\varepsilon > 8 \times 10^{-5}$.

Returning to Eqs. (2.52), (2.63) and (2.64), the quantity $\Delta\beta_p$ can be determined by substituting the latter two equations into the first one and finding expressions for the phase and amplitude. From the phase factor, the perturbed propagation constant is found out to be

$$\beta_p = \frac{\pi}{\Lambda} \pm ((\beta_\varepsilon - \frac{\pi}{\Lambda})^2 - \Omega^2)^{1/2} \tag{2.68}$$

where

+ sign is for $\lambda < \lambda_c$

− sign is for $\lambda > \lambda_c$

β_ε = eigen propagation constant, and

λ_c = Bragg wavelength.

In the stopband region, β_p is complex whereas in the passband region, β_p is real. It is important to mention here that the fact β_p is complex in the stopband region does not mean radiation or absorption loss but rather, it indicates that the wave is propagating with decreasing amplitudes due to coupling to the other wave. Figure 2.11 shows $\beta_p - \beta_c$, where β_c is the Bragg propagation constant, for both the stopband and passband regions.

Having obtained β_p, $\Delta\beta_p$ is easily found by forming

$$\Delta\beta_p = \beta_p - \beta_\varepsilon.$$

and a typical curve is shown in Fig. 2.12.* Referring to this figure,

---

* Singularities at $\lambda=\lambda_1$ and λ_2 are due to the fact that we have assumed a totally lossless waveguide. Introduction of a small loss eliminates these singularities.

FIGURE 2.11

Theoretical deviation of the perturbed propagation constant (β_p) from the Bragg propagation constant (β_c) as a function of the wavelength (λ) deviation from the Bragg wavelength (λ_c) in an optical fibre whose induced index perturbation is 1.2×10^{-4}.

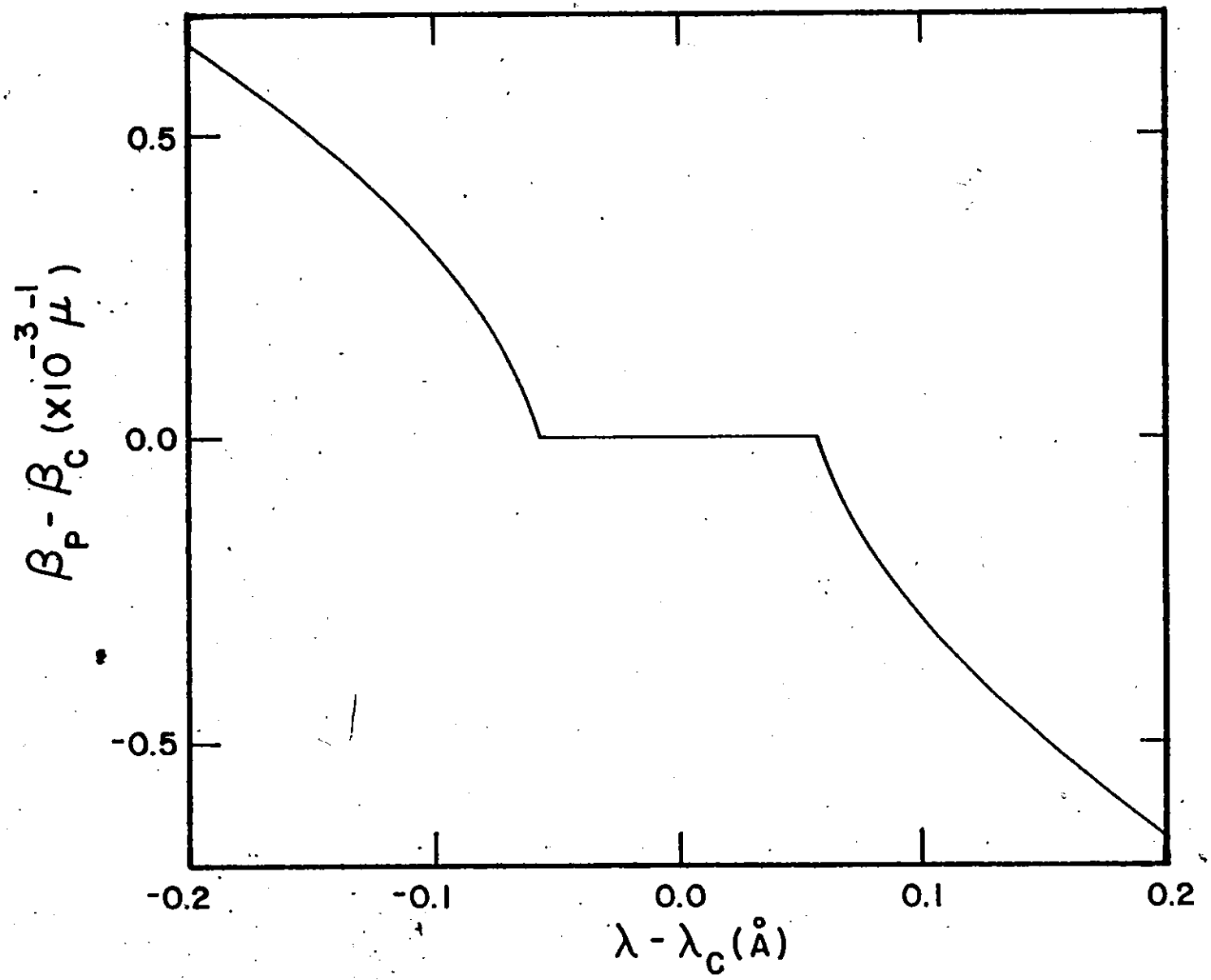
0.5
0.0
-0.5
$\beta_P - \beta_C$ ($\times 10^{-3}$ μ^{-1})
-0.2
-0.1
0.0
0.1
0.2
$\lambda - \lambda_C$ (Å)

FIGURE 2.12

Theoretical deviation of the perturbed propagation constant (β_p) from the eigen propagation constant (β_ε) as a function of the wavelength (λ) deviation from the Bragg wavelength (λ_c) in an optical fibre filter whose induced index perturbation is 1.2×10^{-4}. λ_1 and λ_2 are the wavelength at which $|\beta_p - \beta_\varepsilon|$ is maximum.

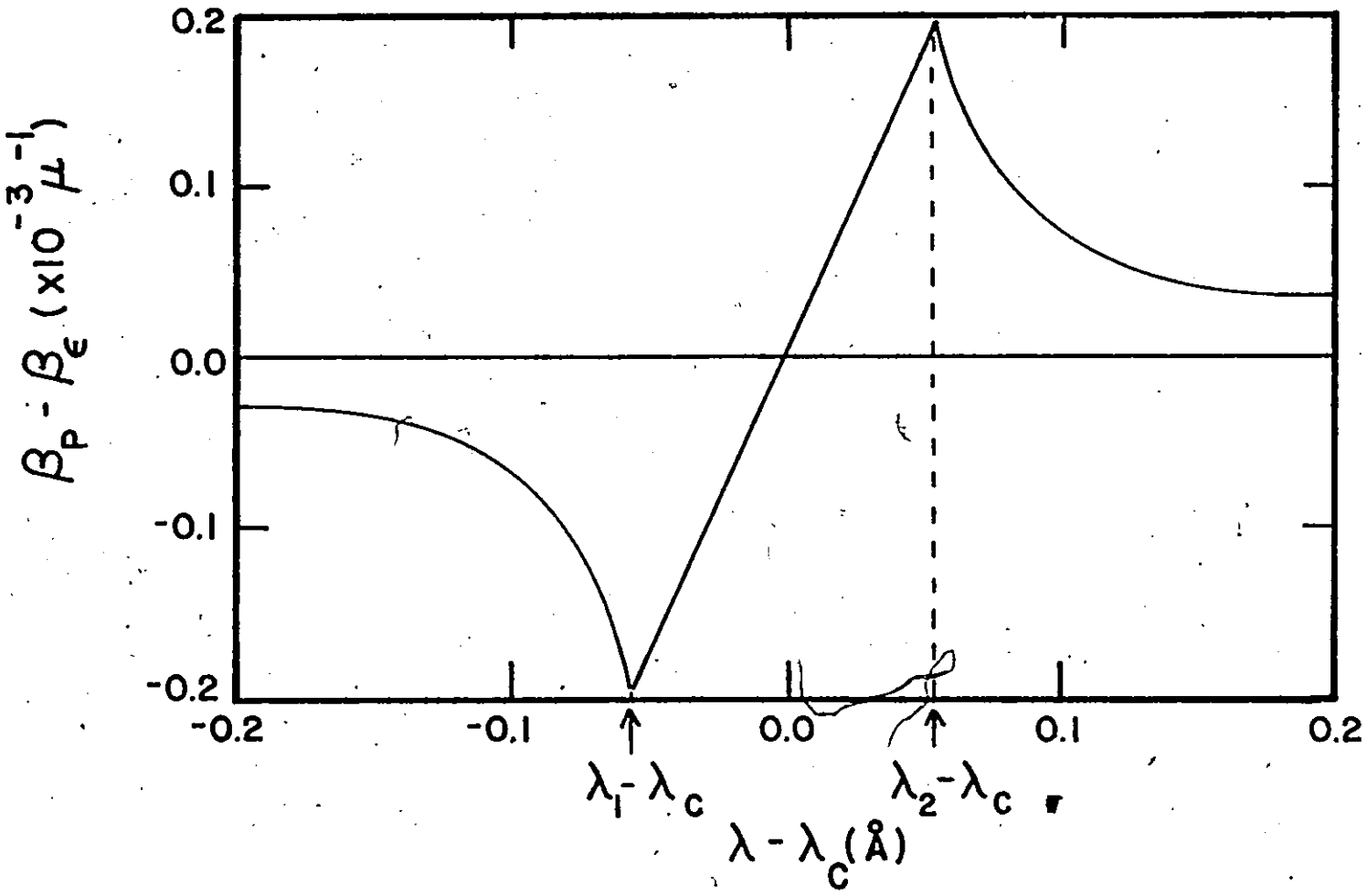
0.2
0.1
0.0
-0.1
-0.2
$\beta_p - \beta_\epsilon$ ($\times 10^{-3}\ \mu^{-1}$)
-0.2
-0.1
0.0
0.1
0.2
$\lambda_1 - \lambda_c$
$\lambda_2 - \lambda_c$
$\lambda - \lambda_c$ (Å)

the most interesting feature about $\Delta\beta_p(\lambda)$ is that it is anomalous in the stopband region. What it implies is that the propagation constant increases as a function of wavelength* and consequently the group velocity is a decreasing function of wavelength. One of the uses that can be made from this is to equalize material dispersion in optical fibres which have an increasing group velocity as a function of wavelength. This subject of equalizing material dispersion by a filter ~~will be discussed~~ in further details at a later stage.

If $\Delta\varepsilon$ is allowed to increase, the peak to peak value of $\Delta\beta_p$ which is defined as

$$\Delta\beta_{pp} = |\Delta\beta_p(\lambda_1) - \Delta\beta_p(\lambda_2)| \tag{2.70}$$

where λ_1 and λ_2 are the roots of $\Omega^2 = \Delta\beta^2$ and were shown in Fig. 2.12, will increase accordingly. From the fact that in the stopband region,

$$\Delta\beta_p = \frac{\pi}{\Lambda} - \beta_\varepsilon \tag{2.71}$$

Equation (2.70) can therefore be written as

$$\Delta\beta_{pp} = |(\beta_\varepsilon(\lambda_1) - \beta_\varepsilon(\lambda_2)| \tag{2.72}$$

Hence, the greater the separation between λ_1 and λ_2 (i.e. larger $\Delta\lambda_t$, stopband width and $\Delta\varepsilon$), the greater will be the difference between $\beta_\varepsilon(\lambda_1)$ and $\beta_\varepsilon(\lambda_2)$, and thus $\Delta\beta_{pp}$ will also be larger.

---

* This phenomenon is similar to the region of anomalous dispersion where $dn/d\lambda > 0$ near the absorption bands in optical materials.

2.4 SUMMARY AND REMARKS

It was demonstrated in this chapter that $\Delta\lambda_t$ and $\Delta\beta_{pp}$ are both linearly increasing functions of $\Delta\varepsilon$. However, L_{cutoff} decreases nonlinearly with $\Delta\varepsilon$, tending to saturate at large $\Delta\varepsilon$. There is not any saturation behaviour in $\Delta\lambda_t$ or $\Delta\beta_{pp}$ as predicted by the theory here although there may actually be for sufficiently high $\Delta\varepsilon$. Also, at very large $\Delta\varepsilon$, L_{cutoff} becomes very small and the fast spatial variation terms of $e^{\pm i\theta z}$ and $e^{\pm i2\theta z}$ may become significant. For $\theta = 2\pi/\Lambda$ and Λ of the order of micron, the fact that L_{cutoff} is saturating at large $\Delta\varepsilon$ in a sense guarantees θL will always be large enough to yield an effective zero average from $e^{\pm i\theta L}$ and $e^{\pm i2\theta L}$ terms.

The assumption of sinusoidal index profile is based on the idea that a standing wave pattern is required in order to perturb the refractive index. For small perturbation which corresponds to low writing power, a gradual change of the refractive index is expected. At high writing power, saturation and other nonlinear effects may well occur and thereby making the periodic index profile nonsinusoidal. An experiment that can determine the index profile is to write a grating on a piece of bulk GeO_2 glass and subsequently examine its far field diffraction pattern. If the index profile is indeed purely sinusoidal, then there should only be the zero and ± 1 orders in the diffraction pattern [45-46]. If higher diffracted orders are presented as well, then the index profile must have higher harmonics.

Finally, the assumption of single mode operation in a fibre that can actually support 3 modes need some justification. If the higher 2

order modes carry significant average intensity in comparison with the first mode, then ν should be extended to 3 in Eq. (2.57) and there will be more than one overlap integral in that equation instead of only I_{11_t}. In Appendix C, the average intensity of the three modes in the core region of the fibre are calculated and the results are shown in Table 2.1. From this, it can be seen that the first mode carries significantly larger average intensity than the higher modes and hence our assumption of single mode operation is valid. In other words, the spatial extent of the higher order modes is greater than that of the first order mode, and so the filter writing capability, is much less.

TABLE 2.1

The average intensity carried by the three modes in the core region of the near single mode optical fibre.

Mode No.	Average Intensity (arbitrary units)
First (HE_{11})	17
Second (HE_{21} or EH_{01})	1
Third (HE_{21} or EH_{01})	1

CHAPTER 3

EXPERIMENTS AND RESULTS

3.1 INTRODUCTION

In the previous chapter a theory was presented for the reflectance from (or equivalently transmittance through) a fibre filter as a function of the photoinduced index ($\Delta\varepsilon$) variation and filter length. In this chapter, we describe experiments aimed at exploiting the intercomparison of this theory and experiments to deduce the induced index change in fibre filters for typical values of Argon laser writing power. In order to do this, a filter is first written with a particular value of Argon laser power coupled into the fibre. Subsequently, this fibre filter is progressively shortened, and the variation in the reflectance of the filter at the writing wavelength is determined. Comparison of these observations with the predictions of the theory then allows the value of the photoinduced index to be deduced. This approach works well at low to moderate writing power. However, examination of Fig. 2.10 shows that this technique becomes increasingly insensitive for higher values of induced index, which corresponds to higher writing power. It turns out that the observed range of induced index perturbation is such that, for higher values of available writing power, the above method develops such high uncertainty in $\Delta\varepsilon$ as to become impractical. Consequently, an alternate method is required at the upper end of the range of available writing power. Examination of Fig. 2.9

shows that for values of $\Delta\varepsilon$ in the range $\geq 1.4 \times 10^{-4}$, the spectral bandwidth of a given filter is commensurate with the spectral resolution of a typical monochromator. Accordingly, for the higher values of writing power, we have made direct measurements of the spectral bandwidth of a given filter in order to deduce the induced index change.

In this chapter, the technique employed to produce fibre filters is reported, followed by a description of the above mentioned experimental approaches to measuring the filter characteristics. The results obtained are illustrated for specific filters, but detailed fitting of the theory to the experimental observations is deferred to Chapter 4.

3.2 THE METHOD OF FABRICATING OPTICAL FIBRE FILTERS

3.2.1 Experimental Preparation and Method

In order to write a filter successfully, one must ensure that (1) the initial preparation of the fibre is done properly, (2) the experimental setup is properly aligned and possesses a high coupling efficiency (η_{coup}), and (3) the environment around the experiment is acceptable in terms of the mechanical and temperature stability. The degree of difficulty in satisfying (1), (2) and (3) is in an increasing manner and as it will be shown later, environmental stability poses many problems throughout the experiment.

The proper way to prepare a fibre is to first of all strip off its jacket for 2 to 3 inches at each end by dissolving it in chloroform. Both ends are then cleaved with a diamond edge and examined under a microscope in order to ensure that they are plane perpendicular to the fibre axis. The reason that this is essential is because the writing of

a filter requires an optical standing wave pattern and will only reflect the lowest order mode HE_{11}*. When the input end is not plane perpendicular to the fibre axis, the higher order modes of HE_{21}* and EH_{01}* will be excited instead of HE_{11} and satisfactory filters can not be produced. On the other hand, when the output end is not plane perpendicular to the fibre axis, the 4% Fresnel reflection from it will not be strongly coupled back into HE_{11} and consequently there will not be the required optical standing wave pattern. The reason why a filter can only reflect the lowest order mode HE_{11} will be discussed at a later stage.

After the proper preparation of a fibre was done, it was mounted in the experimental set-up which is basically the same as that reported by Hill and Kawasaki [21,47]. Hence only a brief review with additional information where necessary will be given here. Figure 3.1 shows the experimental set-up in which a 1 watt Argon green single mode, single line laser was used to irradiate the fibre. In order to obtain a set of filters with different writing powers, a variable attenuator was placed in front of the Argon laser with great care so that the back reflected beam from it would not be coupled back into the laser and cause instability or mode hopping. A 50% beam splitter was used so as to allow the monitoring of the buildup in the reflectance of the filter as it was being written. The absorber was used to reduce unwanted scattering of light during the experiment. In order to couple the laser

---

* Linearly Polarized Fields.

FIGURE 3.1

Schematic of the apparatus for the fabrication of optical fibre filters. The Argon laser is oscillating on a single longitudinal mode at 0.5145 μ with .1 Watt of output power. The 50x microscope objective and the quartz clamp are mounted on a micropositioner and a piezoelectric micropositioner respectively. The fibre is allowed to hang loose between the input and output ends without any stretching.

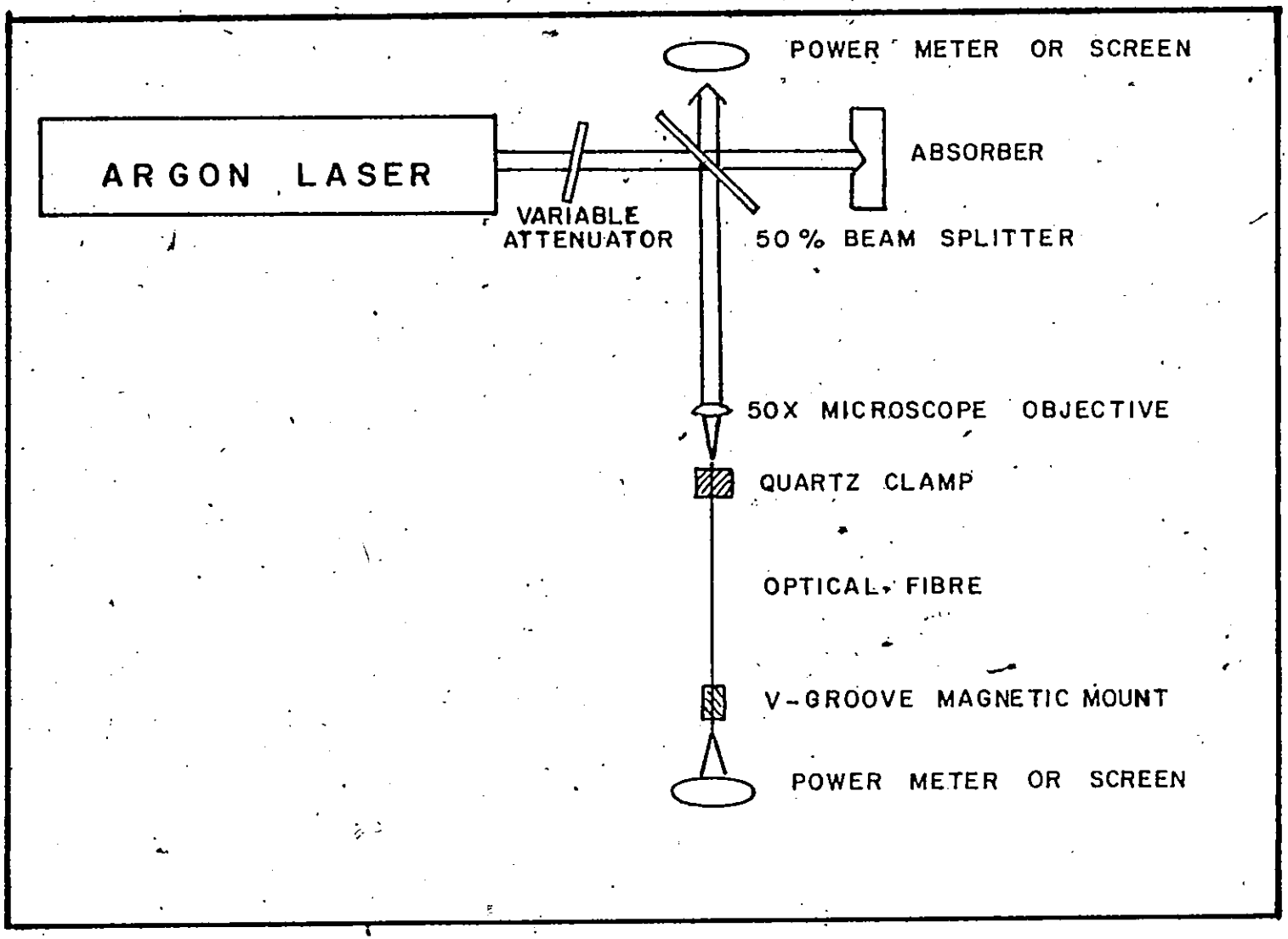
POWER METER OR SCREEN
ARGON LASER
ABSORBER
VARIABLE ATTENUATOR
50 % BEAM SPLITTER
50X MICROSCOPE OBJECTIVE
QUARTZ CLAMP
OPTICAL FIBRE
V-GROOVE MAGNETIC MOUNT
POWER METER OR SCREEN

beam efficiently into the fibre, a 50X microscope objective which has a slightly larger numerical aperture than that of the fibre was used. The input end of the fibre was clamped tightly by a rigid quartz jaw whereas the output was held in place by using a V-groove magnetic mount. The fibre was allowed to hang loose without any stretching. To assist the critical alignment between the microscope objective and the input end of the fibre, they were mounted on a micropositioner and a piezoelectric micropositioner whose resolution is 40 Å/volt respectively. Light emerging from the output end of the fibre was observed on a white screen.

Alignment was done at 1 mW laser power (which is well below the level required to produce a filter) by first adjusting the micropositioners at the input end manually until a round spot was observed at the output screen. The appearance of this round spot indicates that the lowest order mode HE_{11} is excited and the laser beam is aligned with the fibre axis. A detector was then placed in front of the output end of the fibre and the micropositioners at the input ends were adjusted again both manually and piezoelectrically. A typical coupling efficiency of 40%-50% was achieved repeatedly without much difficulty in the experiment. It is worthwhile to mention here that one easy way to tell if the fibre is located correctly in the focal region is by examining the back reflected pattern. If the pattern is in the form of a round spot, the fibre is properly positioned.

With the system aligned, a fire brick was used to block the laser beam incident on the microscope objective and the variable attenuator

was adjusted to give the desired writing power. The fire brick was then removed and the writing process was monitored by observing the amount of reflected radiation and the far field pattern on the output screen.

If the system is stable in the sense that there is no mode hopping in the laser and insignificant mechanical vibration or temperature fluctuation; the reflectance from the input end of the fibre builds up continuously and smoothly until it saturates. Towards the end of the writing process, a 2 or 3 lobes pattern is observed on the output screen indicating that the lowest order mode is being strongly reflected. It is important to note that the fibre fabrication process is extremely sensitive to even very minor temperature variation. For instance, should the fibre be breathed on or a hand be placed near it, the observed reflectance will change dramatically and become unstable. It was always ensured that the system was as isolated as possible in order to achieve the best attainable thermal stability. Mechanical stability was ensured by the fact that the fibre system was arranged on a floating granite table. Upon saturation of the reflectance, the laser beam was blocked again by the fire brick and restored to 1 mW level by adjusting the variable attenuator. At this point, a filter has been made and is available for subsequent measurements.

3.2.2 Results

In all the filters fabricated, their reflectances were allowed to increase until the onset of saturation. The saturated reflectances were found to be different for different writing powers and sometimes even for the same writing power, there was still some variation from one

filter to another. On numerous occasions during the writing process, the measured reflectance dropped abruptly after it reached its maximum or even prior to it. It was observed that when the writing power was low (below 80 mW), the frequency of the rise and fall in the reflectance was higher. Also, the shorter the fibre, the more stable it was in terms of the reflectance fluctuation. When the reflectance dropped from its maximum value to some lower value, several minutes were required before it returned to its maximum value. On some occasions, the maximum reflectance was never fully regained regardless of how long the fibre was allowed to be irradiated. Rather, the reflectance would build up to a lower level and then saturate there. All these observations are consistent with the high sensitivity of the filter writing process to variations in environmental conditions. In all the cases, the writing processes were stopped when the reflectance saturated and remained constant for a period of one minute.

The far field pattern (FFP) of the light transmitted and reflected from the fibre ends were observed to have the following changes. Whereas the transmitted FFP was primarily a round spot prior to the writing process, it changed to a 2 or 3 lobes pattern with a decrease in the transmitted power. This transformation was permanent in that when the filter was later illuminated by a 1 mW laser beam, the transmitted FFP remained a 2 or 3 lobes pattern. For the reflected FFP, it remained a round spot but grew in its intensity by a factor of anywhere between 5 to 22. These changes of the FFP's at the two ends firmly indicated that only the lowest order mode was reflected by the filter.

Seven different levels of writing power were used to make filters and data on the maximum reflectance and the saturation time - time required to reach saturation - are listed in Table 3.1. In general, there does not seem to be any correlation between the writing power and the saturation time. For instance, at a fixed WP, the saturation time can vary by more than a factor of 5. The maximum reflectance however has a clearly increasing trend with respect to the WP as is shown in Fig. 3.2.

3.2.3 Discussion

The erratic nature of the fibre reflectance during the writing process is most likely due to temperature instability. This was confirmed by noting that if the fibre was breathed on or a hand was placed near to it, the reflectance would change dramatically and become unstable. As a result, a filter could not be written. Furthermore, it was observed that for writing power greater than 160 mW, a filter cannot be written due to an everchanging reflectance. The reason for this is that significant joule heating was induced at this level of writing power and therefore temperature instability arose.

To understand how temperature variation results in reflectance fluctuation, the idea of the detuning process in filters has to be introduced. As the temperature changes, the filter resonant wavelength (λ_c) (or Bragg wavelength), which is defined as the wavelength where the reflectance is maximum, changes accordingly and consequently the reflectance at the Argon wavelength (λ_{ARGON}) decreases as shown in Fig.

TABLE 3.1

Maximum reflectance and saturation time for optical fibre filters of different writing power.

Writing Power (mW)	Maximum Reflectance*(%)	Saturation Time (minutes)
35	21-30	5-14
50	37-47	4-13
70	40-50	4-14
85	55-65	3-10
100	74-90	1-3
130	70-90	1-4
140	60-90	1-5

FIGURE 3.2

Experimentally observed maximum reflectance of the optical fibre filters as a function of the writing power.

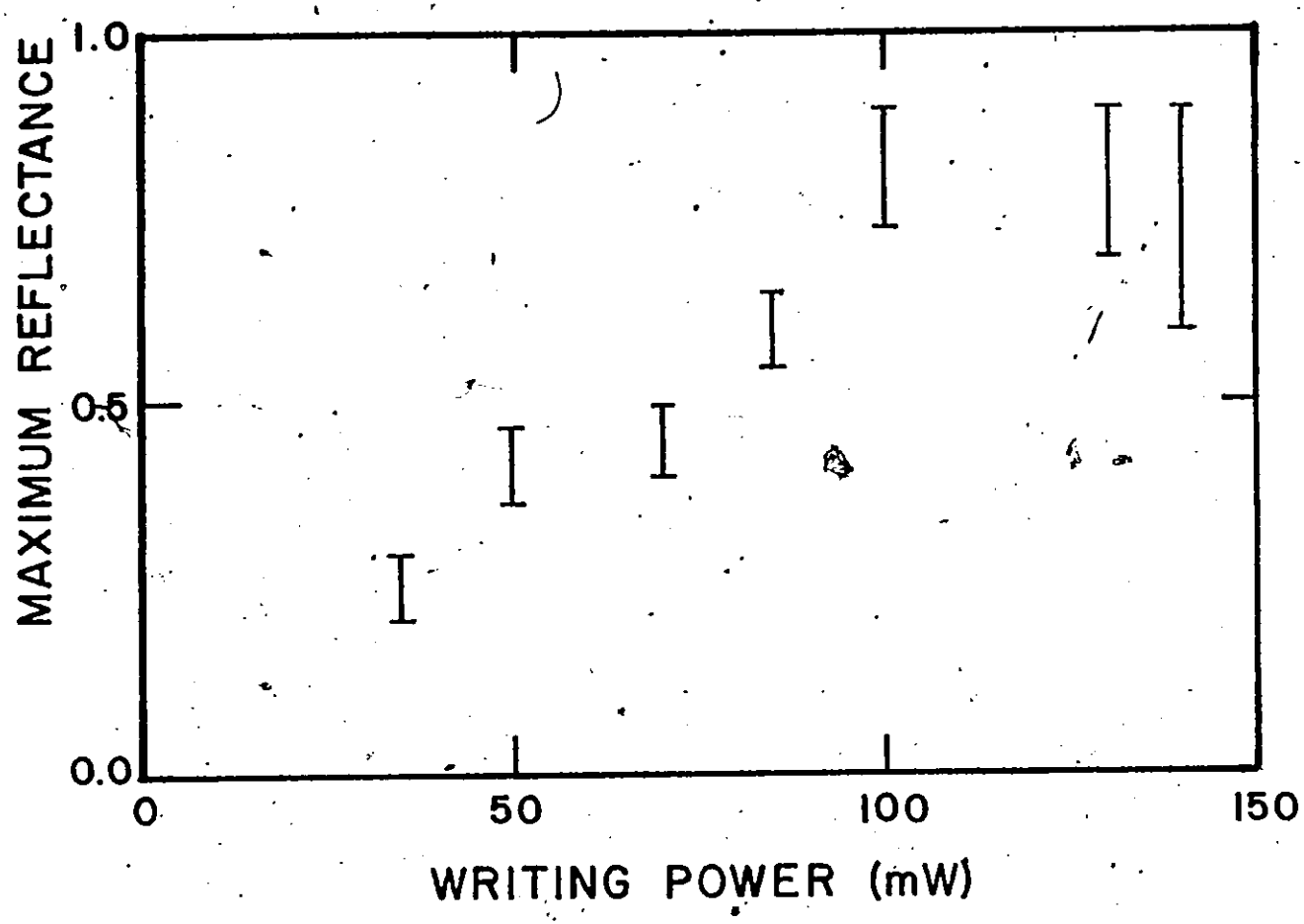
MAXIMUM REFLECTANCE
1.0
0.5
0.0
0
50
100
150
WRITING POWER (mW)

FIGURE 3.3

Illustration of the detuning process in optical fibre filters due to temperature perturbation. At the equilibrium temperature, the laser wavelength λ_{Argon} coincides with the filter resonant wavelength λ_c (Bragg wavelength) and the reflectance is R_1. When the equil[illegible]ature is perturbed, $\lambda_c \neq \lambda_{Argon}$ and the reflec[illegible] which is smaller than R_1.

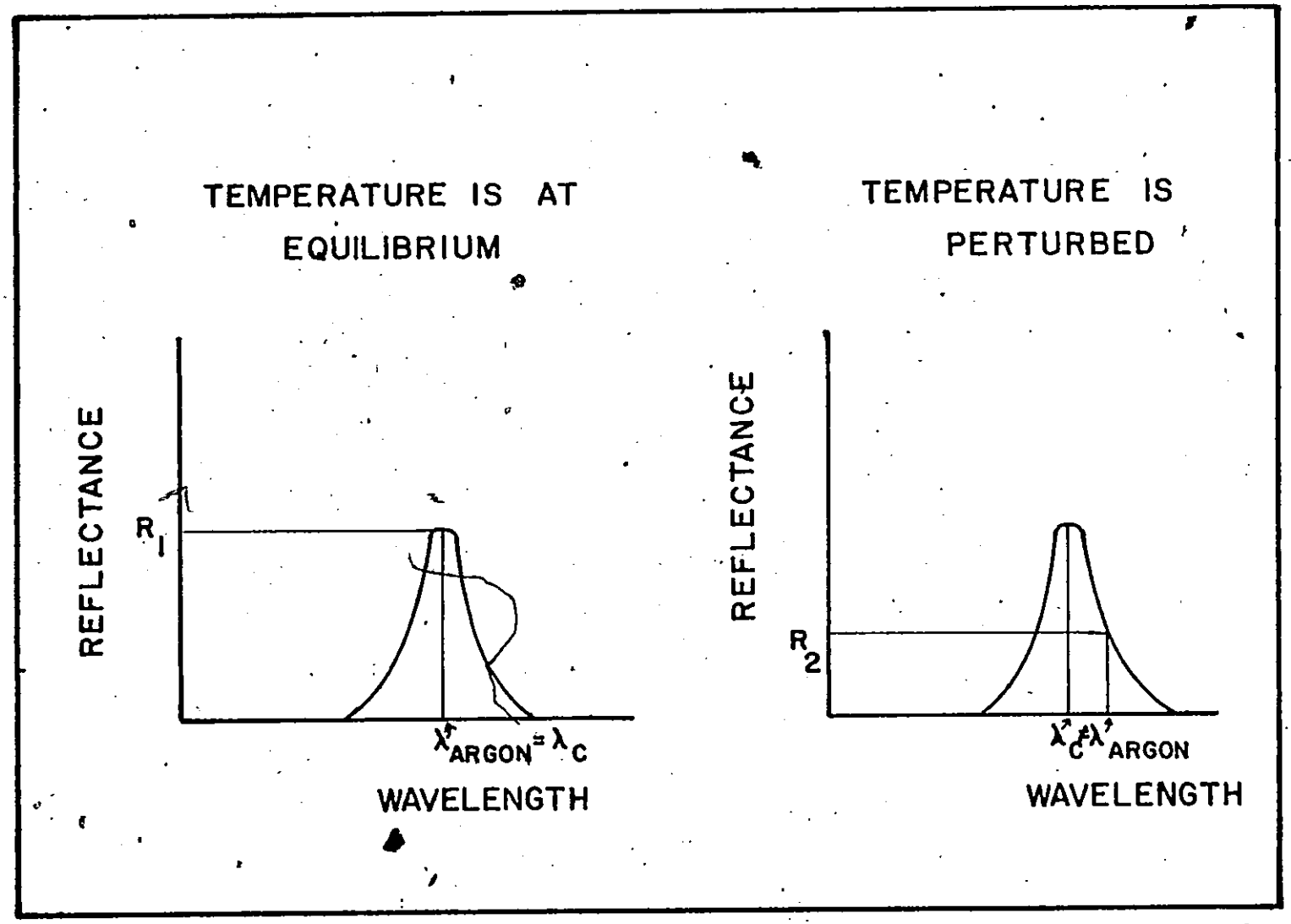
TEMPERATURE IS AT EQUILIBRIUM
REFLECTANCE
R_1
$\lambda'_{ARGON} = \lambda_C$
WAVELENGTH
TEMPERATURE IS PERTURBED
REFLECTANCE
R_2
$\lambda'_C \neq \lambda'_{ARGON}$
WAVELENGTH

3.3. If the temperature variation is temporary and of short duration, a filter can still be written. However, if the change is continuous and of long duration, then no filter can be written as the reflectance would never be able to build up smoothly.

Referring to Table 3.1, the maximum reflectance of the filters never exceed 90% and the reasons for this are as follows. First of all, the filters only reflect the lowest order mode HE_{11}, and thus, the higher order modes of HE_{21} and EH_{01} are transmitted through the filters. Secondly, there is mode coupling from HE_{11} to HE_{21} and EH_{01} as the wave propagates down the filter and hence it decreases the amount of light that will be reflected. Incidentally, because of mode coupling and the fact that the effective cutoff lengths of the filters decrease as the writing power increases (this is described in the next section), it means that filters of lower writing power have more mode coupling and vice versa. Consequently, the maximum reflectance increases as a function of the writing power and this is in fact what was observed in the experiment.

Finally, using the calculated average intensity distribution of the three modes in the fibre from Appendix C, it is easily understood why the filters can reflect only the lowest order mode. The intensities for HE_1 and EH_{01} are simply too low to write a filter at the writing powers used in this experiment. By employing higher writing power, it may be possible to write filters to reflect HE_{21} or EH_{01} if the problem of the temperature instability induced by joule heating can be eliminated.

3.3 DETERMINATION OF THE EFFECTIVE CUTOFF LENGTH OF FILTERS

3.3.1 Experimental Apparatus and Procedures

The experimental apparatus for determining the filters' effective cutoff length (L_{cutoff}), which was defined as the length of the filters at which reflectance is equal to 0.9, is the same as that for fabricating filters. Hence, it will not be repeated here and only the procedures will be given.

After a filter was made, the laser beam was reduced to 1 mW by adjusting the variable attenuator. The rest of the system was not disturbed because the initial coupling condition had to be preserved in order to obtain good and reliable results. A pair of scissors was used to cut the filters from the output end and the reflectance was measured after each cut. In order to ensure that the measured reflectance was genuinely due to the filter, the filter's cut end was submerged into suitable index matching fluid so as to eliminate any reflection from this end. This also suppresses any interference that may occur between wave reflected from the cut end and the filter. Since the theoretical curve of reflectance versus filter length roughly follows a hyperbolic tangent dependence, the amount of fibre length reduced at each cut was therefore made progressively shorter. For a fibre of initially 1 meter long, lengths of typically 15 cm were cut until the remaining length was 1/3 metre. At this point, the length to be cut was progressively shortened from 3 cm to 1/2 cm until the reflectance ceased to decrease significantly or the filter could not be cut further. The quartz jaw that held the input end of the fibre required a fibre length of roughly

1 cm and consequently all cutting processes had to be terminated there.

It should be noted here that when the remaining fibre length is short, it is inadvisable to bend it into the index matching fluid container because it has been shown [47-48] that stretching a filter can detune its resonant wavelength. As a result, the measured reflectance will be somewhat smaller than the true value. To avoid this, an eye dropper was therefore used to deposit a drop of the index matching fluid onto the cut end.

3.3.2 Results

Figure 3.4 shows curves of normalized reflectance* as a function of the filter length (R(L)) for the different levels of writing power used. The shape of the curves resembles that of the theory and indicates that L_{cutoff} decreases as a function of the writing power. Table 3.2 and Fig. 3.5 provide the summary of L_{cutoff} as a function of the writing power. Because of the fibre length limitation imposed by the quartz jaw, data in the low reflectance region for filters of high writing power could not be obtained. Consequently, their R(L) are incomplete in comparison to those of filters of lower writing power. In Figs. 3.6-3.7, fittings of theoretical R(L) to experimental R(L) are shown for two specific writing power cases and they indicate good agreement between theory and experiment. Detailed comparison and analysis of them will be presented in the next chapter.

---

* They are normalized to facilitate the comparison with the theoretical curves.

FIGURE 3.4

Experimental curves of the reflectance as a function of the filter length for different writing powers. Curves A, B, C, D and E correspond to writing powers of 100 mW, 85 mW, 70 mW, 50 mW and 35 mW respectively. The dotted curves are extrapolations of the solid curves as the quartz clamp forbids any measurement to be made for filter lengths shorter than ~1 cm.

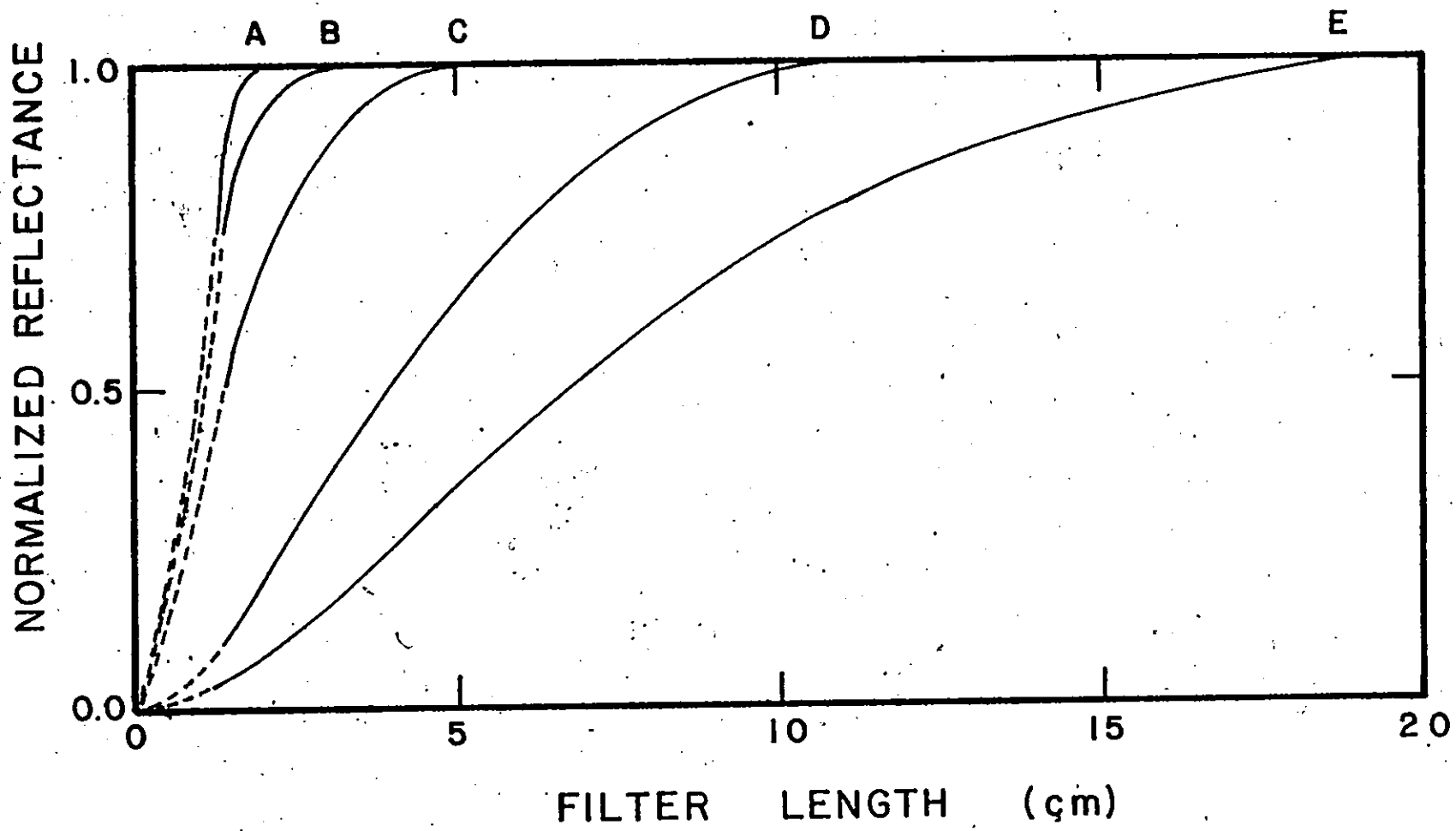
A
B
C
D
E
NORMALIZED REFLECTANCE
1.0
0.5
0.0
0
5
10
15
20
FILTER LENGTH (cm)

TABLE 3.2

Measured effective cutoff lengths (L_{cutoff}) together with their absolute and relative error as a function of the writing power.

Writing Power (mW)	Averaged L_{cutoff} $\bar{L}$(cm)	Absolute Error ΔL (cm)	Relative Error $\Delta L/\bar{L}$
35	16	±0.5	3%
50	8.2	±0.5	6%
70	3.1	±0.5	16%
85	1.7	±0.5	29%
100	1.27	±0.3	24%

FIGURE 3.5

Effective cutoff length of the filters as a function of the writing power measured in the experiments.

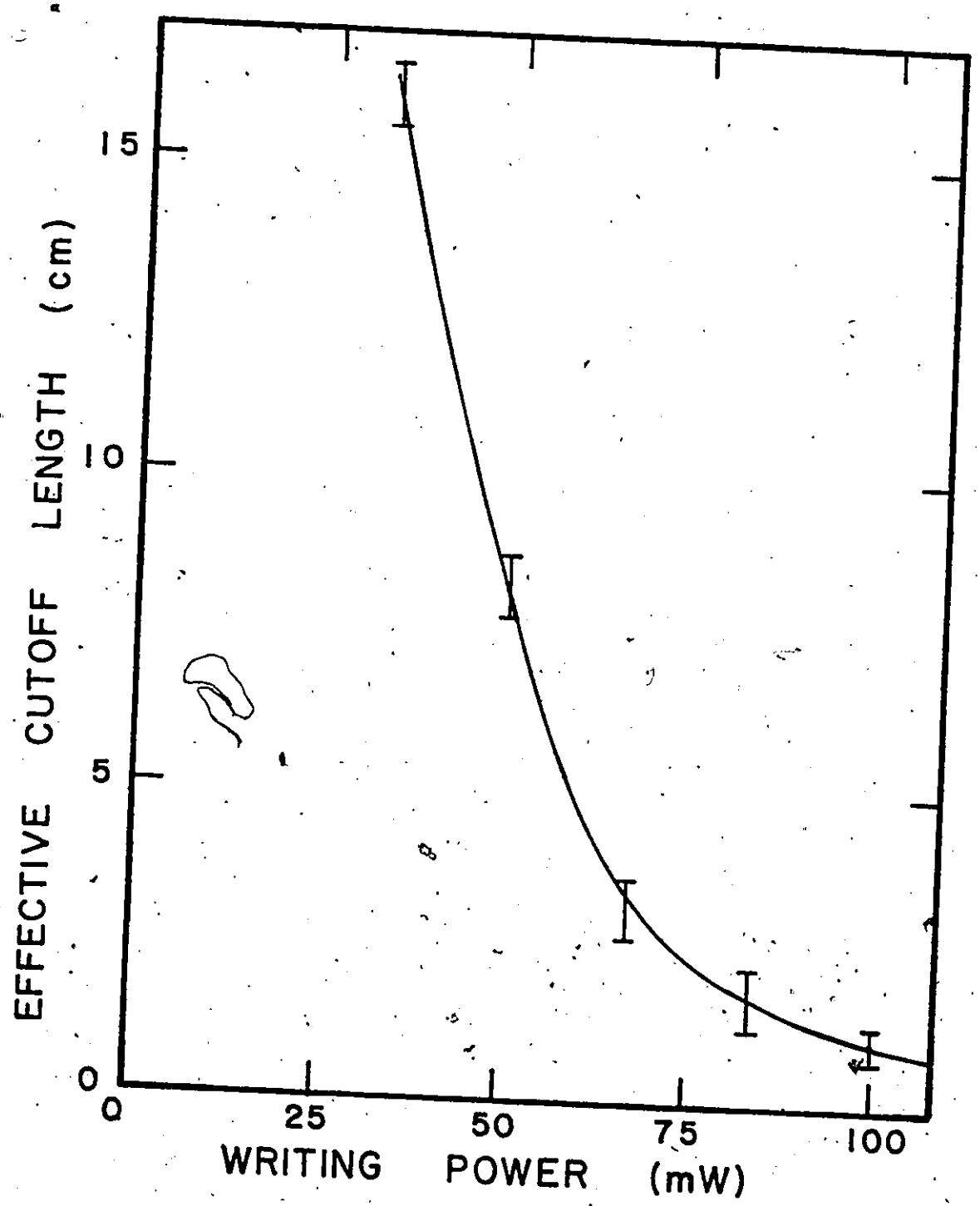
EFFECTIVE CUTOFF LENGTH (cm)
15
10
5
0
0
25
50
75
100
WRITING POWER (mW)

FIGURE 3.6

Comparison between experimental and theoretical curves of reflectance as a function of the filter length for a writing power of 50 mW.

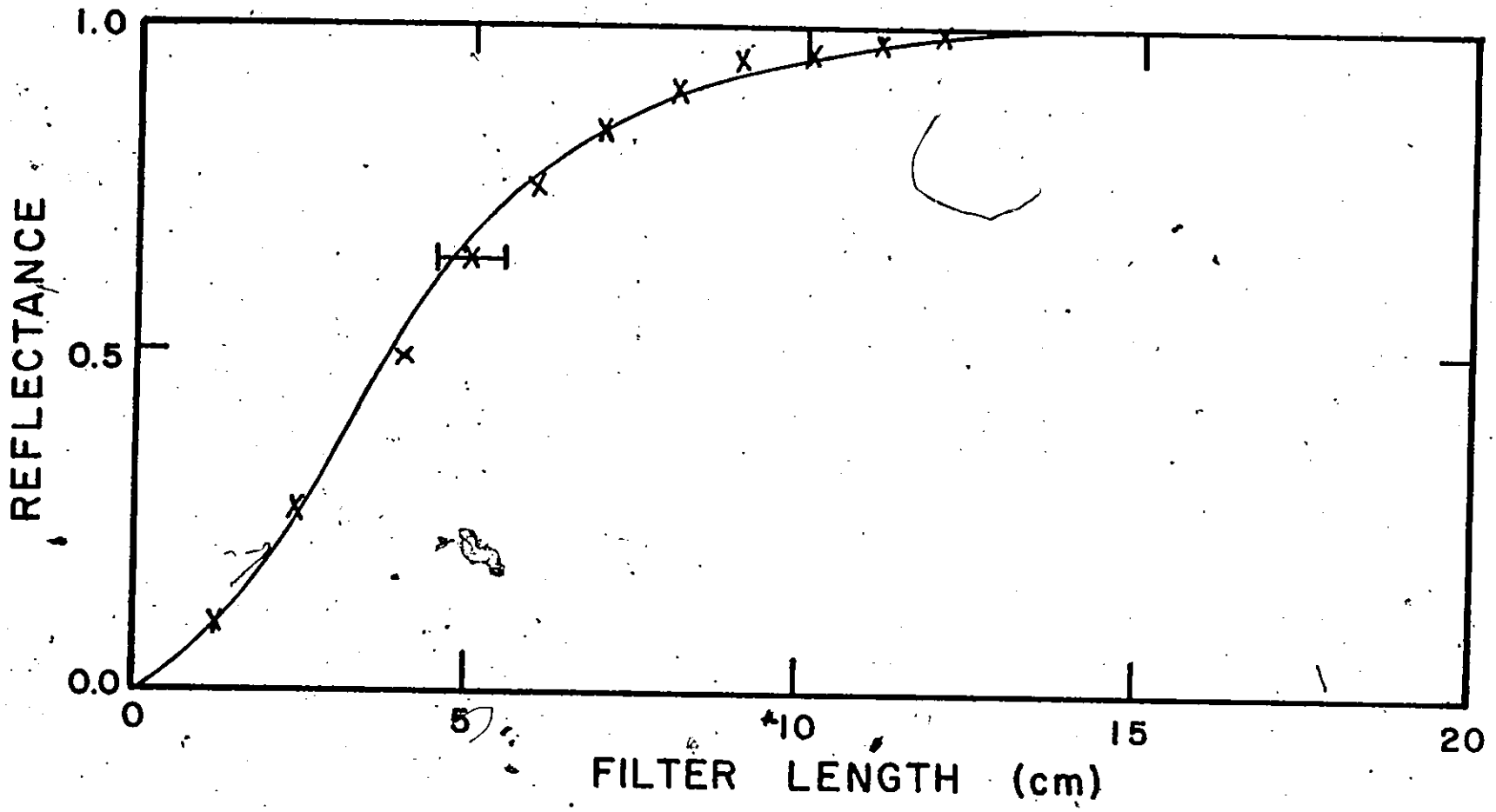
1.0
0.5
0.0
REFLECTANCE
0
5
10
15
20
FILTER LENGTH (cm)

FIGURE 3.7

Comparison between experimental and theoretical curves of reflectance as a function of the filter length for a writing power of 70 mW.

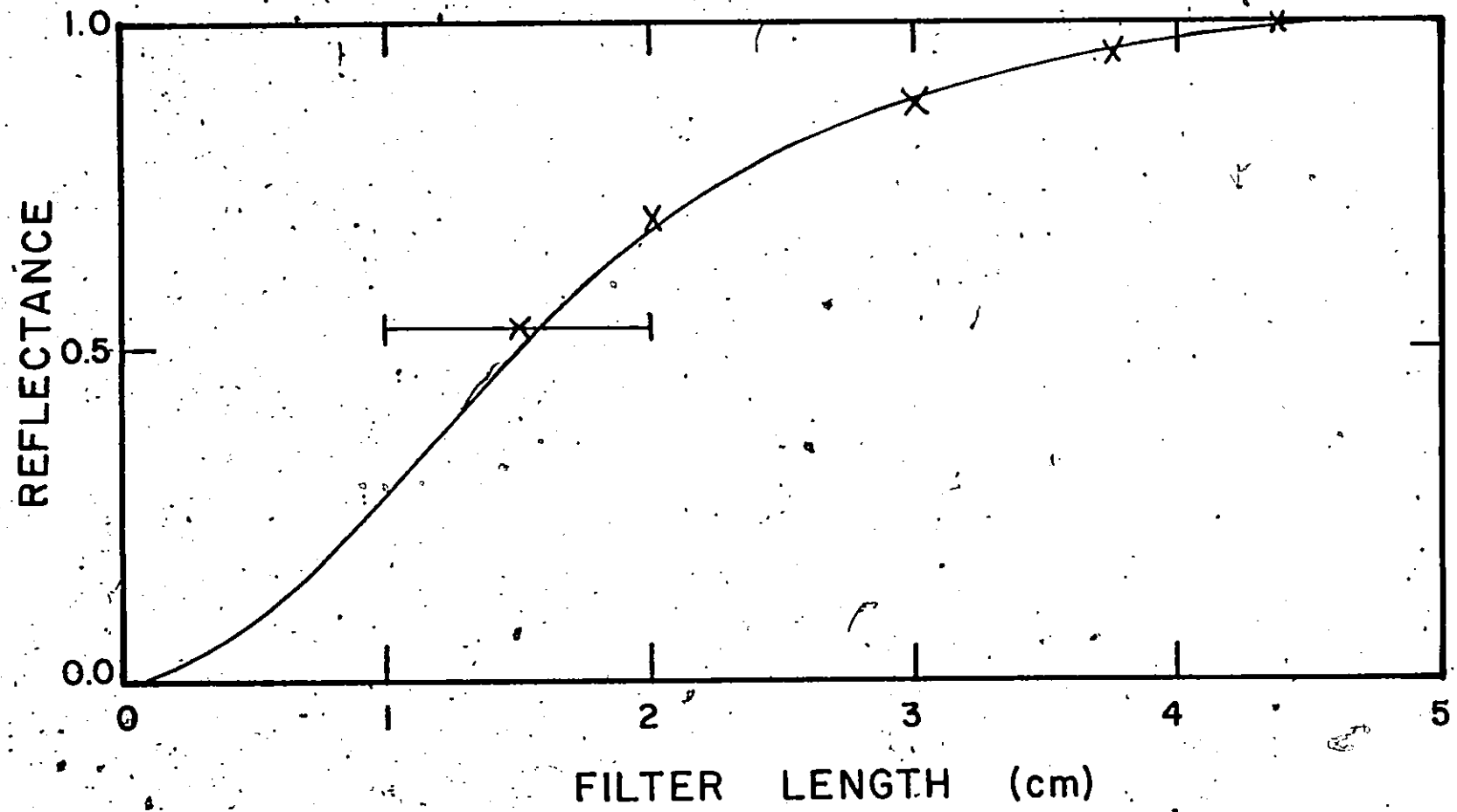
1.0
0.5
0.0
REFLECTANCE
0
1
2
3
4
5
FILTER LENGTH (cm)

Several experimental observations should be mentioned here. Firstly, filters of low writing power (long L_{cutoff}) have a more unstable reflectance than filters of higher writing power (short L_{cutoff}). Secondly, the relative reflectance, which is defined as the fraction of light reflected from the input end relative to the incident power, is consistently smaller after the writing process. Two typical examples are shown in Table 3.3. Thirdly, immediately after each cut, the reflectance always becomes unstable for a while before it finally settles down. The explanation for these observations are given in the next section.

3.3.3 Discussion

The most crucial point in this experiment is to ensure that the initial alignment is not perturbed in any manner during the cutting process. The reason for this is that if the coupling efficiency (η_{coup}) is changed during the cutting process, the measured reflectance will be changed accordingly. When the filters were reduced to length of only 10 cm, there were a few occasions when cutting it introduced sufficient jerking movement to misalign the system. Subsequent realignment is tedious because the exact initial η_{coup} can be very hard to recover. To ensure that the new η_{coup} is as close as possible to the initial one, realignment of the system was done repeatedly until the absolute maximum reflectance was obtained.

Detuning of the filter resonant wavelength (λ_c) was demonstrated by the experimental observations mentioned in the last section. Immediately after each cut, because of the contact between the scissors

TABLE 3.3

Relative reflectance during and after the writing process for two typical cases.

Writing Power (mW)	Relative Reflectance during the writing process (%)	Relative Reflectance after the writing process (%)
100	90	80
140	80	65

and the filter, there would be a slight temperature change and mechanical stretching. Consequently, λ_c was detuned momentarily and caused the reflectance to become unstable. Similarly, temperature difference between the time of writing and cutting filters detuned λ_c and caused the relative reflectance to be smaller after the writing process. Lastly, it seems likely that the longer the filter, the more it is susceptible to temperature variation and this explains why filters of low writing power (long L_{cutoff}) are less stable.

In view of the fact that the rate of ascent in R(L) is faster for higher writing power case, the accuracy of L_{cutoff} in this range is thus lower. This is illustrated in Table 3.2 where we see that the relative error in L_{cutoff} increases with the writing power. Therefore when the data on L_{cutoff} are used to predict the performance of filters, the reliability will be low for filters of high writing power and another experiment such as the one described below is needed to compensate for it.

3.4 MEASUREMENT OF THE SPECTRAL BANDWIDTH OF THE FILTERS

3.4.1 Experimental Setup and Procedures

Figure 3.8 shows the experimental setup for the measurement of the spectral bandwidth of the filters ($\Delta\lambda_t$). The source is a 50 Watt projection lamp whose filament is in the form of a helix of about 1/2 cm long and 1/5 cm wide. In order to couple light efficiently into the optical fibre filters, a 50X microscope objective mounted on a micropositioner was used. Filters which have not been cut in the last experiment were used because the experiment here requires a filter

FIGURE 3.8

Schematic of the apparatus for scanning the optical fibre filters. The source is a 50 Watt projection lamp. Both the microscope objective and input end V-groove magnetic mount (VGMM) are mounted on micropositioners. The output end VGMM is mounted on a piezoelectric micropositioner which is itself mounted on a 2 stages rotationer. The entrance and exit slit of the 1/2 m monochromator are set at 10 μ and the photomultiplier tube (PM tube) is running at 1 Kv with an effective impedance of 1 MΩ.

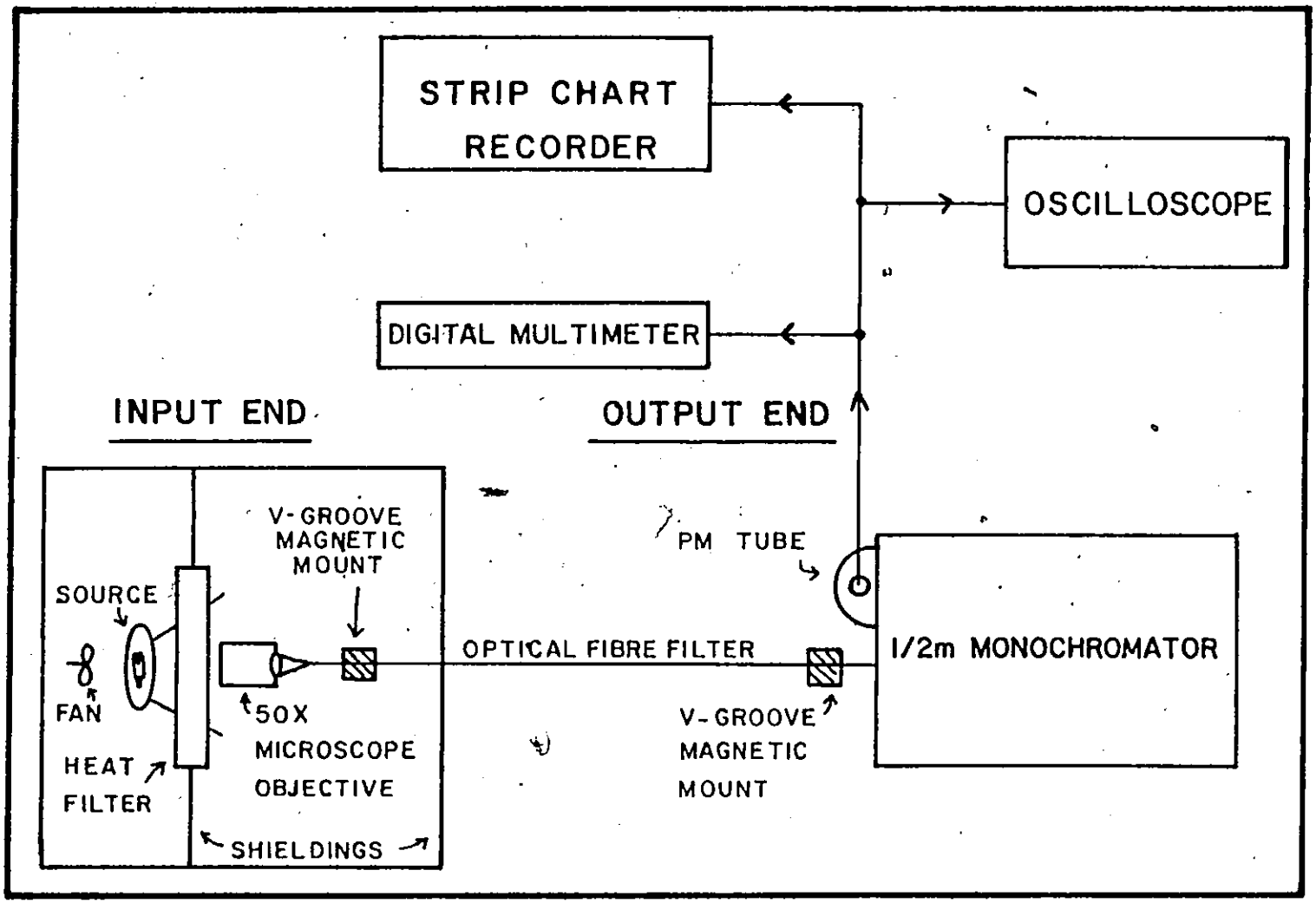
STRIP CHART RECORDER
OSCILLOSCOPE
DIGITAL MULTIMETER
INPUT END
OUTPUT END
V-GROOVE MAGNETIC MOUNT
PM TUBE
SOURCE
OPTICAL FIBRE FILTER
1/2m MONOCHROMATOR
FAN
50X MICROSCOPE OBJECTIVE
V-GROOVE MAGNETIC MOUNT
HEAT FILTER
SHIELDINGS

length of at least 1/3 meter long for manoeuvring. The input end of the filter was held in place by a V-groove magnetic mount which was mounted on another micropositioner. Knowing that the filter is prone to deterioration and detuning through heating, a fan was used to cool the source as it would otherwise become very hot. A heat reflecting mirror was also used between the source and the microscope objective.

The output end of the filter was held in place by a V-groove magnetic mount, which was attached to a piezoelectric micropositioner which was itself mounted on a 2 stages rotationer*. The resolution of the PZM is 40 Å/volt and that of the rotationer is 10 arc seconds. Such precision equipments were necessary to obtain a good coupling efficiency between the output end of the filter and the monochromater whose entrance slit was set at 10 μ so as to provide good resolution. Recalling that the core diameter of the fibre is only 2.2 μ, precise and delicate positioning is a necessity. The rest of the filter between the input and output ends was allowed to hang loose without any stretching in order to avoid detuning.

The exit slit of the monochromator was also set at 10 μ and the signal was detected by a S-20 photomultiplier tube that has an effective impedance of roughly 1 MΩ. The signal detected was displayed on the digital multimeter for direct read out, on the oscilloscope for the

---

* The 2 stages rotationer was used to compensate for any tilting of the filter which may result in reducing the light that hits the grating in the monochromator.

observation of the noise and signal fluctuation and on the strip chart recorder for permanent record.

Finally, in order to avoid any direct light path from the source to the monochromator, a shielding was provided for the input end of the filter. To avoid any mechanical vibration in the filter due to the blowing fan, further shielding was provided.

Having set up the experiment described above, the experimental procedure was as follows. The source was driven at 4 Watts and the filter was mounted at the input end on the V-groove magnetic mount. To align this end efficiently, the output end of the filter was brought to face a photodetector of large area compared to the fibre. The reason for such a procedure was to separate the alignment into 2 steps; input and output ends.

After proper alignment of the input end, the output end of the filter was very carefully transferred to the PZM's V-groove magnetic mount without disturbing the input end in any manner. The power to the source was increased to 50 Watts in order to compensate for the loss in the coupling between the filter and the monochromator and manual adjustment of the PZM was applied to achieve maximum signal as displayed on the digital multimeter. The 2 stages rotationer and the power supply to the PZM were then employed to further maximize the signal and typical improvement of a factor of 2 is possible.

When both the input and the output ends of the filter are aligned, the scanning of the filter can proceed by scanning the monochromator wavelength. A 2.2 μf capacitor was shunted across the input of the

strip chart recorder for reducing the noise fluctuation. Typical operation conditions are listed in Table 3.4.

3.4.2 Results

Figure 3.9 shows a curve of the observed transmittance as a function of wavelength for an optical fibre filter of 140 mW writing power. In order to facilitate subsequent analysis, it is transformed into a reflectance curve $R(\lambda)$ and shown in Fig. 3.10 where the relative dip (R.D.) is defined as the magnitude of the dip divided by the peak signal shown in Fig. 3.9. It was observed in this experiment that as the writing power increases, both the magnitude of the relative dip and the observed full width half maximum ($\Delta\lambda_{FWHM}$) increases. Furthermore, the variation of $\Delta\lambda_{FWHM}$ and R.D. is smaller for filters of higher writing power which means the accuracy of these data is better.

This experiment is a difficult one as is evidenced by the fact that the signal to noise ratio (SNR) rarely exceeded 3.0 and the reasons for this are as follows. First of all, the source filament is much too large to be properly focussed onto the core of the fibre. Even if this can be done, the fact that the numerical aperture of the fibre is merely 0.22 implies that much of the light will be radiated away from the core. Secondly, comparing the effective numerical aperture of the monochromator which is 0.058 to that of the fibre, there is at least a loss factor of 14 in the coupling of light from the fibre to the monochromator. Proper f# matching was attempted but placed impossibly stringent requirements on the alignment due to the extremely small

TABLE 3.4

Typical operation conditions for the scanning of optical fibre filters.

Description	Condition
Voltage applied to photomultiplier tube	1 kV
Power supplied to the source	50 Watt
Monochromator scanning rate	2Å/min
Stripchart recorder speed	30 cm/min
Stripchart recorder full scale	5 mv

FIGURE 3.9

Spectral transmittance curve of an optical fibre filter of 140 mW writing power as observed in the experiment. $\lambda-\lambda_c$ is the deviation of the wavelength (λ) from the wavelength of minimum transmittance λ_c, the resonant wavelength of the filter.

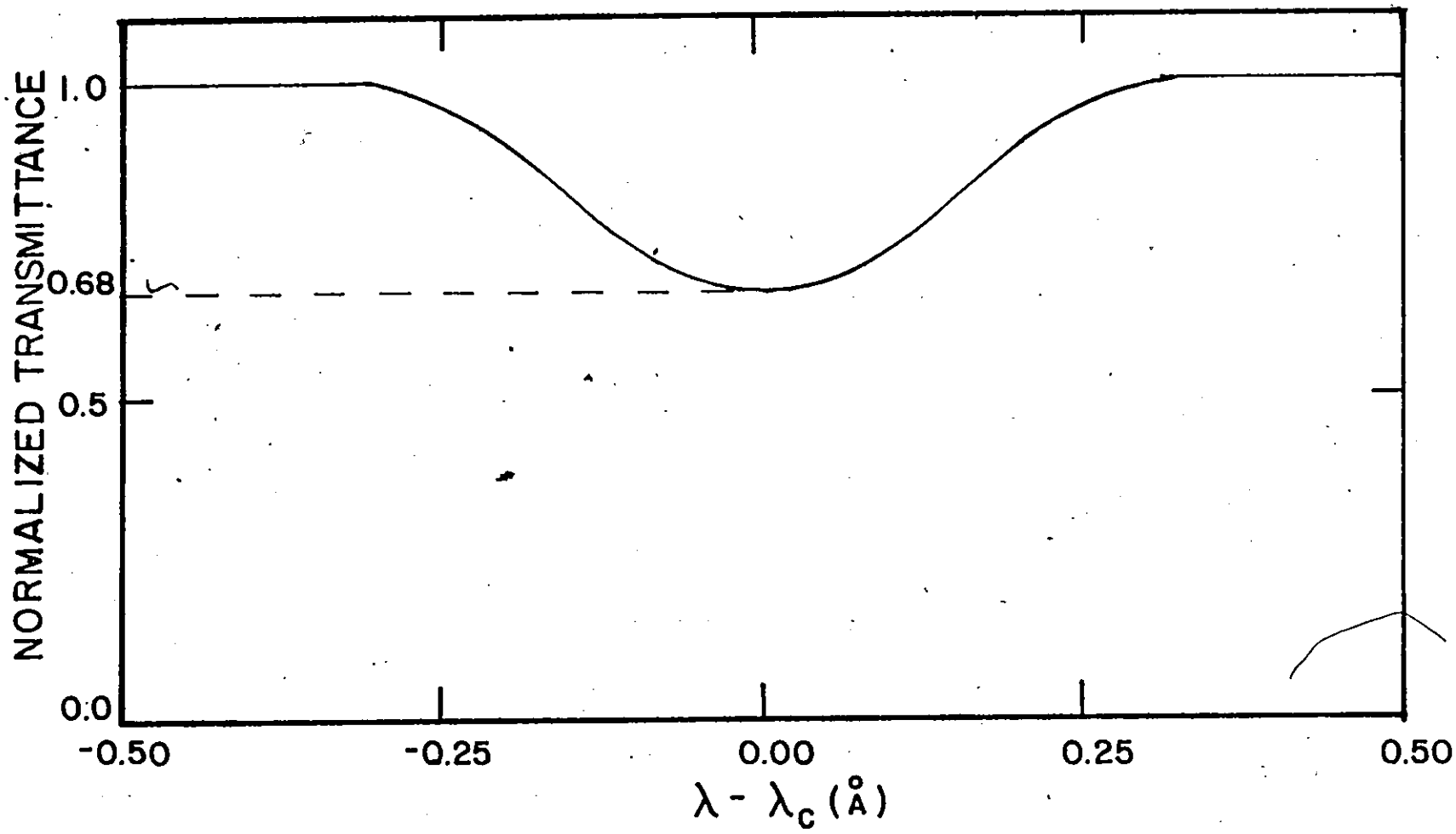
NORMALIZED TRANSMITTANCE
1.0
0.68
0.5
0.0
-0.50
-0.25
0.00
0.25
0.50
λ - λc (Å)

FIGURE 3.10

Spectral reflectance curve of an optical fibre filter of 140 mW writing power as observed in the experiment. $\lambda - \lambda_c$ is the deviation of the wavelength λ from the wavelength of maximum reflectance λ_c, resonant wavelength of the filter. The full width half maximum $\Delta\lambda_{FWHM}$ of the spectral reflectance curve shown is 0.32 Å.

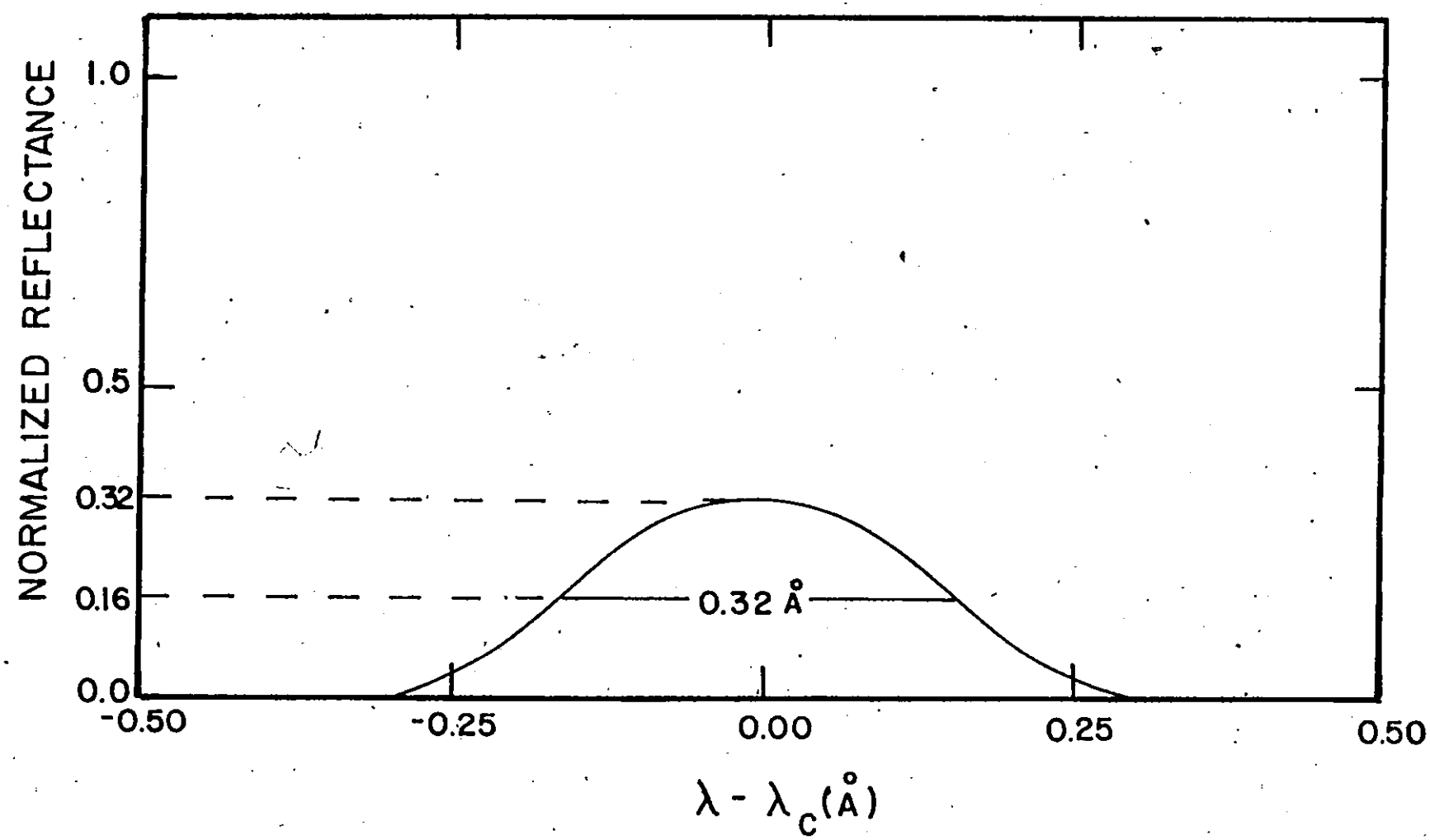
NORMALIZED REFLECTANCE
1.0
0.5
0.32
0.16
0.0
0.32 Å
-0.50
-0.25
0.00
0.25
0.50
λ - λc(Å)

fibre core. Thirdly, the source itself was found to be noisy and fluctuations presented in its light output were quite frequent. Nevertheless, using a sufficient number of scans for the higher writing power cases permitted reasonable data to be collected.

3.4.3 Discussion

It is important to mention here that the observed full width half maximum ($\Delta\lambda_{FWHM}$) in $R(\lambda)$ is by no means the true spectral bandwidth of the filters ($\Delta\lambda_t$). This is because the experimental setup or the system itself has a finite spectral bandwidth ($\Delta\lambda_r$). Therefore, what was observed is actually a convolution of the filter spectral curve ($R_t(\lambda)$) and the system response curve ($f(\lambda)$). In order to extract $\Delta\lambda_t$ from the observed $R(\lambda)$, it is therefore necessary to find $f(\lambda)$ or in other words, calibrate the system.

The experimental set up for determining $f(\lambda)$ is identical to the original set up shown in Fig. 3.8 except the source and the filter were replaced by an Argon laser and a single mode fibre respectively. The Argon laser was set to lase at the green line and its power level was adjusted to give the same signal level as in the scanning of filters. By doing so, all the scanning conditions shown in Table 3.2 are preserved and a reliable $f(\lambda)$ was obtained. In the next chapter, we will discuss how to extract $\Delta\lambda_t$ from $R(\lambda)$ with the knowledge of $f(\lambda)$.

From the property of convolution between any two functions, for a fixed $\Delta\lambda_r$, $\Delta\lambda_t$ is proportional to $\Delta\lambda_{FWHM}$. Therefore, the observation of increasing $\Delta\lambda_{FWHM}$ with respect to the writing power is equivalent to saying that $\Delta\lambda_t$ increases with the writing power and this is predicted

by the theory. Also, for fixed $\Delta\lambda_r$ again, the observed relative dip is proportional to the maximum reflectance in a filter. The observation of increasing relative dip with respect to the writing power is therefore equivalent to increasing maximum reflectance with respect to the writing power. This agrees with what we observed during the writing process of the filters.

Finally, from the fact that noise is independent of the writing power, the signal to noise ratio (SNR) with respect to the writing power is thereby a function of the signal only. For filters of low writing power, it was observed in the experiment that their maximum relative dip or their signal is low. Therefore, it will be unreliable to use them to predict the performance of filters. On the other hand, for filters of high writing power, their signal is large and therefore their reliability is better. In conclusion then, the experiment described here is reliable for filters of high writing power. Combining this experiment with the previous experiment on the determination of L_{cutoff}, which is reliable for filters of low writing power, we therefore have reliable data for filters of high and low writing power.

CHAPTER 4

ANALYSIS OF EXPERIMENTAL DATA

4.1 INTRODUCTION

In the experimental work described in the last chapter, two independent sets of data - R(L) and R(λ) - for the optical fibre filters were obtained. In this chapter, these two sets of data and the theory will be used to determine the basic parameters controlling the performance of the filters. Furthermore, comparison of the two sets of data in the region where both experiments have reasonable accuracy serves to confirm the reliability of the data analysis. Finally, the conjunction of the two sets of data permits conclusions to be drawn concerning the size of the induced refractive index for the available writing powers and indicates that, within experimental error, this induced index perturbation increases in proportion to the square of the writing power.

In sections 2 and 3 of this Chapter, the data on R(L) and R(λ) are analyzed respectively. Section 4 presents the comparison between the results obtained from the two sets of data and section 5 discusses the practical and potential implications of these results for the photo-induced refractive index change in optical fibres.

4.2 ANALYSIS OF R(L)

In Chapter 2, it was shown that a major control parameter in the

theory is the induced index perturbation $\Delta\varepsilon$. Variation of this parameter induces corresponding changes in R(L) and R(χ) or equivalently, values of $\Delta\lambda_t$ and L_{cutoff}. This feature in the theory makes it possible to produce a best fit between the experimental R(L) and the theoretical prediction for R(L), using $\Delta\varepsilon$ as a parameter. Figures 4.1-4.5 show the results obtained with this procedure for the different writing powers used in the experiment.

In each figure, the theoretical variation of R(L) is shown for values of $\Delta\varepsilon$ corresponding to $\Delta\varepsilon_f$ and $\Delta\varepsilon_f \pm 0.5 \times 10^{-5}$, where $\Delta\varepsilon_f$ gives the best fit. This serves to demonstrate that, as the writing power increases, the theoretical variation of R(L) for $\Delta\varepsilon_f$ and $\Delta\varepsilon_f \pm 0.5 \times 10^{-6}$ becomes closer together; signifying that the accuracy of the determination of $\Delta\varepsilon$ from the experimental R(L) variation is reduced. An alternative way of demonstrating this is to plot the experimentally obtained values for $L_{cutoff} \pm \Delta L$, where ΔL is the tolerance or error, on the theoretical curve of L_{cutoff} versus $\Delta\varepsilon$ (Fig. 2.10) and deduce from it the corresponding range of $\Delta\varepsilon$. This is shown in Fig. 4.6 and it clearly indicates that for higher writing powers, the range of $\Delta\varepsilon$ that corresponds to $L_{cutoff} \pm \Delta L$ is larger which causes less accuracy in the determination of $\Delta\varepsilon$. Table 4.1 summarizes the range of $\Delta\varepsilon$ corresponding to the different ranges of L_{cutoff}.

The results shown in Figs. 4.1-4.5 can be used to obtain the variation of $\Delta\varepsilon$ versus the writing power and the latter is shown in Fig. 4.7. Referring to this figure, it is quite clear that for WP $\geq$ 100 mW, the experimental technique of determining L_{cutoff} and subsequently $\Delta\varepsilon$ is

FIGURE 4.1

Theoretical predictions of R(L) versus experimental R(L) for a writing power of 35 mW. The X's denote the experimental data.

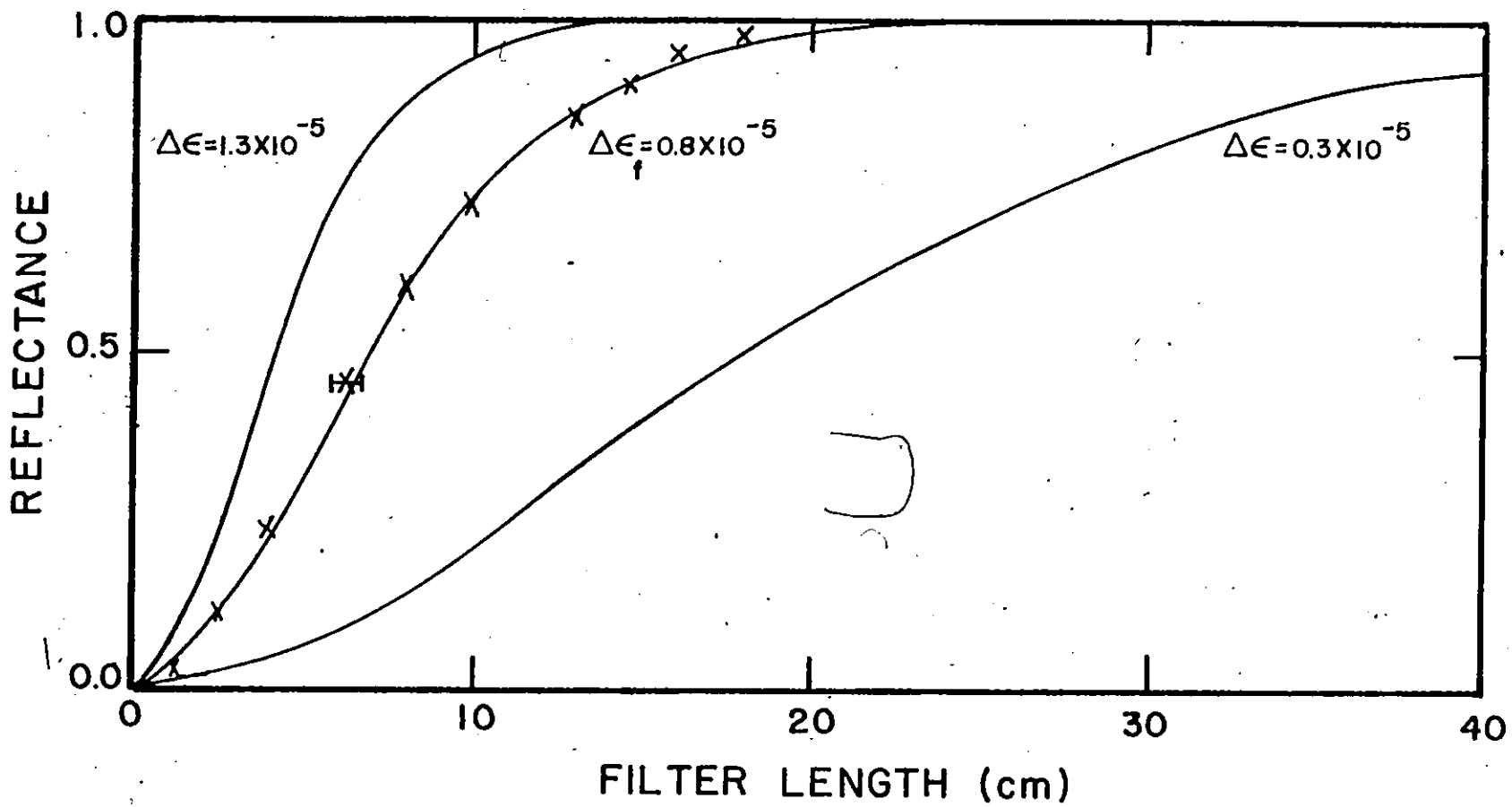
1.0
0.5
0.0
REFLECTANCE
0
10
20
30
40
FILTER LENGTH (cm)
$\Delta\epsilon = 1.3 \times 10^{-5}$
$\Delta\epsilon_f = 0.8 \times 10^{-5}$
$\Delta\epsilon = 0.3 \times 10^{-5}$

FIGURE 4.2

Theoretical prediction of R(L) versus experimental R(L) for a writing power of 50 mW. The X's denote the experimental data.

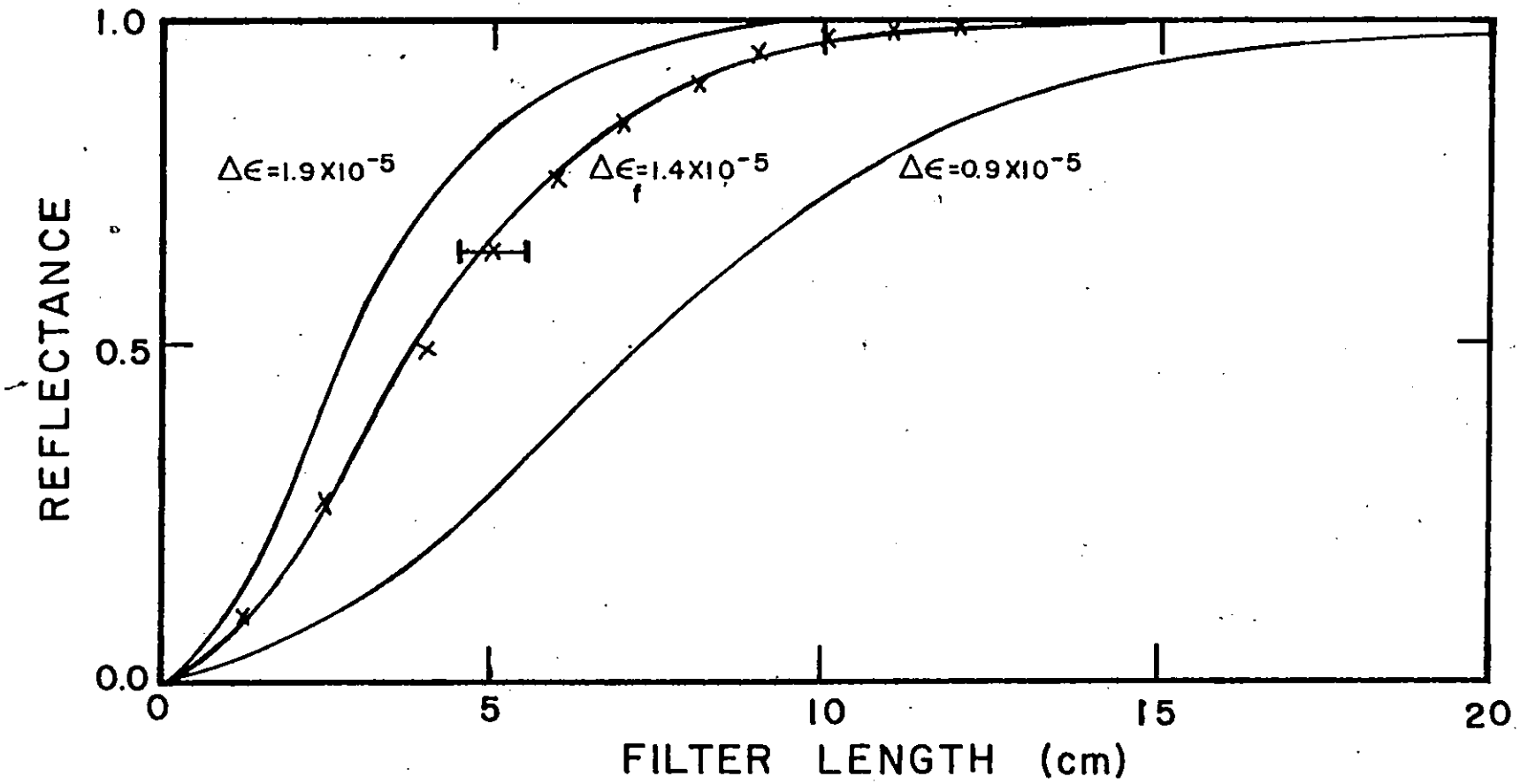
1.0
0.5
0.0
REFLECTANCE
0
5
10
15
20
FILTER LENGTH (cm)
ΔE=1.9X10^-5
ΔE_f=1.4X10^-5
ΔE=0.9X10^-5

FIGURE 4.3

Theoretical prediction of R(L) versus experimental R(L) for a writing power of 70 mW. The X's denote the experimental data.

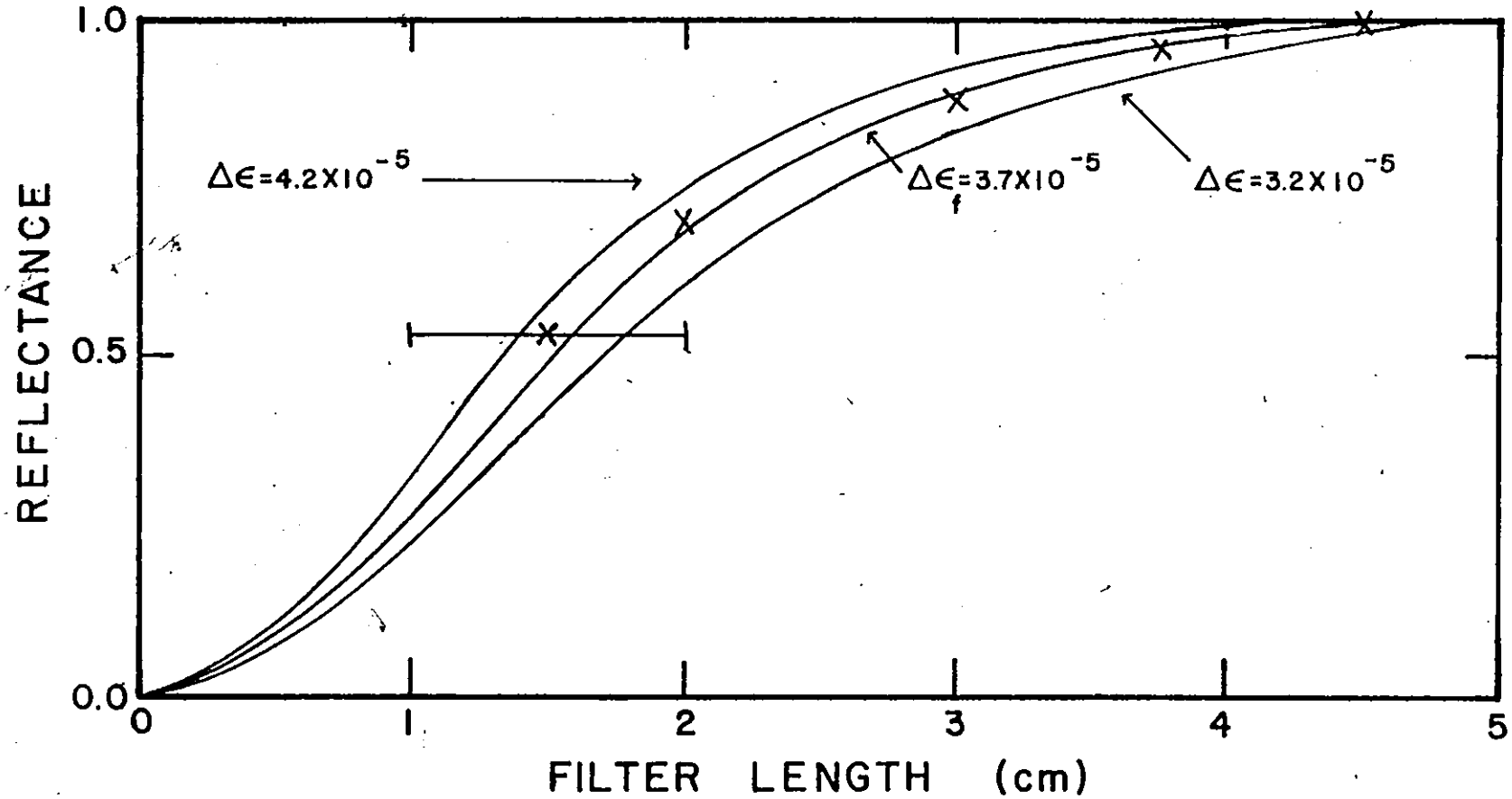
1.0
0.5
0.0
REFLECTANCE
0
1
2
3
4
5
FILTER LENGTH (cm)
ΔE=4.2X10^-5
ΔE_f=3.7X10^-5
ΔE=3.2X10^-5

FIGURE 4.4

Theoretical prediction of R(L) versus experimental R(L) for a writing power of 85 mW. The X's denote the experimental data.

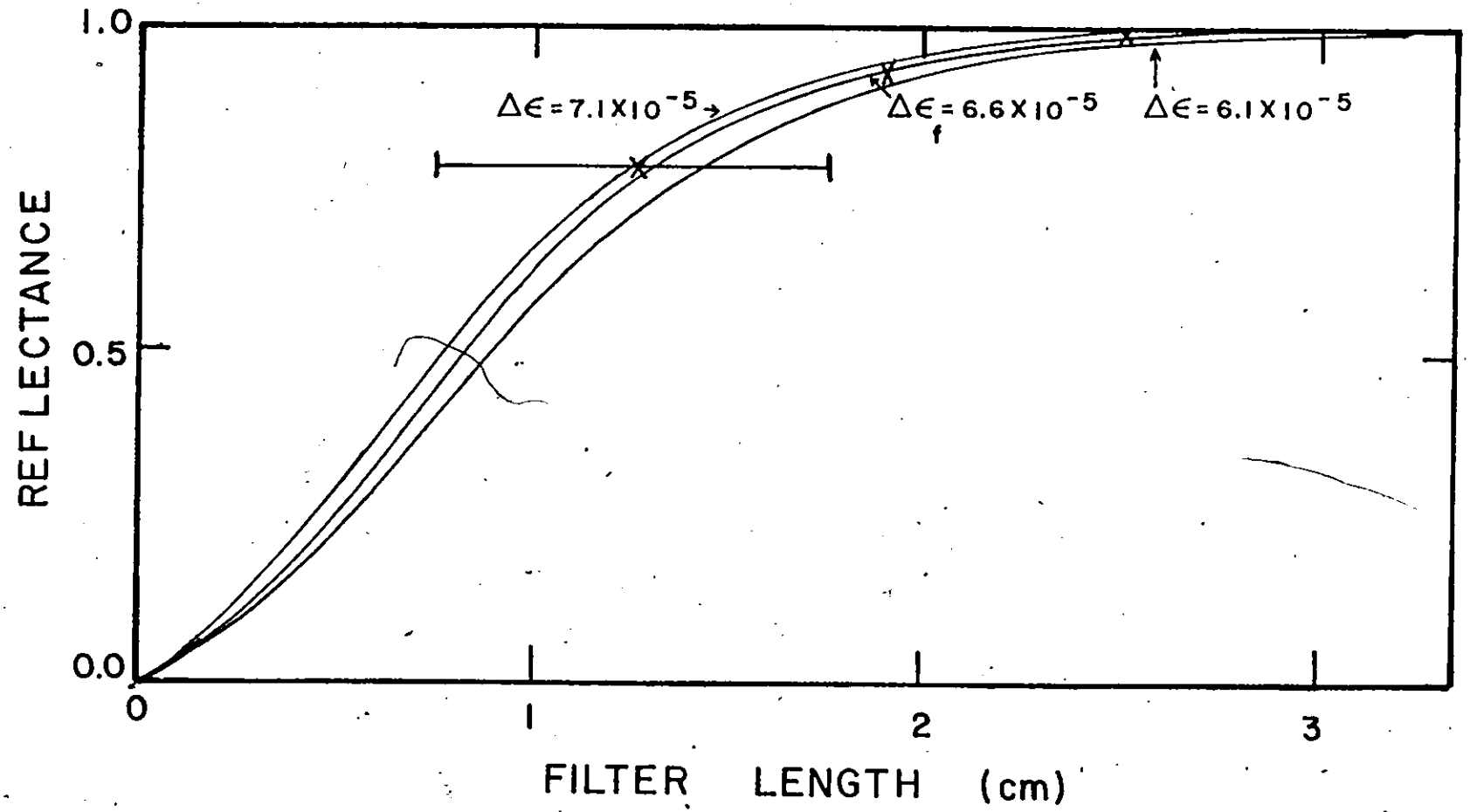
1.0
0.5
0.0
REFLECTANCE
0
1
2
3
FILTER LENGTH (cm)
$\Delta\epsilon = 7.1 \times 10^{-5}$
$\Delta\epsilon_f = 6.6 \times 10^{-5}$
$\Delta\epsilon = 6.1 \times 10^{-5}$

FIGURE 4.5

Theoretical prediction of R(L) versus experimental R(L) for a writing power of 100 mW. The X's denote the experimental data.

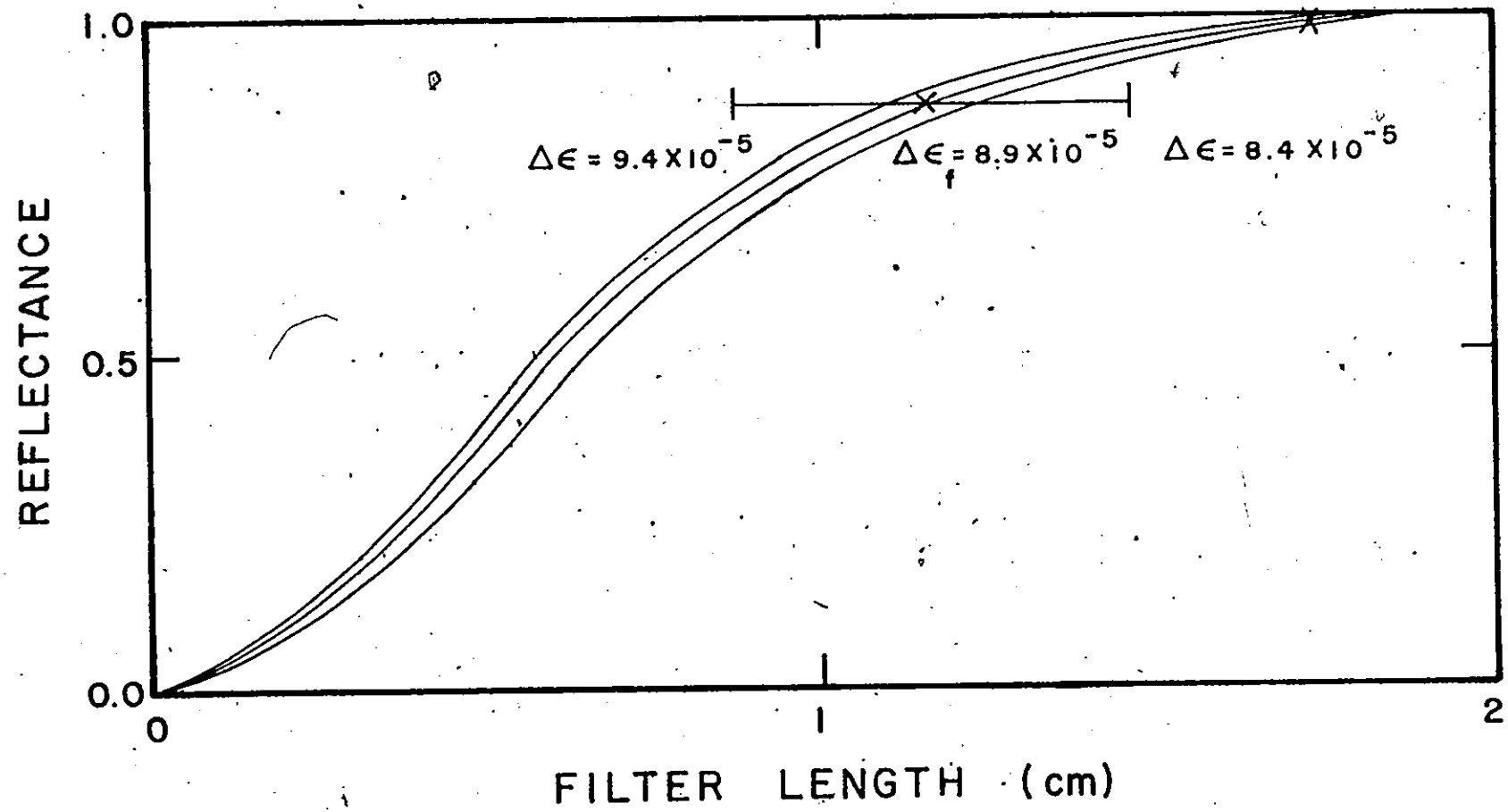
1.0
0.5
0.0
REFLECTANCE
0
1
2
FILTER LENGTH (cm)
$\Delta\epsilon = 9.4 \times 10^{-5}$
$\Delta\epsilon_f = 8.9 \times 10^{-5}$
$\Delta\epsilon = 8.4 \times 10^{-5}$

FIGURE 4.6

Ranges of $\Delta\varepsilon$ corresponding to ranges of experimentally measured L_{cutoff} for the different writing powers.

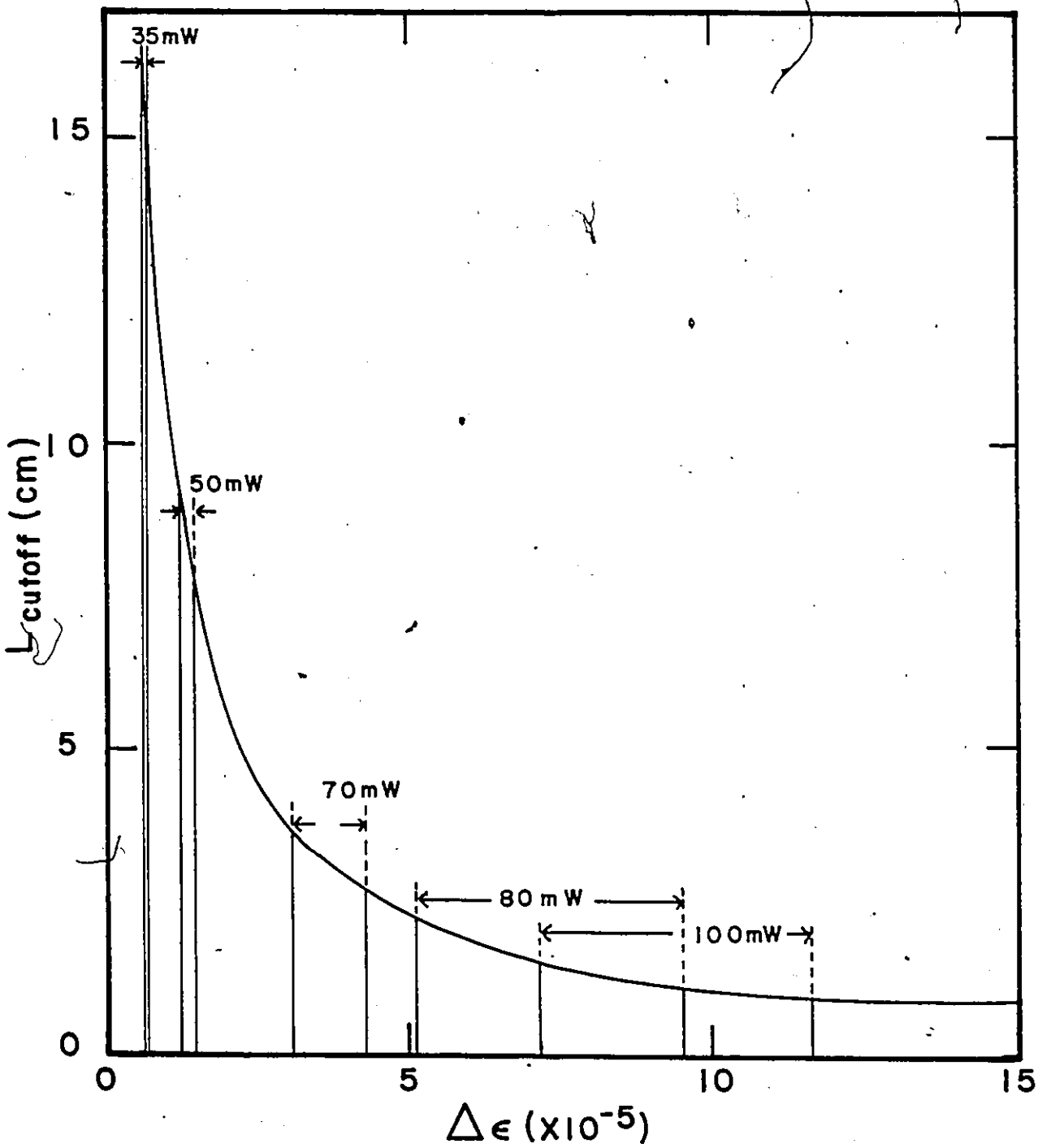
35mW
50mW
70mW
80 mW
100mW
15
10
5
0
0
5
10
15
L_{cutoff} (cm)
$\Delta\epsilon$ ($\times 10^{-5}$)

TABLE 4.1

Ranges of induced index perturbation ($\Delta\varepsilon$) corresponding to ranges of experimentally measured effective cutoff length of the filters (L_{cutoff}) for different levels of writing power.

Writing Power (mW)	Range of L_{cutoff} (cm)	Range of $\Delta\varepsilon$ ($\times 10^{-5}$)
35	15.5-16.5	0.77-0.81
50	7.7-8.7	1.3-1.5
70	2.6-3.6	3.2-4.4
85	1.2-2.2	5.1-9.5
100	0.97-1.57	7.2-11.65

FIGURE 4.7

Induced index perturbation $\Delta\varepsilon$ as a function of the writing power as determined from the experimental data on R(L) or L_{cutoff}.

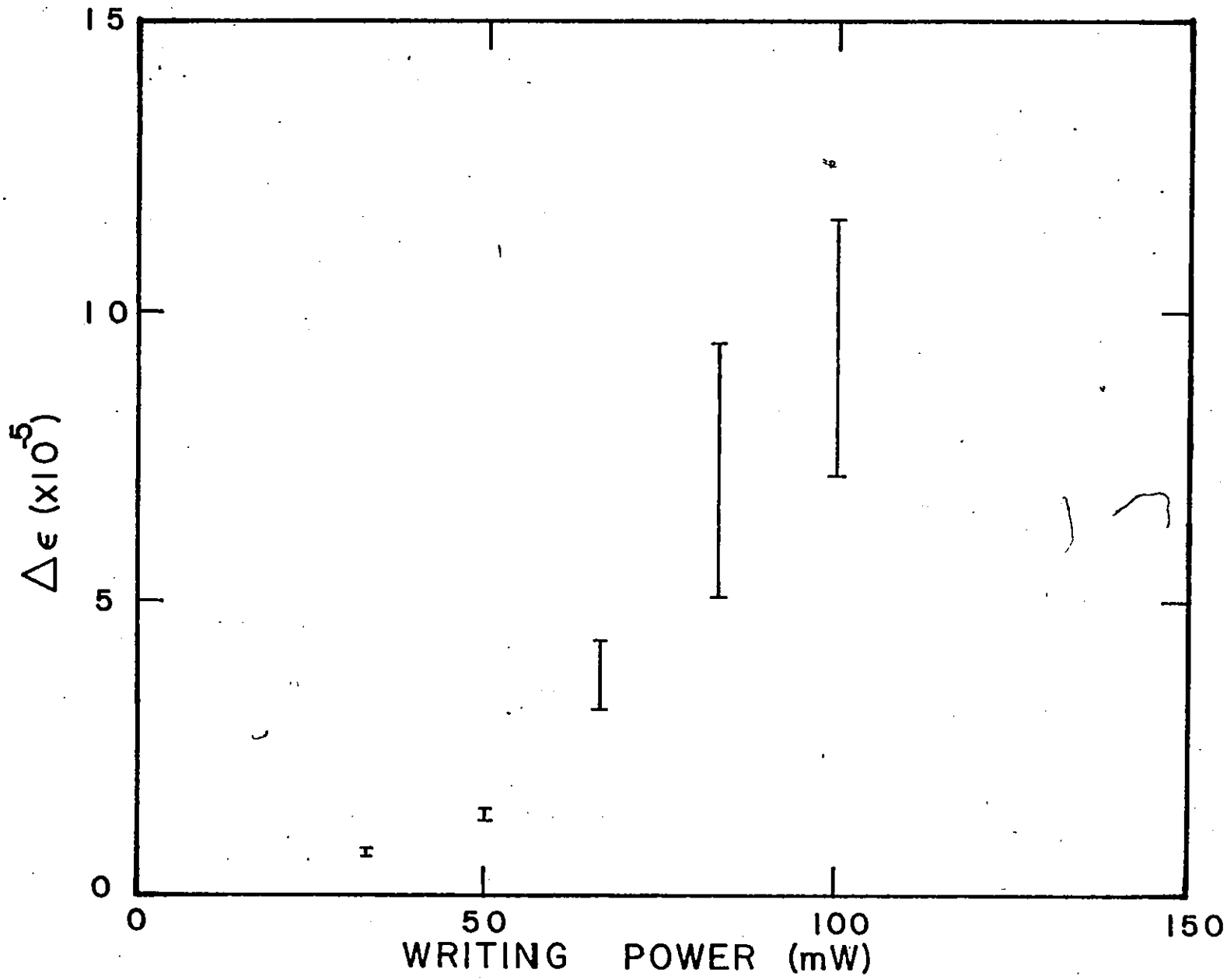
15
10
5
0
$\Delta\epsilon$ ($\times 10^{-5}$)
0
50
100
150
WRITING POWER (mW)

of limited use. Accordingly, an alternate experiment such as the determination of $R(\lambda)$ is required and we now proceed to analyze the data obtained using that approach.

4.3 ANALYSIS OF $R(\lambda)$

The first step in analyzing the measured spectral reflectance curve $R(\lambda)$ is to deconvolute it from the system response function $f(\lambda)$. By doing so, the true spectral reflectance curve $R_t(\lambda)$ is obtained and its comparison with the theory can then be made.

The procedure for deconvoluting the filter spectral reflectance ($R_t(\lambda)$) from the observed $R(\lambda)$ is as follows. Since the physical length of the filter is generally much greater than the effective cutoff length, Eqs. (2.67) and (2.68) can be used and $R_t(\lambda)$ should resemble the curve $R'(\lambda)$ shown in Fig. 2.3. The full width half maximum of this curve ($\Delta\lambda_t$) is the unknown quantity whereas the full width half maximum ($\Delta\lambda_{FWHM}$) and relative dip (R.D.) of the measured $R(\lambda)$ are the known quantities. A suitable value of $\Delta\lambda_t$ is assumed for $R'(\lambda)$ and the latter is convoluted with $f(\lambda)$ to give the convoluted curve $C(\lambda)$. The value of R.D. and $\Delta\lambda_{FWHM}$ of this curve is then compared with that of $R(\lambda)$. If they agree to within the errors involved in the experiment, then $\Delta\lambda_t$ is found. On the other hand, if they disagree by more than the experimental errors, a new value of $\Delta\lambda_t$ is assumed for $R'(\lambda)$ and the convolution process is repeated. In essence, it is an iteration process in which a value of $\Delta\lambda_t$ in $R'(\lambda)$ is assumed and subsequently used in convoluting $R'(\lambda)$ with $f(\lambda)$ to give $C(\lambda)$ until the latter agrees with $R(\lambda)$ to within the experimental errors.

Applying this deconvolution process to the five sets of experimental $R(\lambda)$ corresponding to filters of different writing power, the true spectral reflectance curves $R_t(\lambda)$ are obtained as shown in Fig. 4.8. As in the cases of R(L), the curves represent the averaged $R_t(\lambda)$ corresponding to the averaged $\Delta\lambda_{FWHM}$ and R.D. The ranges of $\Delta\lambda_t$ corresponding to the ranges of observed $\Delta\lambda_{FWHM}$ and R.D. for different levels of writing power are summarized in Table 4.2.

Once values of $\Delta\lambda_t$ have been found, comparison can be made with the theoretical values and their corresponding induced index perturbation $\Delta\varepsilon$ determined as are summarized in Table 4.3. As before, we can now extract the relationship between $\Delta\varepsilon$ and WP as shown in Fig. 4.9. Whereas the accuracy of the previous experiment (R(L)) decreases as a function of power, the converse is true here as indicated by the figure. The reason for this is that (1) the R.D. is higher for higher WP and consequently the signal to noise ratio is better and (2) the accuracy of the deconvolution process decreases for smaller $\Delta\lambda_t$. For WP > 85 mW, the experiment described here provides reasonably reliable data.

4.4 COMPARISON BETWEEN THE ANALYSIS OF R(L) AND R(λ)

It was demonstrated in the previous two sections that the accuracy of the two experimental techniques for determining $\Delta\varepsilon$ is dependent on the writing power (WP). In the low WP region (< 100 mW) values deduced from data on L_{cutoff} are reliable whereas in the high WP region (> 85 mW), results from $\Delta\lambda_t$ are more reliable. In the moderate WP region of 85-100 mW then, the two experiments both produce moderately

FIGURE 4.8

True spectral reflectance curves ($R_t(\lambda)$) of the optical fibre filters for different writing powers. Curves A, B, C, D and E correspond to writing powers of 140 mW, 130 mW, 100 mW, 85 mW and 70 mW respectively, and have spectral bandwidths of 0.264 Å, 0.232 Å, 0.184 Å, 0.164 Å and 0.132 Å respectively. The peak of $R_t(\lambda)$ for different writing powers has been normalized to 1.0 in this figure for the sake of comparison.

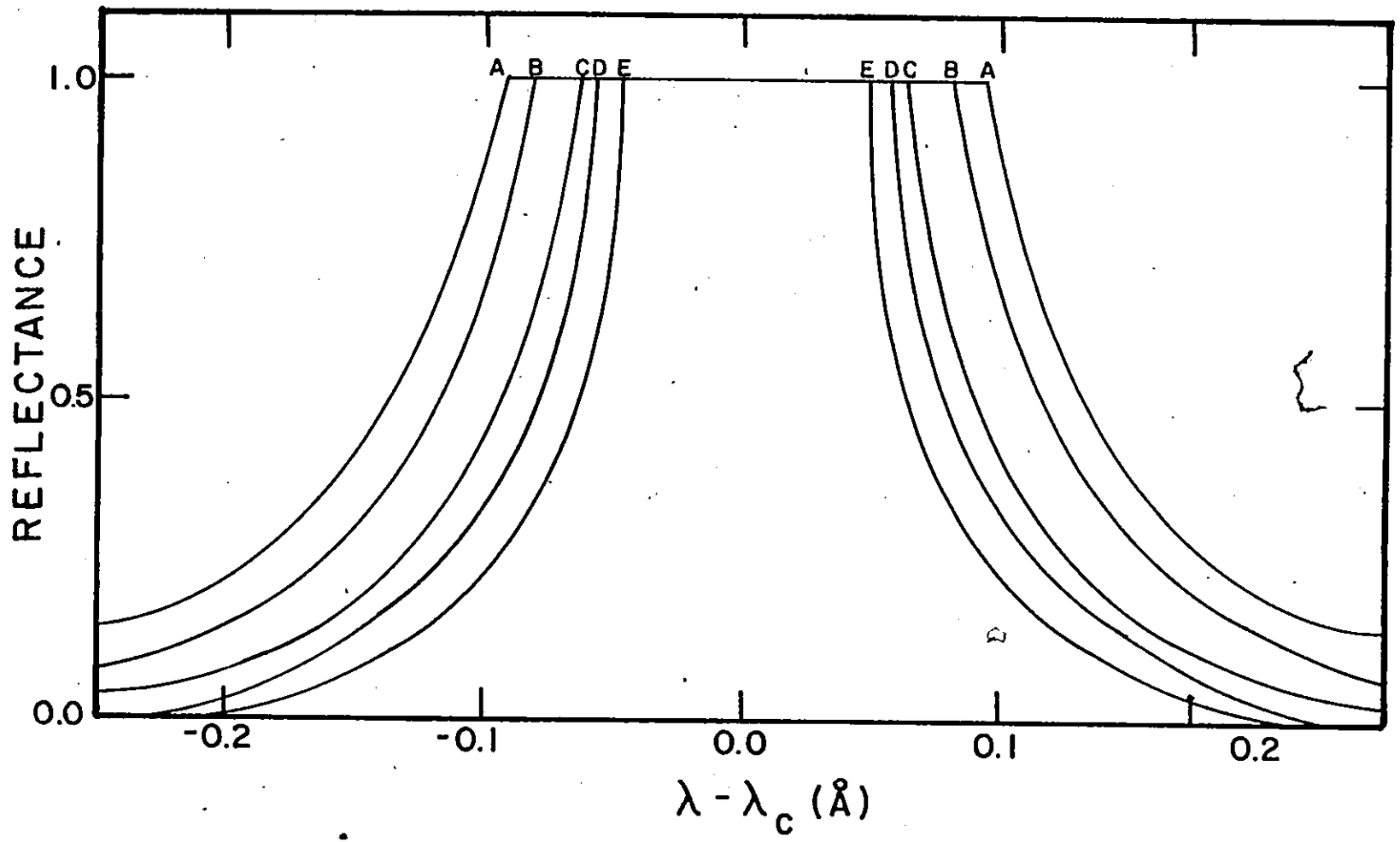
A B C D E
E D C B A
1.0
0.5
0.0
REFLECTANCE
-0.2
-0.1
0.0
0.1
0.2
λ - λc (Å)

TABLE 4.2

Spectral Bandwidth of the filters ($\Delta\lambda_t$) by deconvoluting the observed spectral reflectance curve $R(\lambda)$ from the system response function $f(\lambda)$ as a function of the writing power.

Writing Power (mW)	$\Delta\lambda_t$ (Å)
70	0.096 - 0.18
85	0.13 - 0.21
100	0.149 - 0.24
130	0.22 - 0.28
140	0.26 - 0.3

TABLE 4.3

Ranges of induced index perturbation ($\Delta\varepsilon$) corresponding to ranges of experimentally measured spectral bandwidth of the filters ($\Delta\lambda_t$) for different levels of writing power.

Writing Power (mW)	$\Delta\varepsilon$ (x 10^{-5})
70	7 - 13.4
85	9.6 - 15.5
100	11 - 17.3
130	16 - 20.2
140	19.2 - 21.8

FIGURE 4.9

Induced index perturbation $\Delta\varepsilon$ as a function of the writing power as determined from the experimental data on $R(\lambda)$ or $\Delta\lambda_{FWHM}$.

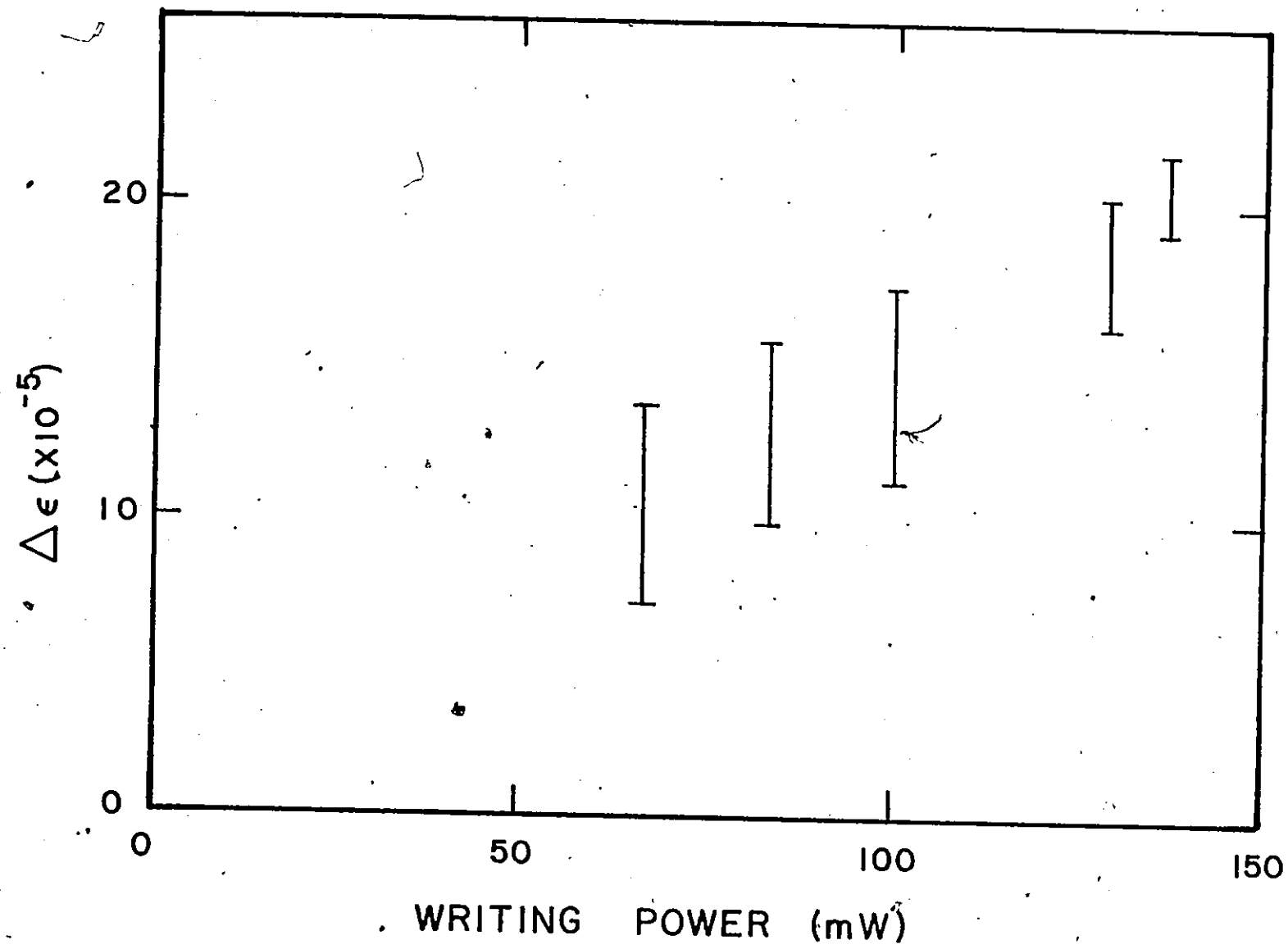
20
10
0
$\Delta\epsilon\ (\times 10^{-5})$
0
50
100
150
WRITING POWER (mW)

reliable results. In Fig. 4.10, both experimental methods are used to plot the curve of $\Delta\varepsilon$ versus WP and it shows that in the WP region of 85-100 mW, the error bars for the two experiments overlap. This therefore serves to indicate that indeed the two experiments are in agreement in the moderate WP region.

Discarding the unreliable data - low WP $\Delta\lambda_t$ data and high WP L_{cutoff} data - we have redrawn Fig. 4.10 in Fig. 4.11, showing $\Delta\varepsilon$ as a nonlinearly increasing function of WP with no sign of $\Delta\varepsilon$ saturating over the available range of writing power. Since it has been suggested that the writing process for optical fibre filters is possibly due to a two photon process [49-50] (which is dependent on the square of writing power), $\Delta\varepsilon$ is plotted against $(WP)^2$ in Fig. 4-12. This shows that a straight line can be fitted fairly well to the data and thus indicates that the induced index perturbation $\Delta\varepsilon$ in the GeO_2 doped SiO_2 optical fibre filter is a function of $(WP)^2$ for the range of WP used in the experiments here.

Finally, using both sets of data again (L_{cutoff} for low WP and $\Delta\lambda_t$ for high WP), $\Delta\lambda_t$ versus WP and $\Delta\beta_{pp}$ versus WP are plotted in Fig. 4.13 and 4.14 respectively so as to show the spectral bandwidth and anomalous dispersion for the filters made in our experiment. The figures show that a spectral bandwidth ranging from 0.01-0.3 Å and a peak to peak anomalous dispersion of $7 \times 10^{-4}/\mu$ are available for the writing powers employed in the experiments reported here.

FIGURE 4.10

Induced index perturbation $\Delta\varepsilon$ versus the writing power using both sets of experimental data. The I's denote points from data on I_{cutoff} whereas the $\mathbb{I}$'s denote points from data on $\Delta\lambda_t$.

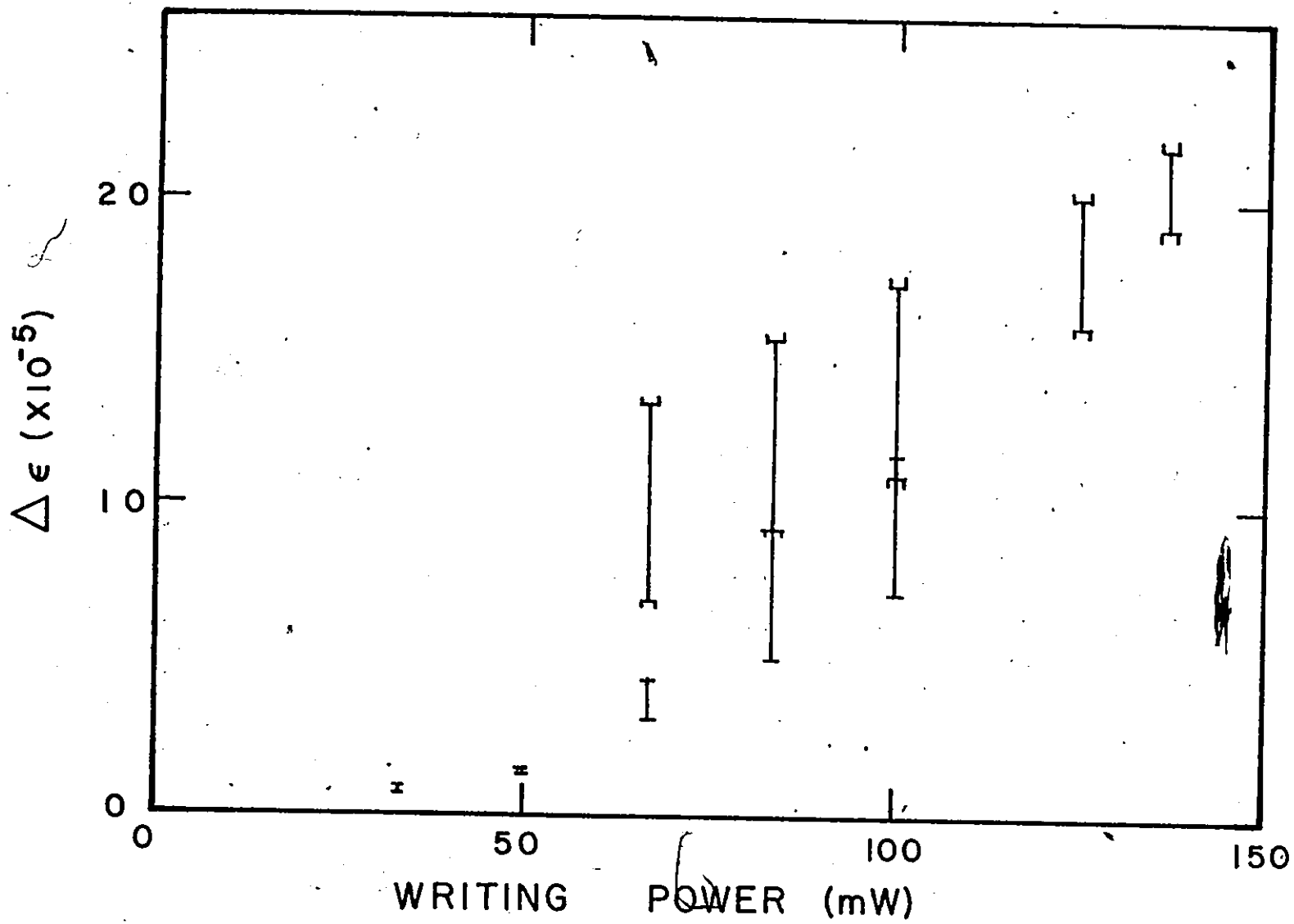
20
10
0
$\Delta\epsilon$ ($\times 10^{-5}$)
0
50
100
150
WRITING POWER (mW)

FIGURE 4.11

Induced index perturbation $\Delta\varepsilon$ versus the writing power using both sets of experimental data. The I's denote points from data on L_{cutoff} whereas the $\mathbb{I}$'s denote points from data on $\Delta\lambda_t$.

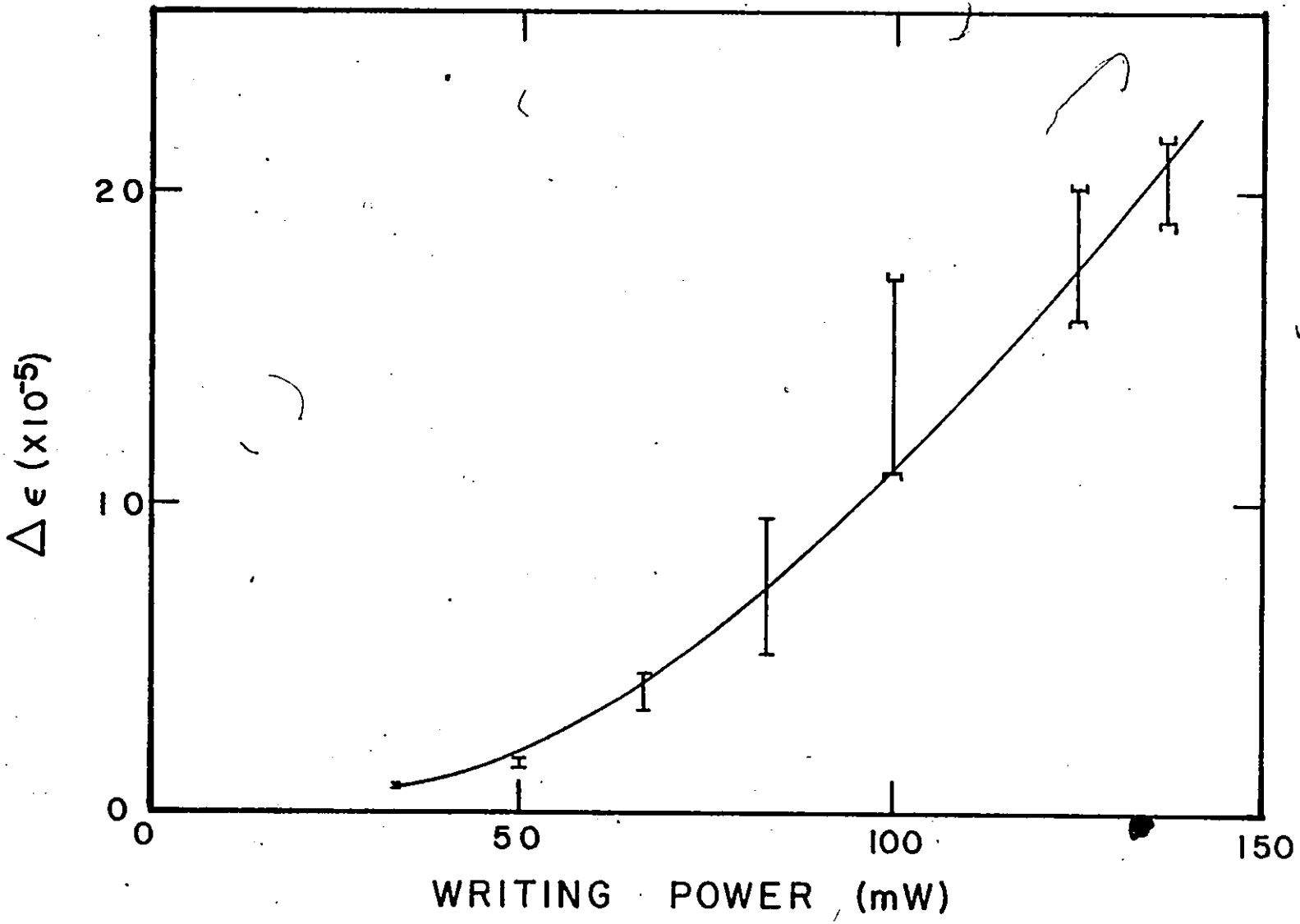
20
10
0
$\Delta\epsilon$ ($\times 10^{-5}$)
0
50
100
150
WRITING POWER (mW)

FIGURE 4.12

Induced index perturbation $\Delta\varepsilon$ versus the square of the writing power using both sets of experimental data.

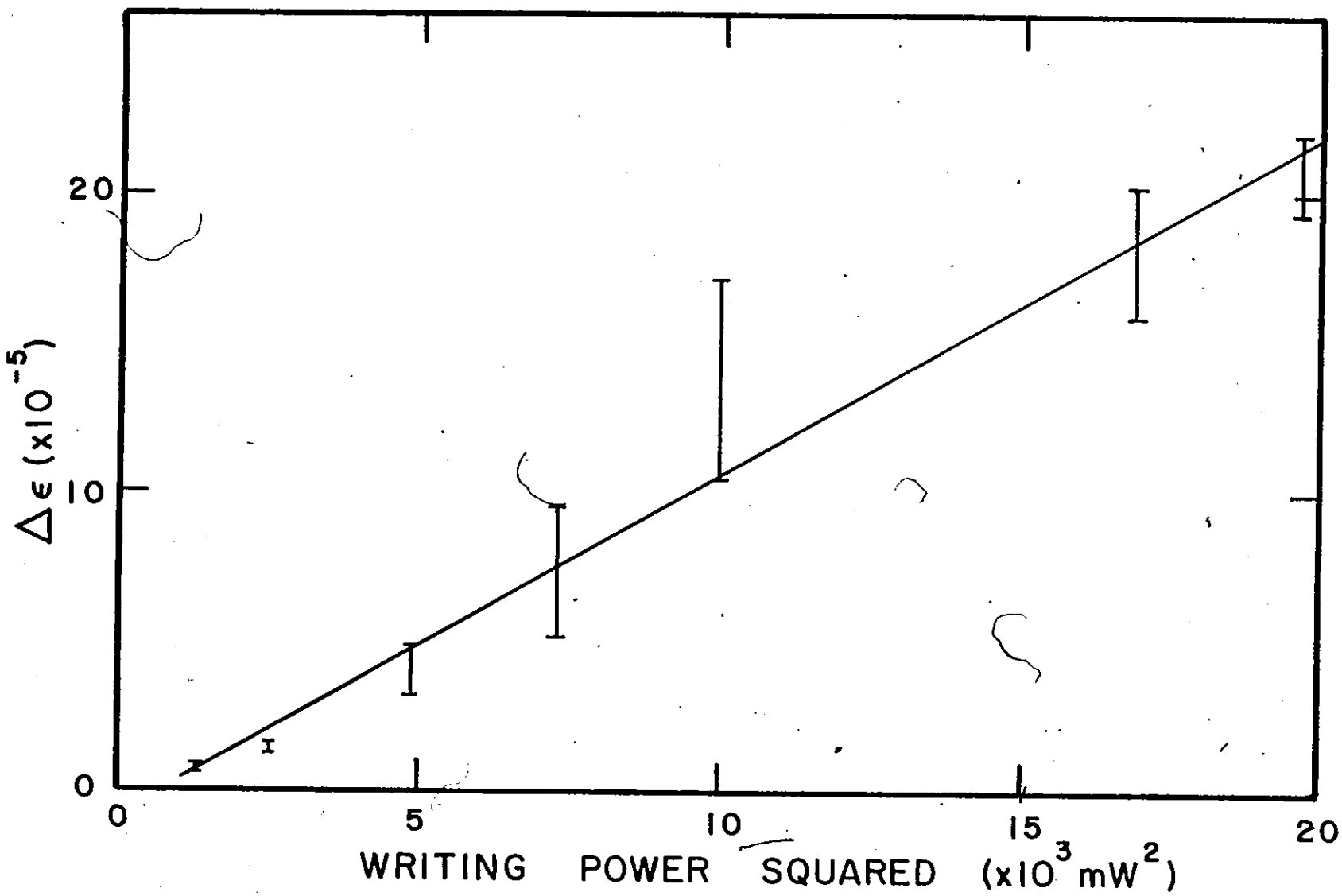
20
10
0
$\Delta\epsilon$ ($\times 10^{-5}$)
0
5
10
15
20
WRITING POWER SQUARED ($\times 10^{3}$ mW^{2})

FIGURE 4.13

Spectral bandwidth of the filter as a function of the writing power.

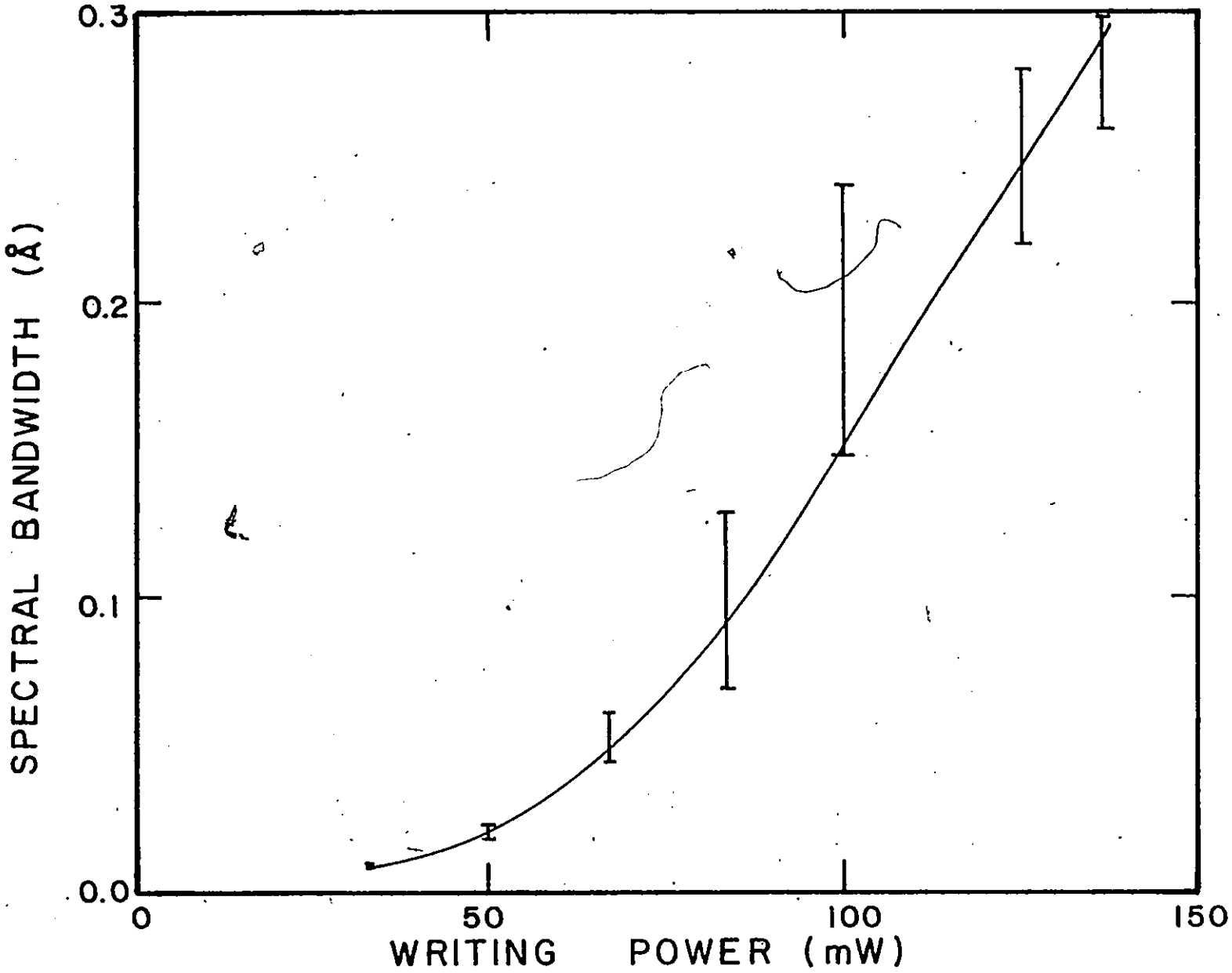
0.3
0.2
0.1
0.0
SPECTRAL BANDWIDTH (Å)
0
50
100
150
WRITING POWER (mW)

FIGURE 4.14

Peak to peak anomalous dispersion $\Delta\beta_{pp}$ of the filter as a function of the writing power.

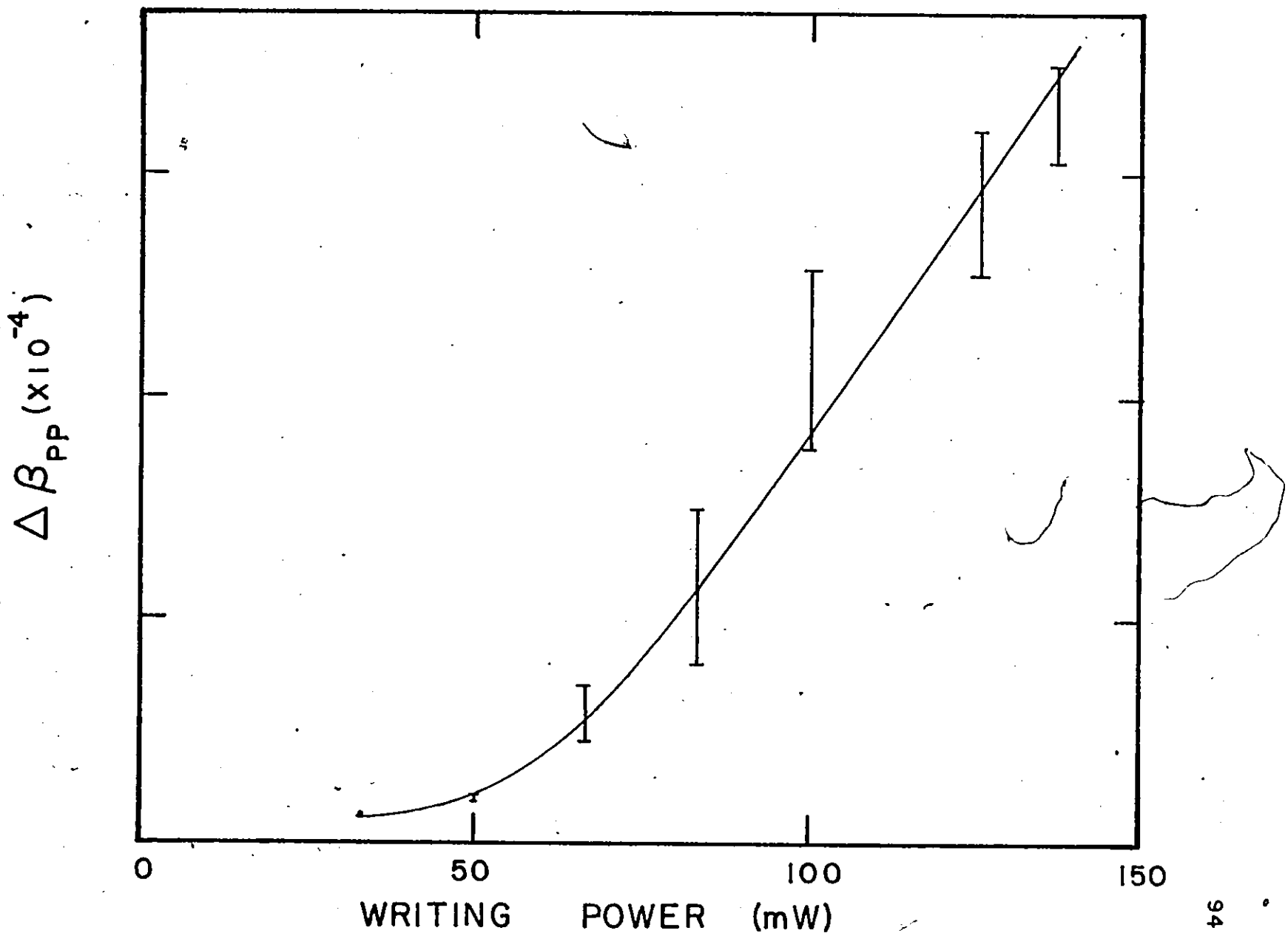
$\Delta\beta_{PP}$ ($\times 10^{-4}$)
0
50
100
150
WRITING POWER (mW)

4.5 DISCUSSION

The spectral bandwidth of 0.01-0.03 Å shown in the last section is extremely narrow in comparison to the conventional filters and hence makes optical fibre filters potentially very important in situations where high resolution is required. For instance, they may be used as resonant reflectors in lasers as demonstrated by Hill and Kawasaki [21]. Also, because of their extremely small size, it is possible to end-butt them to the presently very popular heterojunction injection lasers used in Optical Communications System (OCS) as external reflectors. Furthermore, they are potentially very important in Wavelength-Division-Multiplexing in OCS because the $R(\lambda)$ is narrow and sharp - i.e. fast decaying on either side of the central maximum with no significant side lobes as shown in Figs. 2.3 and 2.4 - which means that many channels can be packed together in a small spectral region. Present WDM schemes usually employ gratings as the multiplexers and demultiplexers which generally require a wavelength spacing of the order of 100 Å or more between adjacent channels [16-20]. Using optical fibre filters in WDM scheme, a wavelength spacing of a few angstroms is the most that is required. Furthermore, sources for this WDM scheme can be of the same material but simply of different doping level [51] or better yet, identical sources but operating at different temperature and hence different wavelengths [52].

In regard to the available anomalous dispersion from the optical fibre filters, it is interesting to know if it can be used to equalize the material dispersion present in typical Optical Communication (OC)

links employing single mode fibres. Basically, there are two requirements that a filter must satisfy in order to equalize material dispersion. One is that its anomalous dispersion is comparable to the material dispersion in the link and the other is that its spectral bandwidth is comparable to that of the source. In Appendix D, the relationship between material dispersion and anomalous dispersion is derived. Applying the available anomalous dispersion obtained here and data on material dispersion for typical OC links, we find that in the spectral region of ~1.2 - 1.3 μ for an assumed spectral bandwidth of 1 Å, the material dispersion which occurs in an OC link of up to 38 Km long can be equalized by a single pass through an optical fibre filter.

Finally, it is important to recall that the fibre used in these experiments has only 4% GeO_2 dopant concentration in the core. It is not unreasonable to suppose that the induced index perturbation would scale up with increased GeO_2 dopant concentration. This receives support from the fact that similar photo-induced refractive index change in $LiNbO_3$ [53], $As_{40}Se_{15}S_{35}Ge_{10}$ [54], polymethyl methacrylate (PMMA) [55-56] and α-diketone camphorquinone [57] gives values of index change commensurate with that calculated for pure GeO_2 material by simply scaling up the values reported here for the 4% doped material (i.e. x 25). The values of the photo-induced index change for the various materials listed above are shown in Table 4.4.

If the estimated photo-induced index change for pure GeO_2 shown in Table 4.4 is indeed an obtainable value, then according to the theory developed in Chapter 2, this corresponds to a spectral bandwidth ($\Delta\lambda_t$)

TABLE 4.4

Induced index perturbation ($\Delta\varepsilon$) in pure GeO_2 and other photosensitive material.

Material	$\Delta\varepsilon$	Reference
GeO_2	5×10^{-3}*	present work
$LiNbO_3$	10^{-3}	[53]
$As_{40}Se_{15}S_{35}Ge_{10}$	10^{-2}	[54]
PMMA	3×10^{-3}	[55-56]
α-diketone camphorquinone	10^{-3}	[57]

* At writing power = 82 mW, $\Delta\varepsilon = (1.92 - 2.18) \times 10^{-4}$ or $\Delta\varepsilon_{averaged} \simeq 2.0 \times 10^{-4}$. This value is for 4% dopant concentration of GeO_2. For pure GeO_2, $\Delta\varepsilon$ is expected to be roughly $25 \times 2.0 \times 10^{-4} = 5 \times 10^{-3}$.

of 6.85 Å and peak to peak anomalous dispersion ($\Delta\beta_{pp}$) of $1.59 \times 10^{-2}/\mu$. Hence, it can be seen that broadband optical fibre filters having high anomalous dispersion can be made.

A final remark that should be made here is that the deduced $\Delta\varepsilon$ reported here is not an upper limit for the 4% GeO_2 doped SiO_2 single mode fibre as we did not observe any sign of the saturation of the induced index perturbation $\Delta\varepsilon$ over the range of writing power used in the experiments. Hence, higher values of $\Delta\varepsilon$ for pure GeO_2 and optical fibre filters of spectral bandwidth broader than 6.85 Å can be expected.

CHAPTER 5

SUMMARY AND SUGGESTIONS FOR FURTHER RESEARCH

In this final chapter, we present a summary of both the theory and the experiments reported in this thesis. Important conclusions are drawn and suggestions for further research aimed at developing a better understanding of the basic processes in the realization of practical optical fibre filters are presented.

In the theoretical analysis of optical fibre filters, Coupled Mode Theory was used and found to be adequate for the range of writing power used in the experiments. Using the theoretical model developed, we were able to predict the functional dependence of spectral bandwidth ($\Delta\lambda_t$) and effective cutoff length (L_{cutoff}) of the filters on the induced index perturbation ($\Delta\varepsilon$). It was found that $\Delta\lambda_t$ increases linearly with $\Delta\varepsilon$ whereas L_{cutoff} decreases nonlinearly with $\Delta\varepsilon$. Also, anomalous dispersion is predicted in the stopband region of the filter which increases with higher value of $\Delta\varepsilon$. This indicates the possibility of using optical fibre filters to equalize material dispersion in Optical Communication links employing single mode fibres.

In the experimental work, optical fibre filters of different writing powers (WP) were first fabricated by irradiating the fibres with an Argon laser operating on a single mode and single line. These filters were then divided into 2 groups because there were two experiments to be done. One is to obtain the effective cutoff length

(L_{cutoff}) of the filters whereas the other is to obtain the spectral bandwidth of the filters as a function of the writing power. The reason that two experiments were used is that, from the theoretical predictions, it was realized that data on L_{cutoff} is reliable in low WP region whereas data on $\Delta\lambda_t$ is more reliable in the high WP region. By using both experiments, not only can good results be obtained in both the high and low WP regions, it also serves the purpose of testing the reliability of the two methods of determining $\Delta\varepsilon$ by examining to what extent they agree with each other in the moderate WP region.

From the experimental results, it was found that spectral bandwidth ($\Delta\lambda_t$) of the filters increases with the writing power whereas effective cutoff length (L_{cutoff}) of the filters decreases with the writing power. Comparing these experimental results with the theory, it was deduced that in the range of writing power used (35-140 mW), $\Delta\varepsilon$, $\Delta\lambda_t$ and L_{cutoff} have corresponding ranges of 0.8×10^{-5} to 2.1×10^{-4}, 0.01 Å to 0.3 Å and 16 cm to 0.54 cm respectively. Also the induced index perturbation was related to the WP and curves were plotted (Figs. 4.11 and 4.12) which showed that $\Delta\varepsilon$ is dependent on the square of the writing power for the range of writing power used in the experiments. It is important to mention here that the two experiments on $\Delta\lambda_t$ and L_{cutoff} were found to agree with each other in the moderate WP region of 85-100 mW, indicating that they are reliable in this region.

When comparing the induced index perturbation $\Delta\varepsilon$ (at maximum writing power) obtained here for the 4% GeO_2 doped SiO_2 fibre with that of other photosensitive materials such as $LiNbO_3$, $As_{40}Se_{15}S_{35}Ge_{10}$ and

PMMA, it was deduced that for bulk GeO_2, a $\Delta\varepsilon$ of 5×10^{-3} is quite possible. At this particular value of $\Delta\varepsilon$, our theory predicts a spectral bandwidth of 6.85 Å and hence, broadband optical fibre filters is a definite possibility. Furthermore, the fact that the deduced $\Delta\varepsilon$ in the experiments is not an upper limit for the 4% GeO_2 (as there was no sign of saturation for the range of writing power used) implies that a value of $\Delta\varepsilon > 5 \times 10^{-3}$ for pure GeO_2 and filters of spectral bandwidth broader than 6.85 Å are possible.

In regard to the exploitation of the available anomalous dispersion in optical fibre filters to equalize material dispersion in Optical Communication (OC) system employing single mode fibres, we found that in the spectral region of ~1.2 - 1.3 μ with a spectral bandwidth of 1 Å, material dispersion in OC links of more than 38 Km long can be equalized by a single pass through the filters. This, together with the fact that using optical fibre filters as multiplexers and demultiplexers in Wavelength-Division-Multiplexing in OC system allows a lot of channels to be packed into a small spectral bandwidth enhances the possibility of OC system employing long link and high data rate. In essence, the length-bandwidth product in OC system is improved.

Several important observations should be mentioned here. First of all, it was observed in the experiment of fabricating filters that the latter reflects only the lowest order mode (HE_{11}). The reason for this was shown to be due to the lower intensity obtained for the higher order modes of HE_{21} and EH_{01}. Secondly, the filters were found to be extremely sensitive to even very minor temperature variation. Because

of this, reflectance fluctuation due to the detuning of filter resonant wavelength during or even after the writing process was observed. Furthermore the present experimental arrangement prohibits the fabrication of filters for writing power > 160 mW, probably because significant joule heating was induced at this high level of writing power. Thirdly, the fabrication of 4% GeO_2 doped SiO_2 optical fibre filters is proved to be superior to that of many other photosensitive material in the sense that it takes a very short time (range from 1 to slightly over 10 minutes as shown in Table 3.1) and requires no heat treatment or UV fixing. Furthemore, the optical fibre filters were found to be permanent filters as no degradation of performance was observed over a period of more than two weeks. Finally, it was observed that they can be erased by applying a small flame to them for a short period of time.

In conclusion, we have delineated some basic characteristics of optical fibre filters based on the photosensitivity of GeO_2 in terms of the spectral bandwidth, small size (short effective cutoff length) and high reflectance. Broad bandwidth filters of up to 7 Å are a possibility for pure GeO_2 fibre and the exploitation of the available anomalous dispersion to equalize material dispersion is shown to be achievable. Further research is needed in this field of photosensitivity-based filters for a better understanding of the physical processes involved in the writing mechanism and subsequent realization of its ultimate performance. For instance, determining the exact index perturbation profile by performing the grating experiment in

bulk or thin film material described in Chapter 3 will help us to understand the writing mechanism and to determine at what writing power saturation can be produced. Experimental systems designed to control temperature stability should be investigated because should temperature be a directly controllable parameter, a lot of important and interesting experiments can be done. For instance, filters of higher writing power can be written and the saturation value of the induced index perturbation can thus be determined. Upon determining this saturation value, the ultimate performance of the optical fibre filters can be evaluated. Furthermore, controllable temperature means that tunable filters can be made by simply adjusting the temperature. Since filters of high writing power have short length, they could be enclosed in a suitable temperature controlled system, hence making tunable filters a distinct possibility. Employing this temperature control again, if a stable temperature gradient can be applied to fibres during the writing process, a chirped grating [58-60] or index perturbation profile can be made and thus giving rise to broadband filters even at low writing power. Other important research includes the writing of multifilters in a single fibre for uses in Wavelength-Division-Multiplexing system, transient filter by temperature control again and filters operating in the infrared region by employing the appropriate difference between two frequencies in the visible region. Finally, in view of the fact that the writing process in the 4% GeO_2 doped SiO_2 single mode fibre is very efficient in that it takes a short time and requires no heat treatment or UV fixing, this material should be employed in thin film devices that

are currently generating much attention in the field of Integrated Optics. It is hoped that the work reported in this thesis has served the purpose of introducing optical fibre filters as novel and important devices in Optical Communications Systems and stimulated further research in their development.

APPENDIX A

EXPRESSIONS FOR LINEARLY POLARIZED ELECTRIC AND MAGNETIC FIELDS IN OPTICAL FIBRES

If, instead of writing E_z and H_z as shown in Eqs. (2.9) and (2.10) for the core region and Eqs. (2.17) and (2.18) for the cladding region, we use the following:

$$E_z = \frac{iA\kappa}{2\beta_\nu}\left[J_{\nu+1}(\kappa r)\begin{Bmatrix}\cos(\nu+1)\phi\\ \sin(\nu+1)\phi\end{Bmatrix} - J_{\nu-1}(\kappa r)\begin{Bmatrix}\cos(\nu-1)\phi\\ \sin(\nu-1)\phi\end{Bmatrix}\right] \quad (A.1)$$

$$H_z = \frac{iA\kappa}{2k}\left(\frac{\varepsilon_o}{\mu_o}\right)^{1/2}\left[J_{\nu+1}(\kappa r)\begin{Bmatrix}\sin(\nu+1)\phi\\ -\cos(\nu+1)\phi\end{Bmatrix} + J_{\nu-1}(\kappa r)\begin{Bmatrix}\sin(\nu-1)\phi\\ -\cos(\nu-1)\phi\end{Bmatrix}\right] \quad (A.2)$$

for the core region and

$$E_z = -\frac{A\gamma}{2\beta_\nu}\,\frac{J_\nu(\kappa a)}{H_\nu^{(1)}(i\gamma a)}\left[H_{\nu+1}^{(1)}(i\gamma r)\begin{Bmatrix}\cos(\nu+1)\phi\\ \sin(\nu+1)\phi\end{Bmatrix} - H_{\nu-1}^{(1)}(i\gamma r)\begin{Bmatrix}\cos(\nu-1)\phi\\ \sin(\nu-1)\phi\end{Bmatrix}\right] \quad (A.3)$$

$$H_z = -\frac{A\gamma}{2k}\left(\frac{\varepsilon_o}{\mu_o}\right)^{1/2}\frac{J_\nu(\kappa a)}{H_\nu^{(1)}(i\gamma a)}\left[H_{\nu+1}^{(1)}(i\gamma r)\begin{Bmatrix}\sin(\nu+1)\phi\\ -\cos(\nu+1)\phi\end{Bmatrix} + H_{\nu-1}^{(1)}(i\gamma r)\begin{Bmatrix}\sin(\nu-1)\phi\\ -\cos(\nu-1)\phi\end{Bmatrix}\right] \quad (A.4)$$

for the cladding region with all the symbols in Eqs. (A.1) - (A.4) being as defined in Chapter 2. Application of Eqs. (2.11) and (2.12) to Eqs. (A.1- A.4) then gives

$$E_x = A J_\nu(\kappa r) \begin{Bmatrix} \cos(\nu\phi) \\ \sin(\nu\phi) \end{Bmatrix} \tag{A.5}$$

$$H_y = nA \frac{\beta_\nu}{|\beta_\nu|} \left(\frac{\varepsilon_o}{\mu_o}\right)^{1/2} J_\nu(\kappa r) \begin{Bmatrix} \cos(\nu\phi) \\ \sin(\nu\phi) \end{Bmatrix} \tag{A.6}$$

$$E_y = 0 \tag{A.7}$$

$$H_x \simeq 0 \tag{A.8}$$

for the core region and

$$E_x = A \frac{J_\nu(\kappa a)}{H_\nu^{(1)}(i\gamma a)} H_\nu^{(1)}(i\gamma r) \begin{Bmatrix} \cos(\nu\phi) \\ \sin(\nu\phi) \end{Bmatrix} \tag{A.9}$$

$$H_y = nA \frac{\beta_\nu}{|\beta_\nu|} \left(\frac{\varepsilon_o}{\mu_o}\right)^{1/2} \frac{J_\nu(\kappa a)}{H_\nu^{(1)}(i\gamma a)} H_\nu^{(1)}(i\gamma r) \begin{Bmatrix} \cos(\nu\phi) \\ \sin(\nu\phi) \end{Bmatrix} \tag{A.10}$$

$$E_y = 0 \tag{A.11}$$

$$H_x \simeq 0$$

for the cladding region.

APPENDIX B

THE EFFECT ON THE FULL WIDTH HALF MAXIMUM OF SPECTRAL REFLECTANCE CURVES ($R(\lambda)$) FOR VERY LARGE PHYSICAL FILTER LENGTH

An examination of Eqs. (2.65) and (2.66) shows that the half maximum points of the spectral reflectance curve $R(\lambda)$ always occur in the passband region. Consequently, only Eq. (2.66) is required for the following analysis.

If, for the moment, it is assumed that the physical length (L_{phy}) is much greater than the effective cutoff length (L_{cutoff}) of the filter, then Eq. (2.68) (repeated below for convenience) is applicable.

$$R(\lambda) = \frac{\Omega^2}{\Delta\beta^2} \tag{2.68}$$

The half maximum points therefore occur at

$$R(\lambda) = \frac{\Omega^2}{\Delta\beta^2} = 0.5 \tag{B.1}$$

or

$$\Delta\beta = \pm\Omega/2 \tag{B.2}$$

If on the other hand $L_{phy} < L_{cutoff}$ for $\lambda \neq \lambda_c$ where λ_c is the Bragg wavelength as defined in Chapter 2, then it implies Eq. (2.66)

$$R(\lambda) = \frac{\Omega^2 \sin^2 (QL)}{\Delta\beta^2 - \Omega^2 \cos^2 (QL)} \tag{2.66}$$

has to be used to find the half maximum points. Consequently, we set $R(\lambda)$ equal to 0.5 and solve for $\Delta\beta$:

$$R(\lambda) = \frac{\Omega^2 \sin^2 (QL)}{\Delta\beta^2 - \Omega^2 \cos^2 (QL)} = 0.5 \tag{B.3}$$

$$\Leftrightarrow 2\Omega^2 \sin^2(QL) = \Delta\beta^2 - \Omega^2 \cos^2 (QL)$$

$$\Leftrightarrow \Delta\beta = \pm\Omega(1 + \sin^2(QL))^{1/2} \tag{B.4}$$

which is a transcendental equation as $Q = (\Delta\beta^2 - \Omega^2)^{1/2}$. However, to a first approximation, the average of $\sin^2(QL)$ is equal to 0.5 and therefore Eq. (B.4) becomes

$$\Delta\beta = \pm\Omega(1.5)^{1/2} \tag{B.5}$$

If we consider the relative difference between Eq. (B.2) and (B.5), then it can be shown that

$$\frac{\Delta\lambda_1}{\Delta\lambda_2} = \frac{\Delta\beta_1}{\Delta\beta_2} \tag{B.6}$$

Letting $\Delta\beta_1$ and $\Delta\beta_2$ be the expressions from Eqs. (B.2) and (B.5) respectively, the full width half maximum of $R(\lambda)$ is therefore broader in the case of $L_{phy} >> L_{cutoff}$ than in the case of $L_{phy} < L_{cutoff}$ for $\lambda \neq \lambda_c$ by a factor of

$$\Delta\lambda_1/\Delta\lambda_2 = \sqrt{2}/\sqrt{1.5} = 1.15 \tag{B.7}$$

APPENDIX C

CALCULATION OF THE AVERAGE INTENSITY CARRIED BY THE DIFFERENT PROPAGATING MODES IN THE NEAR SINGLE MODE FIBRE

The three allowed modes of HE_{11}, HE_{21} and EH_{01} in the near single mode fibre are essentially only two modes because the last two are degenerate due to the minute refractive index difference between the core and the cladding. In the Linear Polarized Fields notation [42], $LP_{01} = HE_{11}$ and $LP_{11} = HE_{21}$ and EH_{01}. The observed round spot, 2 lobes and 3 lobes far field pattern (FFP) from the output end of the fibre correspond respectively to mode HE_{11}, mode HE_{21} or EH_{21} depending on the orientation of the field and hybrid mode of HE_{21} and EH_{21} - that is, a linear combination of modes HE_{21} and EH_{01}. Because the magnitude of this hybrid mode cannot be greater than that of either HE_{21} or EH_{01} alone, for the purpose of demonstrating that the lowest order mode has a much higher average intensity in the core region of the fibre, it is sufficient to calculate only the average intensity in HE_{11} and HE_{21} or EH_{01}.

The average intensity in the core region for different modes can be found from Eq. (2.29) by setting the limit on r to the core radius "a" instead of ∞. Substituting Eqs. (2.18) - (2.16) into Eq. (2.29) and evaluating the integral gives:

$$P_{core} = e_{\nu}\ \theta A^2\ [J_{\nu}^2(\kappa a) - J_{\nu+1}(\kappa a)\ J_{\nu-1}(\kappa a)] \qquad (C.1)$$

where

$$e_\nu = 2 \text{ for } \nu = 1 \qquad (C.2)$$
$$= 1 \text{ for } \nu \neq 0$$

and

$$\theta = \frac{\pi}{4} a^2 \left(\frac{n_{core} + n_{clad}}{2}\right) \left(\frac{\varepsilon_o}{\mu_o}\right)^{1/2} = \text{constant with respect to } \nu \qquad (C.3)$$

The constant A^2 in Eq. (C.1) can be determined by using Eq. (2.30) shown in Chapter 2 and below for convenience

$$A^2 = \frac{1}{\theta} \frac{\gamma^2}{e_\nu} \frac{P_{total}}{(n^2_{core} - n^2_{clad})\, k^2\, |J_{\nu-1}(\kappa a)\, J_{\nu+1}(\kappa a)|} \qquad (2.30)$$

where

P_{total} = total power.

In order to make a correct comparison between the average intensity carried by the different modes in the core region, each of their total power in Eq. (2.30) must be normalized to the same value. For simplicity, choose $P_{total} = 1.0$ and therefore

$$A^2 = \frac{1}{\theta} \frac{\gamma^2}{e_\nu} \frac{1}{\alpha} \frac{1}{|J_{\nu-1}(\kappa a)\, J_{\nu+1}(\kappa a)|} \qquad (C.4)$$

where $\alpha = (n^2_{core} - n^2_{clad})k^2$ = constant with respect to ν.

Substituting Eq. (C.4) into Eq. (C.1) gives

$$P_{core} = \frac{\gamma^2}{\alpha} \left[\frac{J^2_\nu(\kappa a)}{|J_{\nu+1}(\kappa a) J_{\nu-1}(\kappa a)|} - \frac{J_{\nu+1}(\kappa a) J_{\nu-1}(\kappa a)}{|J_{\nu+1}(\kappa a) J_{\nu-1}(\kappa a)|}\right] \qquad (C.5)$$

For the first mode (HE_{11}), $\nu = 0$ and Eq. (C.5) becomes

$$P_1 = \frac{\gamma_o^2}{\alpha} \left[\frac{J_o^2(\kappa a)}{J_1^2(\kappa a)} + 1\right] \tag{C.6}$$

where

$$\gamma_o^2 = (\beta_o{}^2 - n_2^2 k^2) \tag{C.7}$$

and

$$\beta_o = \text{eigen value of Eq. (2.25) for } \nu = 0 \tag{C.8}$$

For the second mode (HE_{21} or EH_{01}) $\nu = 1$ and Eq. (C.5) becomes

$$P_2 = \frac{\gamma_1^2}{\alpha} \left[\frac{J_1^2(\kappa a)}{|J_2(\kappa a)\ J_o(\kappa a)|} - \frac{J_2(\kappa a)\ J_0(\kappa a)}{|J_2(\kappa a)\ J_o(\kappa a)|}\right] \tag{C.9}$$

where

$$\gamma_1^2 = (\beta_1^2 - n_2^2 k^2) \tag{C.10}$$

and

$$\beta_1 = \text{eigenvalue of Eq. (2.25) for } \nu = 1$$

Since α is a constant with respect to ν, it is ignored and an arbitrary unit Ψ is assumed for P_1 and P_2. Evaluating Eq. (2.25) for β_o and β_1 and subsequently substituting the latter into Eqs. (C.6) and (C.9) give

$$P_1 = 2.93\ \Psi \tag{C.12}$$

$$P_2 = 0.173\ \Psi \tag{C.13}$$

and

$$P_1/P_2 = 17 \tag{C.14}$$

For the Hybrid mode which is a linear combination of EH_{01} and HE_{21}, its average intensity (P_h) in the core region cannot be greater than that of the second mode (P_2). That is

$$P_h \leq 0.173\ \Psi \tag{C.15}$$

and

$$P_1/P_h \geq 17 \tag{C.16}$$

Equations (C.14) and (C.15) clearly show that the average intensity carried by the first mode in the core region is significantly larger than that by the higher and hybrid modes.

APPENDIX D

ANALYSIS ON EQUALIZATION OF MATERIAL DISPERSION BY ANOMALOUS DISPERSION IN SINGLE MODE OPTICAL FIBRE FILTERS

The spectral intensity distribution of a source used in an arbitrary Optical Communication (OC) link and the dispersion curve for a filter whose spectral bandwidth is comparable to that of the source are shown in Fig. D.1. Since the single mode optical fibre used in the OC link is dispersive, pulses of different wavelengths in the spectral bandwidth defined by the source will therefore travel at different group velocities (v_g) which is defined as

$$v_g = \frac{d\omega}{d\beta} \tag{D.1}$$

The transit time over a link of length L is

$$\tau = L \frac{d\beta}{d\omega} \tag{D.2}$$

and for different v_g, τ will be different accordingly. The differential time delay between wavelengths λ_1 and λ_2 shown in Fig. D.1 is

$$\Delta\tau = \tau_2 - \tau_1 = L \left[\left(\frac{d\beta}{d\omega}\right)_2 - \left(\frac{d\beta}{d\omega}\right)_1\right]. \tag{D.3}$$

For small refractive index difference between the core and cladding of the fibre such that Linearly Polarized Fields [42] are valid and considering the lowest order mode (HE_{11}) only, the quantity

FIGURE D.1

Diagram (A) shows the spectral intensity of an arbitrary source of spectral bandwidth $\lambda_2 - \lambda_1$ whereas diagram (B) shows the dispersion curve of an optical fibre filter that has comparable spectral bandwidth. The dotted line in diagram (B) represents the dispersion curve for an optical fibre.

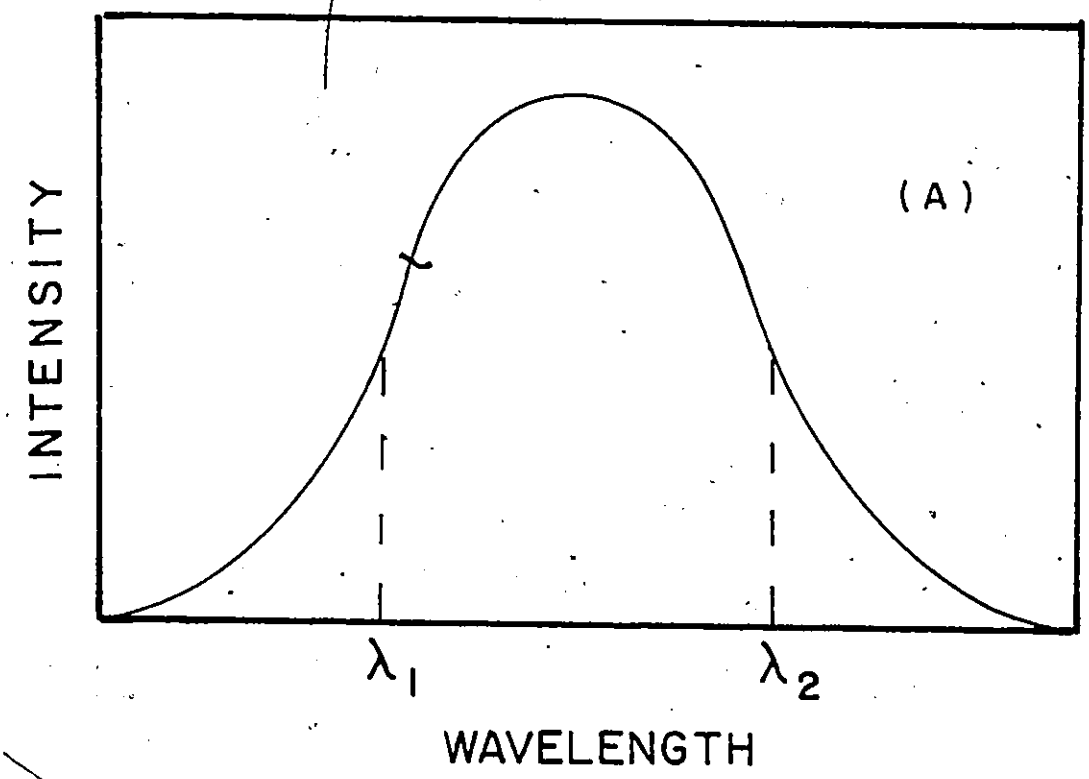
INTENSITY
(A)
λ1
λ2
WAVELENGTH

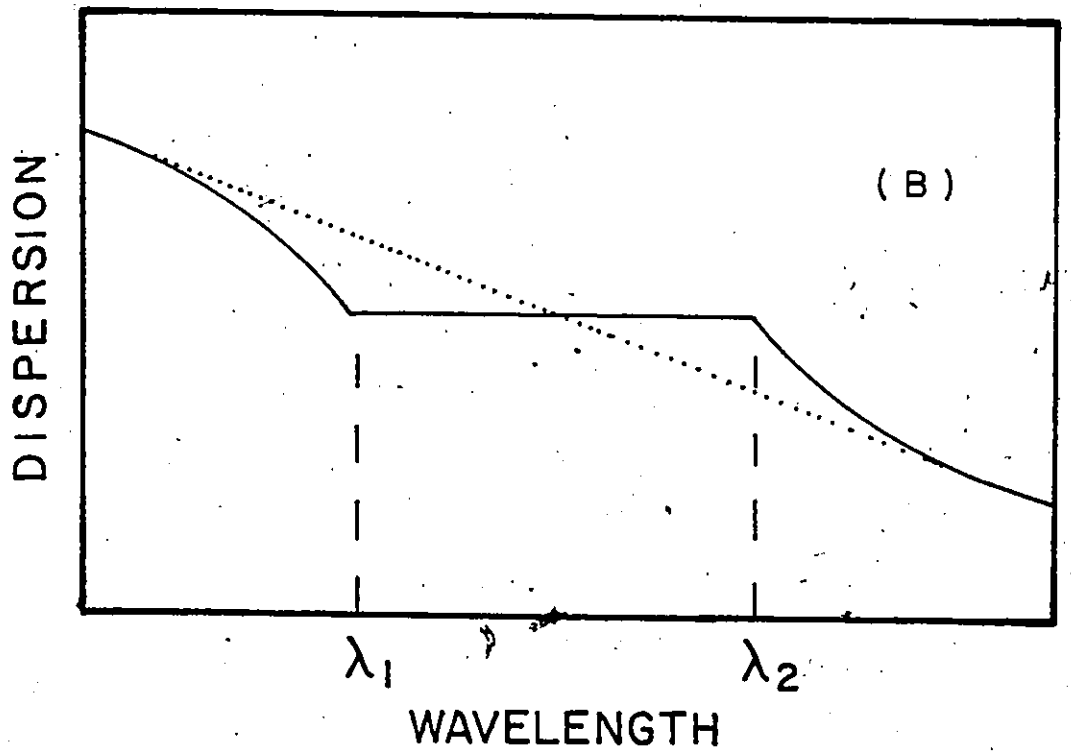
DISPERSION
(B)
λ1
λ2
WAVELENGTH

$$\Delta\tau_m = \Delta\tau/L \tag{D.4}$$

is essentially the material dispersion per length*. Table D.1 shows typical values for the case of 1 Å spectral bandwidth which gives a material dispersion/length of approximately 10^{-4} psec/Km. In order to equalize this material dispersion effectively by the anomalous dispersion in optical fibre filters, the magnitude of the anomalous dispersion must be comparable to the product of 10^{-4} psec/Km and the length of the OC link. In the following analysis, this maximum length of OC link such that equalization of material dispersion by anomalous dispersion is still achievable is determined.

Rewriting Eq. (D.1) as

$$v_g = c\ dk/d\beta \tag{D.5}$$

where β is the propagation constant in the optical fibre filter and k is the plane wave propagation constant, Eq. (D.2) can therefore be written as

$$\tau = \frac{L}{c}\ \frac{d\beta}{dk} \tag{D.6}$$

where L is the effective cutoff length of the filter. It has been shown by Marcuse [44] that for small refractive index difference between the core and cladding which is the case here,

---

* Waveguide dispersion is negligible to HE_{11}.

TABLE D.1

MATERIAL DISPERSION DATA FOR TYPICAL OPTICAL COMMUNICATION LINKS

System	Operating Wavelength (μ)	Material Dispersion/Length at 1 Å spectral bandwidth (psec/km)	References
A	1.276	1.24×10^{-4}	[61]
B	1.22	1.5×10^{-4}	[62]
C	1.34	1.1×10^{-4}	[63]

$$\frac{d\beta}{dk} = \frac{\alpha}{k} \left(1 - \frac{2\, J_\nu^2(\kappa a)}{J_{\nu-1}(\kappa a) J_{\nu+1}(\kappa a)}\right) \tag{D.7}$$

where

$$\alpha = (\beta - n_2\, k) \tag{D.8}$$

and

$$\kappa = (n_1^2\, k^2 - \beta^2)^{1/2} \text{ as defined in Chapter 2.} \tag{D.9}$$

For the lowest order mode (HE_{11}), Eq. (D.7) becomes

$$\frac{d\beta}{dk} = \frac{\alpha}{k} \left(1 + \frac{2\, J_o^2\, (\kappa a)}{J_1^2(\kappa a)}\right) \tag{D.10}$$

Substituting Eq. (D.10) into Eq. (D.6) gives

$$\tau = \frac{L}{c}\, \frac{\alpha}{k} \left(1 + \frac{2\, J_o^2(\kappa a)}{J_1^2(\kappa a)}\right) \tag{D.11}$$

The differential time delay between wavelength λ_1 and λ_2 due to the anomalous dispersion in the filter is therefore

$$\Delta\tau_f = \frac{L}{c} \left\{ \frac{\alpha}{k} \left(1 + \frac{2J_o^2(\kappa a)}{J_1^2(\kappa a)}\right)\Bigg|_{\lambda_2} - \frac{\alpha}{k} \left(1 + \frac{2J_o^2(\kappa a)}{J_1^2(\kappa a)}\right)\Bigg|_{\lambda_1} \right\} \tag{D.12}$$

Using a spectral bandwidth of 1 Å in the filter and evaluating Eq. (D.12) gives

$$\Delta\tau = 4.2 \times 10^{-3} \text{ psec} \tag{D.13}$$

When this value of $\Delta\tau_f$ is compared with the value of differential time

delay per length due to material dispersion listed in Table D.1, it indicates that material dispersion in Optical Communication links of close to 40 Km can be equalized by optical fibre filters. The exact values of the length of the Optical Communication links are shown in Table D.2.

TABLE D.2

Maximum allowable length of optical communication links for effective material dispersion equalization by the anomalous dispersion in optical fibre filters.

System	Maximum Length (Km)
A	34
B	28
C	38

REFERENCES

[1] S.E. Miller, E.A.J. Marcatili and T. Li, Proc. IEEE 61, 1703, (1973).

[2] L.L. Campbell, Fiber and Integrated Optics, 1, 21 (1977).

[3] J. Conradi, F.P. Kapron and J.C. Dyment, IEEE Solid-State Circuits 13, 106 (1978).

[4] T.G. Giallorenzi, Proc. IEEE 66, 744 (1978).

[5] S.E. Miller and A.G. Chynoweth, Optical Fibre Communications (1979).

[6] G. Gliemeroth, D. Krause and N. Neuroth, Elect. Lett. 13, 452 (1977).

[7] M. Saruwatari, K. Asatani, J. Yamada, I. Halakeyama, K. Sugiyama and T. Kimura, Elect. Lett 14, 187 (1978).

[8] S. Machida, J. Yamada, T. Mukai, Y. Horikoshi and H. Tsuchiya, Elect. Lett. 15, 219 (1979).

[9] H.F. Wolf, Overview of Optical Fiber Systems Market, Intelcom 77, Atlanta, Georgia, October 1977.

[10] P. Leigh, Fiber and Integrated Optics 2, 99 (1979).

[11] D. Gloge, Appl. Optics 10, 2442 (1971).

[12] S. Geckeler, Appl. Optics 17, 1073 (1978).

[13] S.H. Remple, Appl. Optics 18, 31 (1979).

[14] D. Marcuse, Appl. Optics 18, 2930 (1979).

[15] S. Sudo, H. Okazaki, M. Nakahara and M. Horiguchi, Elec. Lett. 16, 280 (1980).

[16] W.J. Tomlinson and C. Lin, Elect. Lett. 14, 347 (1978).

[17] K. Aoyama and J.C. Minowa, Appl. Optics 18, 1253 (1979).

[18] K. Aoyama and J.C. Minowa, Appl. Optics 18, 2834 (1979).

[19] R. Watanabe and K. Nosu, Elect. Lett. 16, 106 (1980).

[20] R. Watanabe, K. Nosu and Y. Fujii, Elect. Lett. 16, 108 (1980).

[21] K.O. Hill, Y. Fujii, D.C. Johnson and B.S. Kawasaki, Appl. Phys. Lett. 32, 647 (1978).

[22] D.C. Flanders, H. Kogelnik, R.V. Schmidt and C.V. Shank, Appl. Phys. Lett. 24, 194 (1974).

[23] R.V. Schmidt, D.C. Flanders, C.V. Shank and R.D. Stanley, Appl. Phys. Lett. 25, 651 (1974).

[24] C.S. Hong, J.B. Shellan, A.C. Livanos, A. Yariv and A. Katzir, Appl. Phys. Lett. 31, 276 (1977).

[25] S.T. Peng, T. Tamir and H.L. Bertoni, Elec. Letts. 9, 150 (1973).

[26] F.W. Dabby, A. Kestenbaum and U.C. Paek, Optics Comm. 6, 125 (1972).

[27] Kyokei Sakuda and A. Yariv, Optics Comm. 8, 1 (1973).

[28] C. Elachi and C. Yeh, J. Appl. Phys. 44, 3146 (1973).

[29] S.T. Peng, H.L. Bertoni and T. Tamir, Optics Comm. 10, 91 (1974).

[30] D.G. Dalgoutte and C.D.W. Wilkinson, Appl. Optics 14, 2983 (1975).

[31] S.T. Peng and T. Tamir, Optics Comm. 11, 405 (1974).

[32] K.C. Chang and T. Tamir, Optics Comm. 26, 327 (1978).

[33] A. Yariv, IEEE J.Q.E. 9, 919 (1973).

[34] Harold Stoll and A. Yariv, Optics Comm. 8, 5 (1973).

[35] D. Marcuse, B.S.T.J. 52, 817 (1973).

[36] A. Yariv and M. Nakamura, IEEE J.Q.E. 13, 233 (1977).

[37] A. Yariv and A. Gover, Appl. Phys. Lett. 26, 537 (1975).

[38] D.L. Jaggard and G.A. Evans, Antenna Lab. Tech. Report No. 73 (1975).

[39] D.L. Jaggard and C. Elachi, J.O.S.A. 66, 674 (1976).

[40] G.A. Evans, Ph.D. Dissertation, C.I.T. (1975).

[41] A.W. Snyder, IEEE M.T.T. 17, 1130 (1969).

[42] D. Gloge, Appl. Optics 10, 2252 (1971).

[43] A.W. Snyder and W.R. Young, J.O.S.A. 68, 297 (1978).

[44] D. Marcuse, Theory of Dielectric Optical Waveguides, Academic Press (1974).

[45] Hecht and Zajac, Optics, Addison Wesley (1975).

[46] Born and Wolf, Principles of Optics, Plenum Press (1975).

[47] B.S. Kawasaki, K.O. Hill, D.C. Johnson and Y. Fujii, Optics Lett. 3, 66 (1978).

[48] K. Nagano, S. Kawakami & S. Nishida, Appl. Optics 17, 2080 (1978).

[49] Yoshi Fujii, Private Communication.

[50] A.M. Glass, Optical Engineering 17, 470 (1978).

[51] T. Kimura and K. Dalkoku, Optical and Q.E. 9, 33 (1977).

[52] H. Kressel and J.K. Butler, Semiconductor Lasers and Heterojunction LEDs, Academic Press (1977).

[53] F.S. Chen, J. Appl. Phys. 40, 3389 (1969).

[54] S. Zembutsu, J. Noda and H. Iwasaki, Appl. Optics 19, 937 (1980).

[55] J.M. Moran and I.P. Kaminow, Appl. Optics 12, 1964 (1980).

[56] W.J. Tomlinson, I.P. Kaminow, E.A. Chandross, R.L. Fork and W.T. Silfvast, Appl. Phys. Lett. 16, 486 (1970).

[57] R.A. Bartolini, A. Bloom and H.A. Weakliem, Appl. Optics 15, 1261 (1976).

[58] A. Katzir, A.C. Livanos, J.B. Shellan and A. Yariv, IEEE QE-13, 296 (1977).

[59] J.B. Shellan, C.S. Hong and A. Yariv, Optics Comm. 23, 398 (1977).

[60] M. Miller, Optical and Q.E. 11, 359 (1979).

[61] C.T. Chang, Elect. Lett 15, 765 (1979).

[62] C.T. Chang, Appl. Optics 18, 2516 (1979).

[63] K. Jürgensen, Appl. Optics 18, 1259 (1979).